University of Cincinnati

Date: 7/12/2018

I, Mohamed A. Abbass M.S., hereby submit this original work as part of the requirements for the degree of Doctor of Philosophy in Biomedical Engineering.

It is entitled:

Real-time Control of Ultrasound Thermal Ablation using Echo Decorrelation Imaging Feedback

Student's name: **Mohamed A. Abbass M.S.**

This work and its defense approved by:

Committee chair: T. Douglas Mast, Ph.D.

Committee member: Syed Ahmad

Committee member: Jing-Huei Lee, Ph.D.

Committee member: Marepalli Rao, Ph.D.

30483

Real-time control of ultrasound thermal ablation using echo decorrelation imaging feedback

A dissertation submitted to the Graduate School of the
University of Cincinnati
in partial fulfillment of the requirements for the degree of
Doctor of Philosophy
in the
Department of Biomedical Engineering
of the College of Engineering and Applied Science

by

Mohamed Ahmed Mahmoud Abbass
M.Sc. in Biomedical Engineering

Dissertation Committee:

T. Douglas Mast, Ph.D. (Committee Chair)
Department of Biomedical Engineering, College of Engineering and Applied Science
Jing-Huei Lee, Ph.D.
Department of Biomedical Engineering, College of Engineering and Applied Science
Marepalli B. Rao, Ph.D.
Department of Environmental Health, College of Medicine
Syed A. Ahmad, M.D.
Department of Surgery, College of Medicine

Abstract

Liver cancer, including hepatocellular carcinoma and colorectal metastases, is the second greatest cause of cancer-related death worldwide. Liver transplantation is considered the gold standard for hepatic cancer treatment. However, it is limited by the availability of liver donors and by cost. Hepatic resection is another treatment option that offers a high long-term survival rate. However, the overall resectability rate is low due to chronic liver disease and tumor location. Thermal ablation, including radiofrequency ablation as well as microwave and ultrasound ablation, has become an important alternative to liver resection and transplantation. To avoid incomplete treatments and cancer recurrence while reducing morbidity, a real-time monitoring and control approach, capable of providing consistent thermal ablation in minimal time, is needed.

Echo decorrelation imaging has been successfully employed to monitor ultrasound ablation and radiofrequency ablation both *ex vivo* and *in vivo*. In this dissertation, its utility for real-time control of ultrasound ablation was assessed in *ex vivo* bovine liver and *in vivo* rabbit liver with VX2 tumor. Ultrasound exposures and echo decorrelation imaging were performed using 5 MHz linear image-ablate array. Sonications were automatically ceased when the minimum or average cumulative echo decorrelation within a control region of interest (ROI) exceeded a predetermined threshold, corresponding to high specificity for prediction of local tissue ablation or complete ROI ablation. Ablation outcomes, treatment time

and prediction performance were statistically compared between controlled and uncontrolled groups.

For controlling *ex vivo* focused ultrasound treatments, a small control ROI was placed at the focal zone and the selected control threshold corresponded to 90% specificity of local ablation prediction for preliminary *ex vivo* experiments. Controlled trials were compared to uncontrolled trials employing 2, 5 or 9 therapy cycles. For controlling *ex vivo* unfocused ultrasound treatments, an optimization approach was developed to determine stopping criteria for two series of controlled experiments using different echo decorrelation imaging feedback parameters and sonication sequences. Controlled trials were compared with uncontrolled trials employing 9 or 18 therapy cycles of matching sonication sequences. For controlling *in vivo* focused and unfocused ultrasound treatments, the selected control threshold corresponded to 90% specificity for tumor ablation prediction in previous *in vivo* experiments. Controlled trials were compared with a previous series of uncontrolled *in vivo* experiments employing focused and unfocused ultrasound ablation in rabbit liver and VX2 tumor.

In general, controlled trials resulted in higher ablation rate, smaller lesion dimensions and treatment time compared to uncontrolled trials with longer duration. However, controlled trials showed equivalent lesion dimensions and treatment time, but higher ablation rate compared to uncontrolled trials with shorter duration. Better echo decorrelation prediction capability was observed for controlled trials compared to uncontrolled trials with shorter duration, but equivalent prediction performance was observed when compared to uncontrolled trials with longer duration. For most controlled trials, integrated backscatter imaging showed similar behavior to echo decorrelation for local ablation prediction. These results indicate that control using echo decorrelation imaging may improve the reliability and duration of ultrasound-guided focused and unfocused ultrasound ablation treatments.

Publications

The author of this dissertation has contributed to the following published peer-reviewed scientific journal articles, conference proceedings, and abstracts.

Published peer-reviewed journal articles:

M. A. Abbass, J. K. Killin, N. Mahalingam, F. M. Hooi, P. G. Barthe, and T. D. Mast, "Real-time spatiotemporal control of high-intensity focused ultrasound thermal ablation using echo decorrelation imaging in *ex vivo* bovine liver," *Ultrasound Med. Biol.*, vol. 44, no. 1, pp. 199–213, 2018.[1]

M. A. Abbass, A-J. Garbo, N. Mahalingam, J. K. Killin, P. G. Barthe, and T. D. Mast, "Optimized echo decorrelation imaging feedback for bulk ultrasound ablation control." *IEEE Trans. Ultrason., Ferroelect., Freq. Control.* In press, 2018.[2]

Published conference proceedings:

M. A. Abbass, A-J. Garbo, N. Mahalingam, J. K. Killin, and T. D. Mast, "Real-time control of bulk ultrasound thermal ablation using echo decorrelation imaging feedback," in: *Proc. IEEE Int. Ultrason. Symp.*, 2017.

M. T. Cox, **M. A. Abbass**, N. Mahalingam, A-J. Garbo, K. S. Krothapalli, and T. D. Mast, "Focused ultrasound ablation using electronically scanned grating lobes with real-time echo decorrelation imaging feedback," in: *Proc. IEEE Int. Ultrason. Symp.*, 2017.

Published abstracts:

M. A. Abbass, J. K. Killin, N. Mahalingam, and T. D. Mast, "Real-time feedback control of high-intensity focused ultrasound thermal ablation using echo decorrelation imaging," *J. Acoust. Soc. Am.*, vol. 141, no. 5, p. 3550, 2017.

M. A. Abbass, N. Mahalingam, K. S. Krothapalli, S. A. Ahmad, and T. D. Mast, "*In vivo* ultrasound thermal ablation controlled using echo decorrelation imaging," *J. Acoust. Soc. Am.*, vol. 143, no. 3, p. 1927, 2018.

M. T. Cox, **M. A. Abbass**, and T. D. Mast, "Simulation and analysis of three-dimensional echo decorrelation imaging," *J. Acoust. Soc. Am.*, vol. 143, no. 3, p. 1929, 2018.

[1]Parts of this paper were reproduced verbatim with permission from the publisher in Chapters 1, 2, and 5.

[2]Parts of this paper, © 2018 IEEE, were reproduced verbatim with permission from the publisher in Chapters 1, 3, and 5.

Acknowledgments

First and foremost, I would like to thank God (Allah), the most merciful and the most compassionate, for His help and blessings.

بِسْمِ اللهِ الرحمن الرَّحيمِ

يَرْفَعِ اللَّهُ الَّذِينَ آمَنُوا مِنكُمْ وَالَّذِينَ أُوتُوا الْعِلْمَ دَرَجَاتٍ

صدق اللَّهُ العظيم

"Allah will raise up, to ranks, those of you who believe and who have been granted knowledge."

(Quran; Surah Al-Mujadilah: 11)

I am really speechless at this moment, when my blood, sweat and tears I have put altogether for years is being honored. It wouldn't be possible without the continuous support of my advisor Dr. T. Douglas Mast, the light that guided me through. I will always be indebted to him. I would like to thank all my colleagues of the Biomedical Acoustics Laboratory; Tyler Fosnight, Dr. Kyle Rich, and Michael Cox for making my adjustment to the new scientific environment easy and smooth. I would like to thank all the undergraduate students of the UC Co-op program; Jakob Killin, Neeraja Mahalingam, Allison-Joy Garbo, Krishna Sameer Krothapalli, and Jack Masterson for providing all the effort and time needed to finish my experimental work.

Also, I would like to thank my committee members: Dr. Jing-Huei Lee, Dr. Marepalli B. Rao, and Dr. Syed A. Ahmad for their fruitful comments and discussions. I would

like to thank all the faculty members, current and recent students of the Image-guided Ultrasound Therapeutic Laboratories for their continuous assistance and help. Many thanks to Dr. Christy Holland and Dr. Kevin Haworth for their advice, for allowing me to use their lab equipment in my experiments, and for supporting me in Acoustical Society of America meetings. Thanks to Dr. Himanshu Shekhar, Dr. Karla Mercado-Shekhar, and Robert Kleven for their friendly comments on my work and practice talks, which really improved me.

I would like to take the moment to recognize and praise the unconditional support that I never imagined someone could ever have the capacity to give. Thanks to my parents Ahmed and Embarka, my wife Kariman, and my children Omar and Alya.

May the knowledge and experience I learnt throughout this journey be conveyed and paid forward to make the world a better place. I would like to thank our funding source, the National Institutes of Health. I would like to thank the Egyptian government for the financial assistance of my tuition and living expenses.

Contents

List of Tables

Table **Page**

List of Figures

Figure **Page**

List of Abbreviations

A-mode Amplitude mode

ANOVA Analysis of variance

AUC Area under the curve

ATM Array therapy module

BCLC Barcelona Clinic Liver Cancer

B-mode Brightness mode

CLM Colorectal metastases

CT Computed tomography

CEUS Contrast-enhanced ultrasound

FN False negative

FP False positive

GUI Graphical user interface

IBS Integrated backscatter

IQ In-phase and quadrature

KS Kolmogorov-Smirnov

HCC Hepatocellular carcinoma

HIFU High-intensity focused ultrasound

HSD Honest significance difference

HMI Harmonic motion imaging

LMI Localized motion imaging

MR Magnetic resonance

MRI Magnetic resonance imaging

MWA Microwave ablation

M-mode Motion mode

NRMSE Normalized root-mean square error

PBS Phosphate-buffered saline

RF Radiofrequency

RFA Radiofrequency ablation

ROC Receiver operating characteristic

ROI Region of interest

RTIF Real-time image fusion

RMS Root-mean square

RMSE Root-mean square error

SPTP Spatial-peak temporal-peak

TTC Triphenyl-tetrazolium chloride

TN True negative

TP True positive

US Ultrasound

2D Two-dimensional

3D Three-dimensional

Chapter 1
Introduction

1.1 Liver cancer

Liver cancer is the second greatest cause of cancer-related death (788,000 deaths) worldwide. According to American Cancer Society statistics [1], the expected number of liver cancer patients and deaths in the United States for 2018 are 42,220 (30,610 in men and 11,610 in women) and 30,200 (20,540 in men and 9,660 in women), respectively. Also, it is predicted that the incidence of liver cancer will increase by more than 50% from 2010 to 2020 in the United States [2]. Hepatocellular carcinoma (HCC) is the most common primary malignant tumor in liver, especially in patients with cirrhosis (70–90% of all cirrhosis patients) [3, 4]. Liver cirrhosis due to chronic infections of hepatitis B or C virus [5], alcoholism [6], or long-term fatty liver acts as a substrate for HCC development [7]. However, hepatitis B patients (common in Asia and Africa) may also develop HCC in non-cirrhotic liver, but at lower frequency [4]. HCC can be classified morphologically into three types [8, 9]: nodular HCC usually found in cirrhotic liver as single or multiple encapsulated lesions, massive HCC usually found in non-cirrhotic liver as a large lesion with satellite nodules, and diffuse HCC which is found as a large number of small nodules throughout the lobe or organ.

Treatment and prognosis of HCC depend on the tumor stage and status of the residual liver function [10]. Regular screening is highly recommended for patients with liver cirrhosis every 6 months using ultrasonography or tumor biomarkers (e.g., serum alpha-fetoprotein [11]) to detect HCC early [12]. Patients with confirmed HCC are managed according to the Barcelona Clinic Liver Cancer (BCLC) classification system [13], which recommends the best treatment option for each stage. Based on the BCLC staging system, patients are classified into early-stage, intermediate-advanced, and end-stage HCC. Liver transplantation is considered the gold standard for HCC treatment for eligible patients (e.g., solitary tumor with normal portal pressure). Patients who are candidates for liver transplantation should also fulfill the Milan criteria (one tumor with diameter ≥ 2 cm and ≤ 5 cm, or maximum three tumors with diameters ≥ 1 cm and ≤ 3 cm). Following these criteria offers a high post-transplantation 5-year survival rate ($> 70\%$) and a low 5-year tumor recurrence rate ($< 25\%$) [3]. However, transplantation is limited by the availability of liver donors and by cost. Another favorable therapeutic option for early-stage HCC patients with non-cirrhotic liver is hepatic resection. Partial hepatectomy provides shorter waiting times [14] and comparable 5-year survival rates (60–70%) [15] compared to transplantation. However, the overall resectability rate (20–30%) is low due to a combination of underlying chronic liver disease, tumor location (e.g., close to vascular structures or the diaphragm), and the multifocal nature of some HCC [16].

The liver is also one of the most common sites for secondary tumors, e.g. colorectal metastases (CLM). Prevalence of CLM is affected by the incidence of colorectal cancer, the third most common cancer worldwide. Approximately 50% of patients with colorectal cancer develop CLM [17]. Surgical resection is the gold standard for treating isolated CLM in patients who are medically qualified for hepatectomy [18]. Partial hepatectomy for CLM

provides $< 5\%$ mortality [18] with a 30–58% 5-year survival rate [19, 20]. However, the number of CLM patients eligible for resection is $< 20\%$ due to unsuitable tumor locations and impaired residual liver function [21]. Chemotherapy [22] and local ablation provide alternative treatments for unresectable CLM tumors or can potentially act as a bridge to CLM resection. Thermal ablation may also be employed to assist surgical resection [23, 24] to reduce intraoperative blood loss and postoperative hospitalization [24]. In the following section, various thermal ablation techniques are discussed.

1.2 Thermal ablation of liver cancer

Thermal ablation techniques are the most appropriate option for HCC patients who are ineligible for transplantation or resection and with tumor size less than 3 cm, based on the BCLC classification system. Thermal ablation may also provide a 5-year overall survival rate equivalent to surgical resection (47.6% vs. 56.0%) for patients with small CLM [25].

Minimally invasive bulk thermal ablation, including laser interstitial thermotherapy [26], radiofrequency ablation (RFA) [27], microwave ablation (MWA) [28], and high-intensity ultrasound (US) (e.g., interstitial [29, 30], focused [31, 32], and unfocused [33]) ablation, is an important treatment approach to unresectable primary and secondary liver tumors (e.g., HCC and CLM) [34, 35]. High-intensity focused ultrasound (HIFU) is a noninvasive thermal ablation technique that is capable of producing coagulative necrosis at a precise focal point within the tissue without harming overlying and adjacent structures, even for those within the beam path [36], providing sufficient residual liver tissue for patient survival [37]. HIFU has been employed to treat unresectable liver cancer in thousands of cases in China [38].

All thermal ablation techniques aim to rapidly elevate the tissue temperature above 60 °C, resulting in thermal coagulative necrosis within a zone encompassing all tumor margins, to

avoid incomplete treatment (e.g., in one RFA study, 48% of tumors close to large blood vessels were treated incompletely [39]) and cancer recurrence (e.g., in a recent study, 14% of RFA-treated malignant liver tumors developed local recurrence [40]). However, uncontrolled ablation of large regions may also damage nearby critical liver structures (e.g., the hepatic artery and portal vein). Therefore, real-time monitoring and control methods, capable of providing consistent thermal ablation in minimal treatment time, could improve bulk thermal ablation treatments. In the following section, different monitoring methods for thermal ablation guidance are discussed.

1.3 Real-time monitoring methods for thermal ablation

Imaging modalities are needed for real-time monitoring of tissue changes during HIFU or bulk thermal ablation. Magnetic resonance-guided HIFU (MRg-HIFU) and ultrasound-guided HIFU (USg-HIFU) are the most commonly used platforms for HIFU treatment guidance and control. MRg-HIFU has been used for monitoring and control of thermal ablation using real-time MR thermometry [41, 42, 43, 44, 45]. However, MR imaging increases treatment complexity and cost [46, 47]. USg-HIFU is more portable and inexpensive, while its high frame rate, real-time capability potentially makes it more capable of ablating mobile organs (e.g. liver [48, 49] and kidney [50, 51]).

Various monitoring algorithms have been developed to detect HIFU-induced thermal lesioning based on ultrasound pulse-echo imaging, including B-mode [52, 53], M-mode [54], backscatter [55, 56, 57], echo strain imaging [58], harmonic motion imaging (HMI) [59, 60, 61], elastography [62], and acoustic radiation force imaging [63]. All these methods aim to provide feedback on the progress of thermal treatment and to confirm the completeness of ablation. However, these methods are sensitive to errors caused by the formation of microbubble clouds

at the ablation site [64], the complex nonlinear dependency of tissue acoustic and viscoelastic properties on temperature [65] and decorrelation of the backscattered signal caused by tissue motion [66], bubble activity [54, 67], and heat-induced changes in tissue structure [68, 69, 70].

In clinical practice, RFA [71] and MWA [72] electrodes are typically placed in the target region under US or X-ray image guidance. Most ablation devices offer only crude automatic control, based on tissue electrical impedance or temperature measured at one or more antenna tines [73], but cannot provide detailed spatial feedback on all points in the ablation volume. As a result, RFA and MWA procedures rely heavily on operator skill, increasing the risk of untreated tumor and therefore local cancer recurrence. Alternative image-guided thermal ablation methods have been incorporated with US imaging [74, 75], computed tomography (CT) [76], and magnetic resonance imaging (MRI) [77, 78] for accurate therapy guidance and control. Although MRI provides precise 3D temperature mapping [28], it requires MR compatible tools [79], increasing treatment cost and complexity compared to US imaging. CT has the additional disadvantage of ionizing radiation.

Currently, B-mode US is the most common imaging modality for guidance of bulk thermal ablation, including RFA and MWA. Ultrasound imaging has advantages of being portable and inexpensive, while its high frame rate is suitable for real-time monitoring of moving organs like the liver [74]. Recent research efforts have used real-time US image fusion [80] with MRI or CT images, as well as contrast-enhanced US (CEUS) imaging [81], aid tumor margin visualization during treatment planning and assessment. However, the ability of B-mode US to predict the extent of thermal ablation is limited by the formation of heat-induced microbubble clouds (hyperechoic activity), causing acoustic shadowing and making tumor boundaries difficult to visualize [82].

1.4 Real-time control methods for thermal ablation

Real-time feedback control algorithms for HIFU and bulk thermal ablation based on pulse-echo ultrasound imaging have been tested in previous research [55, 66, 83, 84, 85], aiming to reduce treatment time and to enhance ablation accuracy [86].

For HIFU thermal ablation, Curiel et al. [66] evaluated the feasibility of using localized HMI to monitor and control HIFU ablation in VX2 rabbit tumors *in vivo*. Treatments were automatically stopped if the localized harmonic motion amplitude at the focus dropped below a specified amplitude threshold in two consecutive measurements. This algorithm was able to successfully control in 69% of the trials; echo decorrelation associated with tissue state changes and motion was considered a source of error. Similarly, Sugiyama et al. [83] used real-time localized motion imaging (LMI) as a feedback method to control HIFU thermal lesion length in porcine liver. Their feedback control system successfully provided lesion lengths close to their target (8–12 mm) with root-mean square error (RMSE) of 2.51 mm. However, errors were found in the estimated lesions' size and overtreatment occurred due to system delay after ceasing the HIFU sonication. Qu et al. [87] improved the LMI method by employing a dynamic cross-correlation window, which decreased the RMSE of the estimated coagulation length to 1.69 mm during porcine liver ablation ($N = 49$), but increased processing time for displacement estimation from 2.05 ± 0.05 s to 2.64 ± 0.36 s for 28 A-mode scan lines.

Recently, Takagi et al. [84] developed an approach for real-time monitoring and control of HIFU treatment based on cross-correlation of ultrasound signals, similar to echo decorrelation imaging. The cross-correlation coefficient between echo signals, calculated between the target frame and the first (reference) frame was used to detect thermal coagulation during HIFU treatments in chicken breast. HIFU exposures were automatically terminated when

the average cross-correlation coefficient within a focal region of interest (ROI) fell below a predetermined threshold. Feedback-controlled, HIFU treated samples were found to be more homogeneously coagulated compared to uncontrolled cases. However, they noted that further investigation is needed to determine the optimum coagulation threshold and to increase the monitoring frame rate for better detection of tissue changes in the presence of motion, boiling and cavitation. In addition, their approach of cross-correlating with a fixed, pre-treatment reference frame may not be amenable to control of *in vivo* HIFU ablation, where motion-induced decorrelation can be large [33, 88].

For bulk thermal ablation, Toshikuni et al. [85] have clinically demonstrated an RFA monitoring approach using a real-time image fusion (RTIF) system. Tumor boundaries were manually marked on a reference image (CT/CEUS/MRI), then automatically co-registered with real-time US images used to monitor the RFA ablation. Fused B-mode images were used to manually control the RFA, such that treatments were ceased when the hyperechoic region covered the spherical marker boundaries in all directions. RTIF-controlled trials achieved more effective treatment than uncontrolled trials. However, this approach is limited by its use of local echogenicity as an ablation predictor, which can lead to inaccurate prediction of RFA therapeutic effects [88, 89].

1.5 Echo decorrelation imaging

Echo decorrelation imaging [33, 88, 89, 90, 91] exploits the phenomenon of heat-induced echo signal decorrelation to locally map heat-induced tissue changes, including irreversible structural changes as well as transient microbubble activity, on millisecond time scales [70, 92]. This approach has been successfully employed to monitor HIFU and bulk US thermal ablation [33] and RFA [88, 89, 92] both *ex vivo* and *in vivo*, and has been shown to predict

local ablation more effectively than changes in echogenicity (e.g., integrated backscatter). A method to extract heat-induced decorrelation from artifactual motion- and noise-induced decorrelation has been shown feasible for monitoring of *in vivo* RFA [70]. Notably, the same heat-induced decorrelation limits the utility of several other pulse-echo US imaging methods such as elastography [93] and echo strain imaging [94, 95] to accurately characterize tissue during thermal ablation [64, 66, 70] as described in the previous section. Although such approaches have been demonstrated feasible for control of multiple-focus ultrasound heating [96] as well as ultrasonic hyperthermia [97], heat-induced decorrelation may limit their applicability to control of bulk thermal ablation.

Echo decorrelation images, comprising maps of the local echo decorrelation per millisecond, were computed as [88]

$$\Delta(y,z,t) = 2\left[\frac{\beta^2(y,z,t) - |R_{01}(y,z,t)|^2}{\tau\left[\beta^2(y,z,t) + \overline{\beta^2}(t)\right]}\right], \tag{1.1}$$

where y and z are azimuthal (array) and range (depth) image coordinates and τ is the inter-frame time in milliseconds. R_{01} is the position-dependent, zero-lag, windowed spatial cross-correlation between two consecutive complex image frames, while $\beta^2(y,z,t)$ is an integrated backscatter (IBS) term determined from the corresponding autocorrelations of the two frames:

$$\begin{aligned} R_{01}(y,z,t) &= \langle I(y,z,t)^* I(y,z,t+\tau)\rangle, \\ \beta^2(y,z,t) &= \langle |I(y,z,t)|^2\rangle\langle |I(y,z,t+\tau)|^2\rangle, \end{aligned} \tag{1.2}$$

where $\langle . \rangle$ represents two-dimensional convolution with a Gaussian window [88], while $\overline{\beta^2}$ denotes the spatial mean average of $\beta^2(y,z,t)$. The echo decorrelation term in Eq. (1) was normalized by the inter-frame time τ to define the echo decorrelation map per millisecond [33] and by $\beta^2(y,z,t)$ and $\overline{\beta^2}$ to reduce decorrelation artifacts in hypoechoic and hyperechoic

regions respectively [89]. More detailed derivation and analysis of echo decorrelation imaging is given elsewhere [33, 70, 88, 89, 98].

Echo decorrelation maps were computed from image frames recorded immediately after each sonication cycle. For each cycle, an ensemble-averaged echo decorrelation map $\overline{\Delta}(y, z, m)$ was computed as

$$\overline{\Delta}(y, z, m) = \frac{1}{K-1} \sum_{k=1}^{K-1} \Delta(y, z, k\tau), \tag{1.3}$$

where m is the therapy cycle index, K is the number of image frames recorded per cycle, and k is the frame index.

Cumulative echo decorrelation maps $\Delta(y, z, m)_{\text{cum}}$ were defined as the accumulated temporal maximum of the ensemble-averaged echo decorrelation maps for each pixel (y, z):

$$\Delta(y, z, m)_{\text{cum}} = \max\left(\overline{\Delta}(y, z, m-1), \overline{\Delta}(y, z, m)\right). \tag{1.4}$$

For comparison, ablation prediction using IBS imaging was also employed. IBS imaging was previously tested for HIFU thermal ablation prediction by Zhong et al. [99]. Ensemble averaged IBS maps ($\overline{\beta}(y, z, m)$) for each therapy cycle were normalized by the cumulative IBS map of the sham cycles (β_{sham}) as defined previously in Fosnight et al. [33]. Cumulative decibel-scaled IBS images were computed as

$$\overline{\beta}(y, z, m) = 10 \cdot \log_{10}\left(\frac{\frac{1}{K-1}\sum_{k=1}^{K-1} \beta(y, z, k\tau)}{\beta_{\text{sham}}}\right), \tag{1.5}$$

$$\text{IBS}_{\text{cum}} = \max\left(\overline{\beta}(y, z, m-1), \overline{\beta}(y, z, m)\right) \tag{1.6}$$

where m is the therapy cycle index, K is the number of image frames recorded per cycle, and k is the frame index.

Two-dimensional echo decorrelation imaging and US therapy were performed using 5 MHz, 64-element image-treat linear arrays with 4.8×24.4 mm^2 aperture for all trials

reported in the dissertation. The approximate region for imaging and treatment extended from $-12.2 < y < 12.2$ mm in azimuth, $0 < z < 50.8$ mm in range, and $-2.4 < x < 2.4$ mm in elevation. Use of an image-treat transducer provided precise spatial registration between 2D echo decorrelation maps and treatment planes [100], allowing accurate feedback on thermal ablation progression and facilitating accurate registration of US images with histologic tissue sections.

1.6 Hypothesis and specific aims

The primary goal of the studies reported here was to develop a real-time closed-loop approach to control HIFU and bulk US thermal ablation using echo decorrelation imaging feedback *ex vivo* and *in vivo*.

The **central hypothesis** of the studies is that using echo decorrelation imaging feedback for controlling US thermal ablation provides precise thermal lesioning with smaller treatment time and better cell death prediction than uncontrolled US ablation. To test this hypothesis, a comprehensive research plan was constructed and is summarized in the following specific aims.

1.6.1 Specific Aim 1: Develop a real-time closed-loop algorithm for US thermal ablation control

Specific Aim 1a: Evaluate the control algorithm in *ex vivo* HIFU thermal ablation experiments. In this aim, the control algorithm was assessed in controlling HIFU thermal ablation in *ex vivo* bovine liver. Controlled trials were compared with uncontrolled trials employing the same sonication sequence, but with different numbers of therapy cycles. The lesion dimension, treatment time, and ablation prediction ability of the controlled and uncontrolled groups were statistically compared.

Specific Aim 1b: Evaluate the control algorithm in *ex vivo* bulk US thermal ablation experiments. The goal of this aim was to assess the control algorithm in controlling bulk US ablation in *ex vivo* bovine liver.

1.6.2 Specific Aim 2: Optimize the echo decorrelation imaging feedback for bulk US thermal ablation control

An optimization method was applied to select control criteria for two series of controlled and uncontrolled *ex vivo* bulk US ablation experiments using different echo decorrelation imaging feedback parameters. Ablation outcomes of the controlled trials were statistically compared with matching uncontrolled trials.

1.6.3 Specific Aim 3: Evaluate the control algorithm in *in vivo* HIFU and bulk US thermal ablation experiments

The goal of this aim was to test the feasibility of controlling HIFU and bulk US thermal ablation in *in vivo* rabbit liver and VX2 tumor. This aim was completed by comparing ablation outcomes and prediction capability for the controlled trials with the uncontrolled trials reported by Fosnight et al. [33] in a similar *in vivo* study.

1.7 Dissertation organization

The rest of the dissertation is organized as follows.

Chapter 2 introduces the closed loop algorithm used to control thermal ablation using echo decorrelation imaging feedback. The developed real-time control algorithm was evaluated in *ex vivo* HIFU thermal ablation experiments (**Specific Aim 1a**). Controlled trials were compared with uncontrolled trials with shorter or longer duration (2-cycle, 5-cycle, and 9-cycle). Ablation outcomes and prediction capability were statistically tested for each group.

Chapter 3 describes the optimization approach developed to optimize the echo decorrelation imaging feedback criteria for controlling *ex vivo* bulk US thermal ablation in two series of experiment employing different sonication sequences (**Specific Aim 2**). The control algorithm employing the optimized stopping criteria were evaluated in *ex vivo* bulk thermal ablation experiments (**Specific Aim 1b**). Controlled trials were compared with uncontrolled trials with shorter or longer duration (9-cycle and 18-cycle). Ablation outcomes and prediction capability were statistically tested for each group.

Chapter 4 demonstrates the feasibility to control HIFU and bulk US thermal ablation in *in vivo* rabbit liver and VX2 tumor (**Specific Aim 3**). In this chapter, the stopping criteria were modified to match the acoustical and anatomical characteristics of the *in vivo* tissue. The motion and noise compensation method previously derived by Hooi et al. [70] ws implemented to work simultaneously with the control algorithm. Controlled trials were compared with uncontrolled trials from a similar *in vivo* study reported by Fosnight et al. [33]. Ablation outcomes and prediction capability were statistically tested for each group.

Chapter 5 summarizes the results of the dissertation and suggests future research directions for ablation control by echo decorrelation imaging.

Chapter 2
Real-time control of HIFU thermal ablation using echo decorrelation imaging feedback

2.1 Objectives

High-intensity focused ultrasound (HIFU) is a potential therapeutic method for precise ablation of unresectable liver cancer without damaging vital structures [35]. However, its long treatment duration could be a problem, especially for patients with poor physical condition [101]. Hence, a real-time monitoring and control method capable of providing accurate and precise thermal lesions, while minimizing treatment time, is needed.

Recently, ultrasound (US) echo decorrelation imaging was successfully validated in predicting HIFU thermal ablation in *in vivo* rabbit liver and VX2 tumor [33]. Also, its utility as thermal coagulation feedback to control HIFU ablation was tested in *ex vivo* chicken breast by Takagi et al. [84], to reduce treatment time and to provide homogeneous thermal lesioning. However, it was noted that further investigation is needed to determine the optimum coagulation threshold for better control performance.

In this chapter, the feasibility of controlling HIFU thermal ablation using 2D echo decorrelation imaging was assessed with a view toward *in vivo* implementation. The echo decorrelation imaging approach employed here tracks changes in echo signals over millisecond-scale

intervals, potentially providing more robust control than cross-correlation with a fixed reference frame [84]. The main goals of this chapter were to (i) implement an automated control algorithm based on real-time echo decorrelation imaging; (ii) determine the optimum echo decorrelation threshold for HIFU control; (iii) test the algorithm in *ex vivo* bovine liver experiments; and (iv) statistically assess the effect of control on thermal lesioning results.

2.2 Materials and methods

In this section, materials and methods for a series of experiments on controlled ablation of *ex vivo* liver tissue are discussed. In these experiments, both HIFU ablation and echo decorrelation imaging were performed using a linear, 5 MHz image-treat array, with treatments ceased after echo decorrelation exceeded a predetermined threshold throughout the focal region of interest. An overview of the experimental setup is shown in Fig. 2.1(a)–(b).

2.2.1 Echo decorrelation feedback control algorithm

To control HIFU ablation using echo decorrelation imaging, a real-time, closed-loop control algorithm was developed. This algorithm was integrated with a real-time imaging application used to compute B-mode and echo decorrelation images from beamformed radiofrequency (RF) echo signals acquired immediately after each sonication pulse, during the rest period of the HIFU transducer, as shown in Fig. 2.1(d). For each cycle, an ensemble-averaged echo decorrelation map was computed using Eq. 1.3. The cumulative echo decorrelation map was defined as the accumulated temporal maximum of the ensemble-averaged echo decorrelation maps for each pixel (Eq. 1.4).

A flow chart of the control algorithm is shown in Fig. 2.1(c). The cumulative echo decorrelation $\Delta(y, z, m)_{\text{cum}}$ was used as a feedback predictor for closed-loop ablation control, qualitatively representing the time history of thermal energy deposition in the tissue.

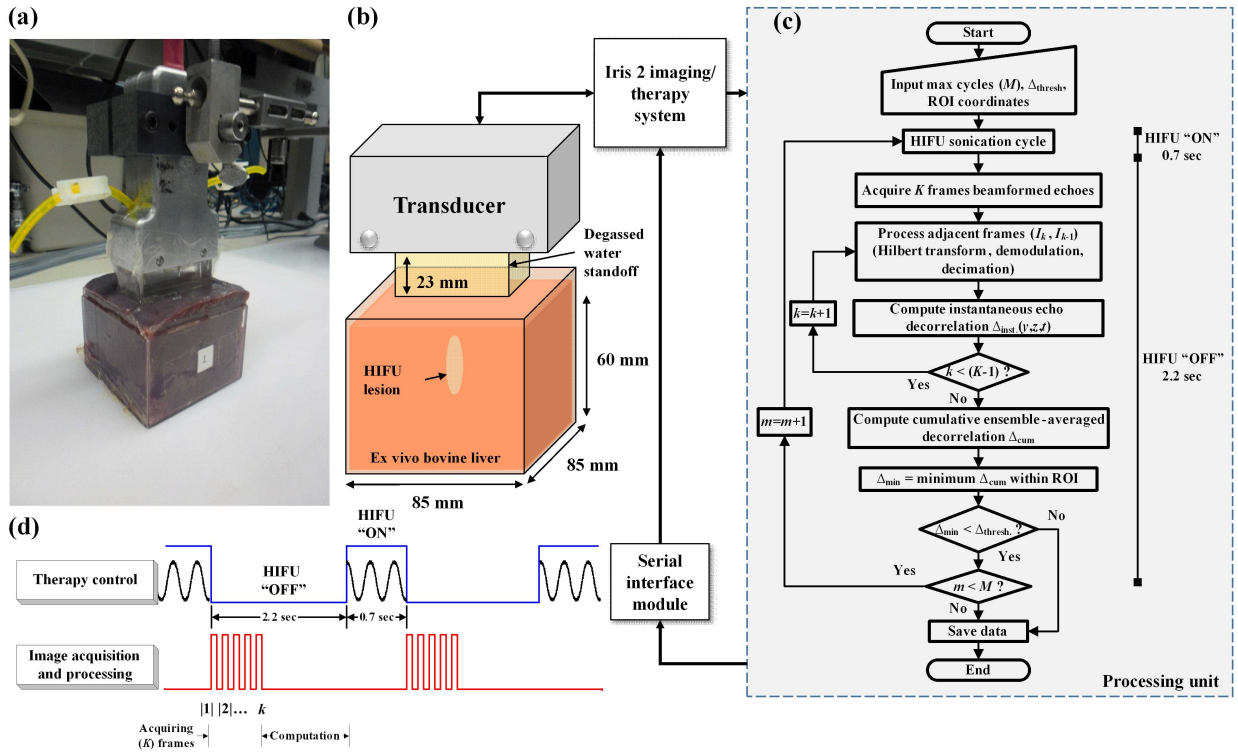

Figure 2.1: Experimental setup. (a) 64 element image-treat transducer aligned with *ex vivo* bovine liver during the *in vitro* experiment, (b) schematic of the experimental setup, (c) the developed real-time feedback control algorithm flow chart, (d) timing diagram of the treatment scenario.

The imaging application overlaid the cumulative echo decorrelation map over the B-mode image at the end of each sonication cycle, resulting in a frame rate of 0.344 Hz (inverse of the 2.9 s cycle length). Treatments were automatically terminated when either the minimum cumulative echo decorrelation within a focal ROI exceeded the predetermined ablation control threshold or when the current sonication cycle index m exceeded the maximum number of sonication cycles M.

2.2.2 HIFU ablation experiments

2.2.2.a Tissue handling and preparation

Tissue handling followed procedures employed in previous studies of echo decorrelation imaging during *ex vivo* thermal ablation [89, 92]. A freshly excised bovine liver was obtained from a local slaughterhouse and placed in ice-cold, deionized, degassed phosphate-buffered saline (PBS). Liver tissue specimens were cut to fit a square cuboid acrylic cuvette with dimensions $85 \times 85 \times 60$ mm^3 with an open top for ultrasound imaging and treatment, as shown in Fig. 2.1(a). The tissue surface was covered with a layer of aqueous gel to couple the specimen and transducer while avoiding tissue dehydration. Experiments were performed at room temperature, with an average liver temperature of 21 °C measured before each trial.

2.2.2.b Treatment monitoring and control

HIFU treatments and imaging were controlled by the Iris 2 ultrasound imaging and therapy system (Ardent Sound, Mesa, AZ, USA) [102]. A custom image-treat linear array transducer (64 elements, 4.8×24.4 mm^2 aperture, frequency 5–5.4 MHz; Ardent Sound, Mesa, AZ, USA) performed both pulse-echo imaging ($> 40\%$ fractional bandwidth, transmit focal depth 3.5 cm, F-number 4) and HIFU therapy (maximum acoustic power 35 W). This array was integrated with a 23 mm water-filled standoff, filled with deionized, degassed water. The Iris 2 system was interfaced with a secondary personal computer (PC) that acquired beamformed RF echo signals using a 14-bit A/D converter (Compuscope 14200, Gage Applied) and initiated HIFU sonications via a custom programmable serial interface.

A graphical user interface (GUI), shown in Fig. 2.2, faciliated treatment planning, monitoring, and control for HIFU therapy. Before each ablation experiment, the user defined the maximum number of sonication cycles M, the ROI size/location, and the ablation control threshold Δ_{thresh} by parameters input to this GUI.

For HIFU treatments, a series of electronically focused exposures were fired in cycles with 0.7 s sonication followed by pulse-echo imaging and RF data acquisition during a 2.2–2.8 s rest period. The timing sequence of the HIFU exposures and echo data acquisition is shown in Fig. 2.1(d). Immediately after each HIFU exposure, twenty beamformed echo frames were acquired at a frame rate of 116 Hz. Echo data were sampled at 33.3 MHz and stored to a solid-state flash hard drive.

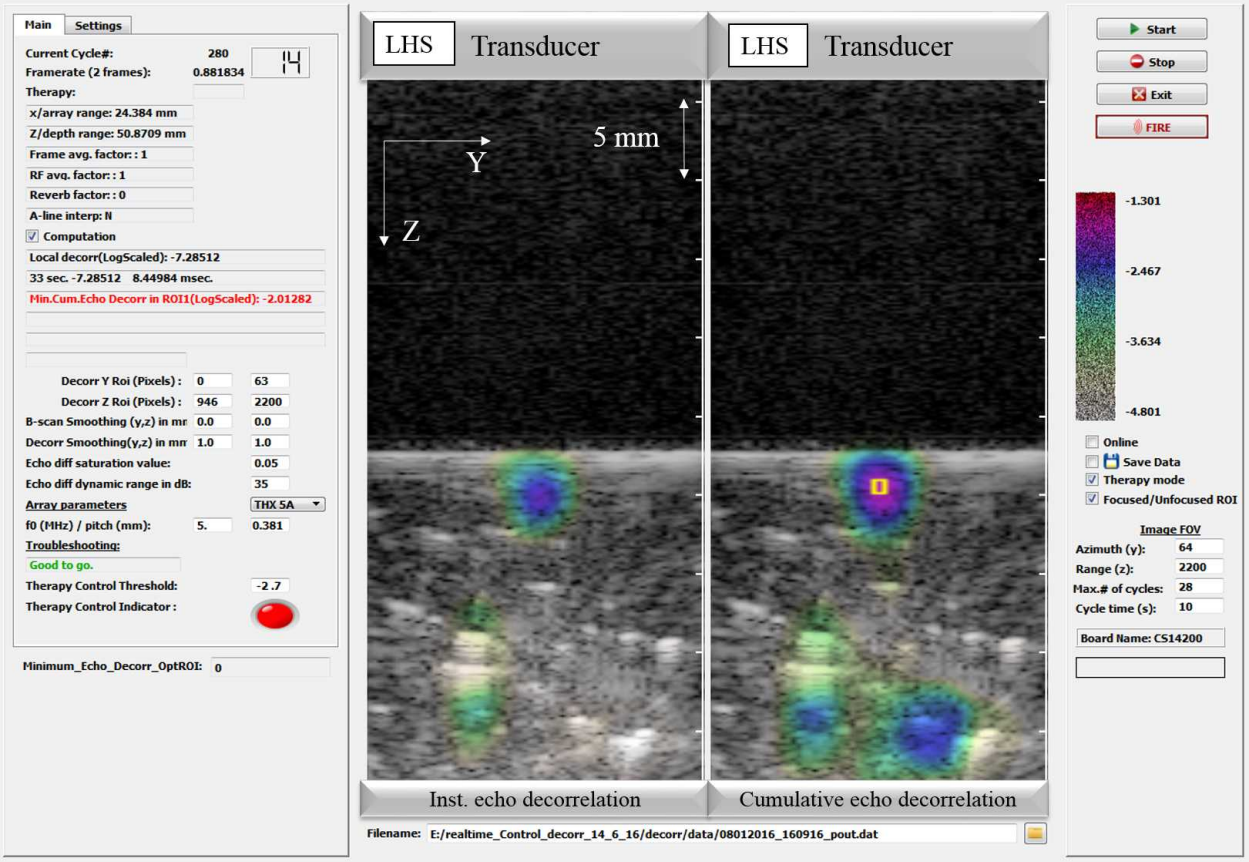

Figure 2.2: GUI of the implemented Qt-based C++ application used for the HIFU thermal ablation control and imaging; the controlling ROI is bounded by a yellow line.

2.2.2.c Image processing

Recorded echo signals were filtered by a Hilbert-transform filter providing in-phase and quadrature (IQ) complex signal components, then demodulated using a 5 MHz carrier frequency and decimated by a factor of 6. Demodulated IQ frames were used to compute B-mode images, maps of the local echo decorrelation per millisecond, and corresponding ensemble-averaged and cumulative echo decorrelation maps for each cycle [33] in real-time. In the GUI, instantaneous and cumulative echo decorrelation maps were superimposed on B-mode images for each frame for real-time feedback, as shown in Fig. 2.2.

2.2.2.d Image segmentation and registration

To directly relate echo decorrelation images to the desired outcome of tissue ablation, images were compared with tissue histology, as performed in many previous studies of ultrasound monitoring approaches (e.g., [45, 61, 103, 104]). After treatments, ablated liver tissue was frozen overnight at -80 °C in the same cuvette, maintaining tissue shape and orientation for accurate registration with ultrasound images. The tissue was then sectioned along the image plane and stained with 2% triphenyl tetrazolium chloride (TTC) vital stain. Ablated tissue histology was assessed based on TTC uptake, with regions of full TTC uptake (stained red) interpreted as non-ablated liver tissue and regions of partial or no TTC uptake interpreted as ablated tissue [105]. TTC-stained sections were optically scanned at 1200 dpi (CanoScan 8800F, Canon, Tokyo, Japan). Scanned histologic images were then manually segmented into ablated and non-ablated regions as in [33].

Image registration of segmented tissue sections with corresponding B-mode images was performed using 2D rigid registration with 3 degrees of freedom (two translations and one rotation), as done previously [33]. Landmark points placed at the left, right and top edges

of the HIFU lesion were used to center the histologic section at zero azimuth of the B-mode image. At the same time, the histologic section was rotated and translated to align with the segmented tissue surface on the B-mode image. Registration errors were estimated based on the vertical (range/depth direction) distance between the proximal tissue surfaces segmented on the B-mode and histologic images. Mean and root-mean-square (RMS) values of this distance, as well as the 95% confidence interval of the mean, were determined over all proximal boundary points from all controlled and uncontrolled trials.

2.2.2.e Assessment of thermal ablation prediction

The capability of echo decorrelation and integrated backscatter (IBS) imaging to predict local tissue ablation was assessed using receiver operating characteristic (ROC) curve analysis, as performed previously [33, 88]. For ROC curve analysis, cumulative echo decorrelation maps were computed using MATLAB (The MathWorks, Natick, MA, USA), including correction for decorrelation associated with electronic noise and tissue motion [33, 70]. ROC curves were computed by comparing thresholded cumulative echo decorrelation and IBS maps to histologic binary masks for each trial [33, 88], plotting the true-positive ratio (Sensitivity = TP/(TP+FN)) versus the false-positive ratio (1−Specificity = FP/(FP+TN)) over all image pixels and the entire range of echo decorrelation cutoffs [106]. In these expressions, TP (true positives) is the number of correctly predicted ablated points, FP (false positives) is the number of incorrectly predicted unablated points, TN (true negatives) is the number of correctly predicted unablated points, and FN (false negatives) is the number of incorrectly predicted ablated points. Area under the ROC curve (AUC) was computed using the trapezoidal rule; an AUC value of 1 represents the best possible prediction performance while a value of 0.5 indicates no predictive capability [106]. For each ROC curve, the optimal threshold for predicting local tissue ablation was determined as the cutoff value nearest to

the top-left corner of the ROC curve (i.e., a value simultaneously maximizing sensitivity and specificity) [107].

AUC values were tested for statistical significance against the null hypothesis (AUC = 0.5) using a general model for the AUC standard error [106] (one-tailed, significance criterion $p < 0.05$). The statistical significance of differences between AUC values was tested using the method of DeLong et al. [107, 108] (significance criterion $p < 0.05$, two-tailed). To account for non-independence of predictions for closely located pixels, statistical tests of AUC were adjusted using effective sample sizes determined from the maximum packing density (hexagonal packing) of circular windows with diameter matching the spatial resolution of echo decorrelation images ($d = 2.355$ mm for a Gaussian correlation window width $\sigma = 1.0$ mm) [33, 88].

2.2.3 Determination of ablation control threshold

The echo decorrelation threshold employed for controlled HIFU exposures was determined using a process outlined by Fosnight et al. [33] in an *in vivo* study of echo decorrelation imaging during ultrasound ablation. For this purpose, a set of preliminary HIFU ablation experiments was performed without use of the control algorithm. HIFU thermal ablation trials ($N = 13$) were carried out on fresh *ex vivo* bovine liver using the experimental setup and methods described above.

In each of the ablation trials, nine HIFU sonication cycles (20% duty cycle, 5.4 MHz frequency, as in the *in vivo* study reported by Fosnight et al. [33]) were performed using continuous-wave, high-intensity pulses, electronically focused along the array axis 2 mm below the tissue surface with 803–1125 W/cm^2 *in situ* spatial-peak, temporal-peak intensity (I_{SPTP}). I_{SPTP} was calculated as described previously [33]. For each cycle, the array was fired for 0.7 s (HIFU on) followed by a 2.8 s rest period during which pulse-echo images were acquired. Using simulations, temperatures in the focal plane were predicted for *ex vivo* liver

tissue using previously reported methods and parameters [100], assuming 0.5 dB/cm/MHz absorption, 21 °C initial temperature, and no perfusion. According to these simulations, one sonication cycle was sufficient to achieve ablative temperatures in all cases. For the lowest HIFU exposure intensity employed (5.4 MHz, 20% duty cycle, 803 W/cm^2 I_{SPTP}), the maximum estimated tissue temperature after one sonication cycle was 74 °C), while maximum tissue temperature reached the boiling point (100 °C) after two sonication cycles. Before the therapy cycles of each trial, nine sham sonications were employed to estimate decorrelation caused by electronic noise and tissue motion; this estimated artifactual decorrelation was then used to compensate decorrelation maps during the HIFU treatment [33, 70].

Treated tissue was sectioned, stained, and segmented and ROC curves were computed as described above. The sensitivity and specificity of pixel-by-pixel ablation prediction were determined as a function of the echo decorrelation threshold, and the control threshold was chosen as that producing 90% prediction specificity.

2.2.4 Controlled HIFU experiments

To test the performance of echo decorrelation imaging feedback for controlling HIFU thermal ablation, a series of experiments was carried out over a range of sonication intensities and exposure durations. The real-time closed loop algorithm described above was implemented to control the array therapy module (ATM) of the Iris 2 system using the Qt-Serial library. Code specifying each HIFU exposure, including amplitude, phasing, and timing, was sent to a custom serial interface module by a standard serial communication protocol (RS232, 115200 bps, 8N1) and stored in the buffer memory of the serial interface module before being sent to the ATM for execution. Sonications were repeated by sending a serial command to the serial interface module to execute currently stored therapy code.

A small ROI of 1×1 mm^2 was selected and located 2 mm below the tissue surface within the focal zone, as shown in Fig. 2.2. The control ROI was chosen to be smaller than

the spatial resolution of the echo decorrelation map, estimated as 2.35 mm for the Gaussian window employed here [88]. This ensured that decorrelation values computed within this ROI characterized echo changes at the focal position. A larger ROI could increase the possibility of false-positive ablation predictions due to any artifacts. To examine the effect of ROI size on the control algorithm, a *post hoc* analysis was performed on the cumulative echo decorrelation maps from all controlled trials. Means and standard errors of the minimum echo decorrelation inside square ROIs of different diameters (1–10 mm) were computed. To compare with approaches employing average decorrelation within an ROI [84], means and standard errors of the average decorrelation within the same ROIs were also computed.

HIFU exposures (5.0 MHz, 24% duty cycle) were performed with I_{SPTP} *in situ* ranging from 1064–1385 W/cm^2, with each therapy cycle comprising 0.7 s HIFU sonication followed by a 2.2 s rest period including pulse-echo imaging. The rest period corresponded to the time elapsed during acquisition of RF echo signals (0.5 s), transfer of echo data (0.4 s), computation of echo decorrelation and B-mode images (1.0 s), and firing of the next therapy cycle (0.3 s). Simulations showed a small increase in overall heating rate, compared to the 2.8 s rest period used in the preliminary experiments. After each cycle, echo decorrelation was computed; treatment was then continued if decorrelation failed to exceed its predetermined control threshold throughout the ROI, up to a maximum of $M = 18$ cycles. After each cycle, echo decorrelation was computed; treatment was then continued if decorrelation failed to exceed its predetermined control threshold throughout the ROI, up to a maximum of $M = 18$ cycles (twice the maximum number of cycles from a previous *in vivo* study of echo decorrelation imaging [33]). This procedure was followed for a total of 10 controlled ablation trials.

For comparison, series of uncontrolled HIFU ablation trials (5.0 MHz, 24% duty cycle) were also performed. The maximum number of uncontrolled therapy cycles was selected to be 9, corresponding to the number previously found sufficient to ensure *in vivo* ablation of

both rabbit liver and VX2 tumor [33, 98]. A total of 10 uncontrolled trials were performed using this maximum duration (total time 26.1 s for 9 cycles). An additional 10 uncontrolled trials were performed employing 5 therapy cycles (14.5 s), corresponding to the average sonication time required in the preliminary HIFU trials ($N = 13$) for the cumulative echo decorrelation to exceed the selected ablation control threshold throughout the ROI. Based on the initial controlled trials results, the sonication time required to reach the predetermined decorrelation threshold was found to vary from 1–3 cycles (2.9–8.7 s), with an average of 2 cycles (5.8 s). Hence, a third uncontrolled group ($N = 10$) was added to represent the average sonication time of the controlled trials, equal to 5.8 s (2 cycles).

After tissue sectioning, staining, registration, and segmentation as described above, thermal lesions for each trial were characterized by their width, area, depth and ablation rate, computed in MATLAB based on the binary maps of segmented tissue ablation. The lesion depth was measured as the vertical distance from the tissue surface to the deepest ablated point along the array axis (zero azimuth on the ultrasound images). The lesion width was measured as the azimuthal extent of ablated tissue along the horizontal (azimuthal) line taken at half the measured lesion depth. The lesion area was computed as the total area occupied by pixels mapped as ablated tissue. Ablation rate was defined as the measured lesion area per unit treatment time.

Statistical analysis was done using R software (R Foundation, Vienna, Austria). Means and standard errors of the lesion width, depth, area and ablation rate were computed for all groups. The normality of the width, depth and area for all groups was tested using the Shapiro-Wilk test with the significance criterion $p < 0.05$. For normally distributed groups, analysis of variance (ANOVA) was applied to test the hypothesis of no difference in means (significance criterion $p < 0.05$). If significant, a *post hoc* Tukey's honest significance difference (HSD) test was carried out for multiple comparison of means. For non-normally distributed groups, a Kruskal-Wallis rank sum test [109] (significance criterion $p < 0.05$) was

conducted to test the hypothesis of no median difference, followed by Dunn's test [110] for multiple pairwise comparisons with Bonferroni adjustment [111]. Equality of variances was tested statistically using the Bartlett test for the normally distributed groups and the Levene test for the non-normally distributed groups. The average treatment time of the controlled group was tested against the fixed treatment times of 5-cycle and 9-cycle uncontrolled groups using one-sample t-tests (two-tailed, significance criterion $p < 0.025$ including Bonferroni correction).

To test the performance of echo decorrelation and IBS imaging for predicting local thermal ablation in the controlled and uncontrolled trials, ROC curves and AUC values were computed for each group by the same method described above. The significance difference of AUC values against the null hypothesis (AUC = 0.5) and against each other (controlled vs uncontrolled groups) were tested as described in the previous subsection. Also, differences between AUC values for ablation prediction using echo decorrelation and IBS imaging were tested statistically using DeLong's method for area under correlated ROC curves [108]. Calculations of z statistics (two-tailed, significance criterion $p < 0.05$) were done in R using the pROC package [112]. Thereafter, z scores were adjusted based on the effective number of independent predictions, as described previously in Fosnight et al. [33] and Section 2.2.2.e, to compute the effective p value.

The capability of echo decorrelation and IBS imaging to predict ablated tissue area was evaluated for all groups. Predicted areas for echo decorrelation and IBS imaging were computed as the total area occupied by pixels with echo decorrelation values greater than a certain cutoff for a range of decorrelation ($\log_{10}$-scaled decorrelation per ms: -4 to -1) and IBS (-5 to 20 dB) cutoffs. RMS errors between predicted and measured lesion areas were calculated across all trials of all groups ($N = 40$). Optimal decorrelation and IBS cutoffs were determined as these corresponding to minimum RMS errors. At these optimal cutoffs, absolute RMS errors between predicted and measured areas were computed for each group.

Also, normalized RMS error (NRMSE) was computed for each group as a ratio between the absolute RMS error and the RMS value of the measured ablated area.

2.3 Results

Based on results of the preliminary experiments designed to determine the ablation control threshold, an ROC curve was computed to test the performance of echo decorrelation imaging as a predictor of local tissue ablation. Echo decorrelation imaging predicted local ablation significantly better than chance (AUC = 0.941, $p < 10^{-16}$). The sensitivity and specificity of local ablation prediction using echo decorrelation imaging are plotted as a function of the echo decorrelation threshold in Fig. 2.3. The echo decorrelation threshold for the controlled ablation experiments was selected as $\Delta_{\text{thresh}} = -2.7$ ($\log_{10}$-scaled decorrelation per ms) to achieve the prescribed specificity of 90% in the preliminary experiments. The corresponding sensitivity of ablation prediction at this threshold was 83%.

In the 10 controlled HIFU trials, successful control was achieved in all 10 cases. That is, in all 10 cases, the echo decorrelation threshold of -2.7 ($\log_{10}$-scaled decorrelation per ms) was reached throughout the focal ROI. The number of cycles required to reach this threshold ranged from 1 cycle (0.7 s sonication time or 2.9 s total therapy time) to 3 cycles (2.1 s sonication time or 8.7 s total therapy time). The mean number of cycles required for successful control was 2 (1.4 s sonication time or 5.8 s total therapy time), equal to the duration for the 2-cycle group (5.8 s therapy time) but significantly smaller than the 5-cycle group (14.5 s, $p = 1.8 \cdot 10^{-7}$) or the 9-cycle group (26.1 s, $p = 1.0 \cdot 10^{-10}$).

Means and standard errors of minimum (Δ_{min}) and average (Δ_{avg}) cumulative echo decorrelation values within ROIs of diameter 1–10 mm from all controlled trials are shown in Fig. 2.4. The mean of Δ_{min} exceeded the selected ablation threshold Δ_{thresh} in the 1×1 mm^2 ROI (mean $\pm$ standard error -2.23 ± 0.13) only. However, the mean of Δ_{avg} exceeded Δ_{thresh} in ROIs of size 1×1 mm^2 (-2.02 ± 0.098) to 5×5 mm^2 (-2.6 ± 0.116).

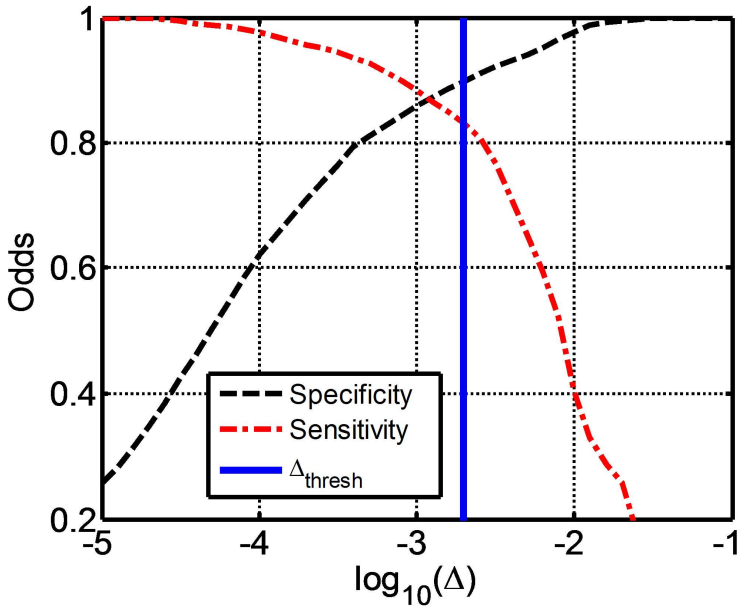

Figure 2.3: Plotted are $\log_{10}$-scaled echo decorrelation ablation prediction sensitivities and specificities calculated for the ($N = 13$) HIFU exposures in *ex vivo* liver; the blue line represents the ablation control threshold.

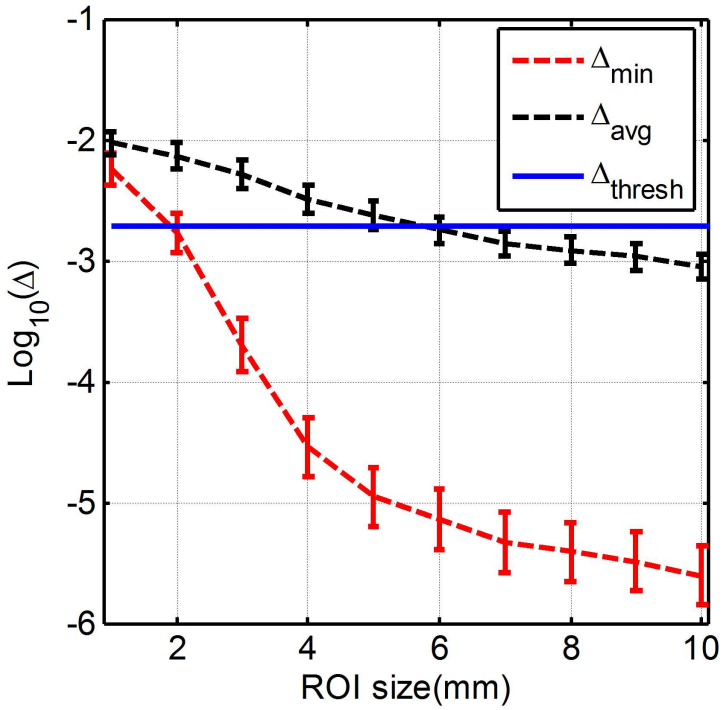

Figure 2.4: Plotted are means and standard errors of minimum ($\Delta_{\min}$) and average (Δ_{avg}) cumulative echo decorrelation values within different ROI sizes for the controlled group; the blue line represents the ablation control threshold.

Representative ablation results from the controlled HIFU ablation trials, as well as from uncontrolled comparison trials, are shown in Fig. 2.5. For each of eight trials, the cumulative corrected echo decorrelation and IBS maps are shown superimposed on a B-mode image from the end of the trial, together with a co-registered map of the vitally stained, segmented tissue histology. Left and right columns show results from trials ablated with average and maximum acoustic powers 26.6 W (*in situ* intensity $I_{\mathrm{SPTP}} = 1192$ W/cm^2) and 31 W ($I_{\mathrm{SPTP}} = 1385$ W/cm^2) respectively. Rows show two representative trials for the controlled (a, b), 2-cycle (c, d), 5-cycle (e, f) and 9-cycle (g, h) groups. In the TTC-stained tissue sections (left), red and green lines indicate segmented tissue boundaries and ablated regions respectively. In each echo decorrelation image (middle), the $\log_{10}$-scaled ablation control threshold -2.7 ($\log_{10}$-scaled decorrelation per ms) is indicated by a yellow dashed line, while white lines indicate tissue boundaries segmented from the B-mode images. In each IBS image (right), the dB-scaled threshold (3.3 dB) corresponding to 90% specificity, for local ablation prediction, calculated from the preliminary experiments ($N = 13$), is indicated by a yellow dashed line. The RMS image registration error measured for all controlled and uncontrolled trials was 0.67 mm, while the mean registration error was 0.52 mm with a 95% confidence interval of 0.47–0.57 mm. Lesion dimensions (width, depth, and area) of the representative trials are close to the reported means for each group, as shown in Fig. 2.7(a)–(d).

ROC curves computed for the four experimental groups are shown in Fig. 2.6 for echo decorrelation (a) and IBS (b) local ablation prediction, respectively. Statistical results for pair-wise AUC comparisons between all groups for echo decorrelation and IBS imaging are shown in Table 2.1. For echo decorrelation ablation prediction (Fig. 2.6(a)), all AUC values were significantly greater than chance, including the controlled group (AUC = 0.952, $p < 10^{-16}$) as well as the 5-cycle (AUC = 0.976, $p < 10^{-16}$), 9-cycle (AUC = 0.979, $p < 10^{-16}$), and 2-cycle (AUC = 0.722, $p = 0.012$) uncontrolled groups. No significant differences occurred between AUC values for the controlled, 9-cycle, and 5-cycle groups

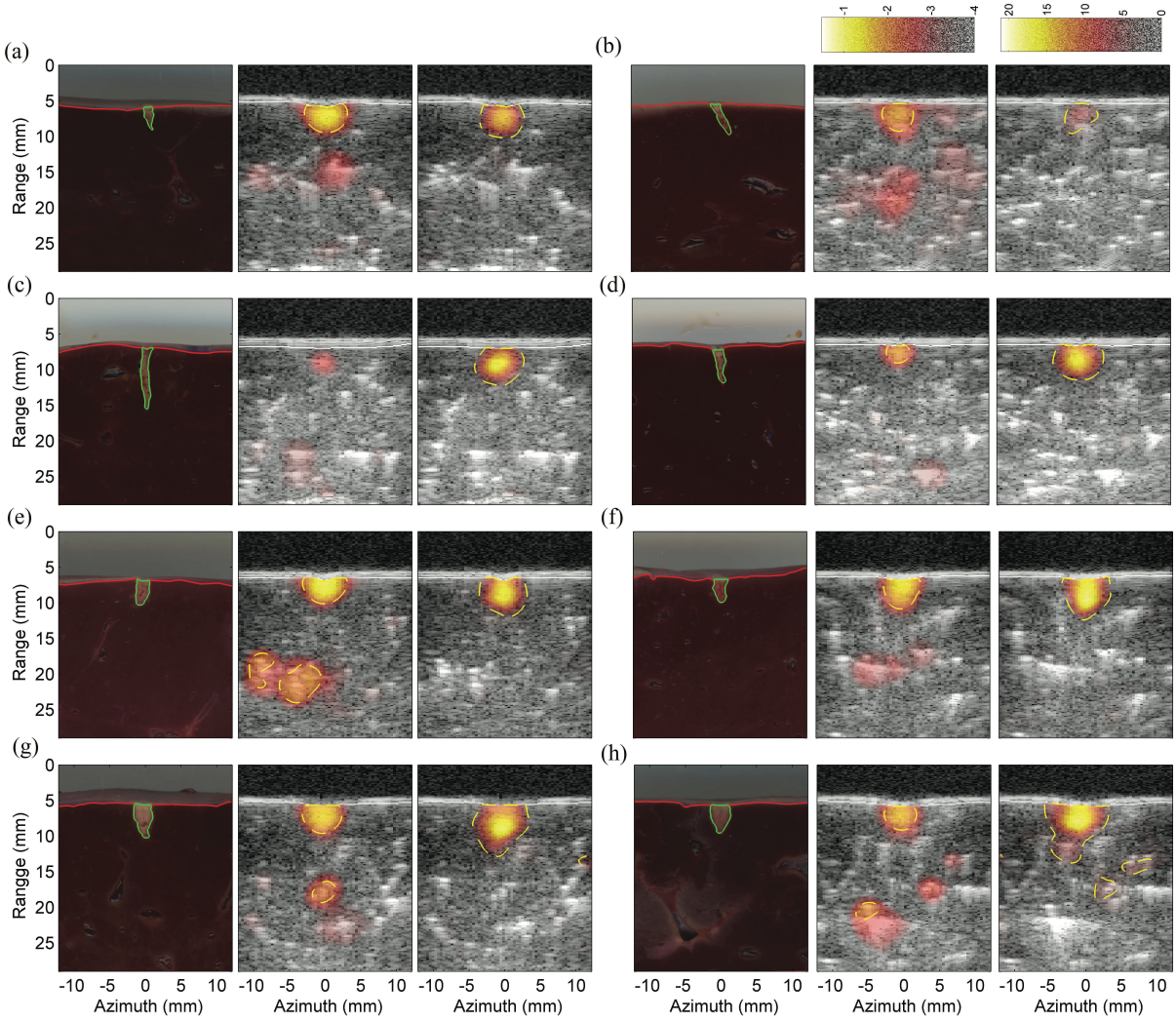

Figure 2.5: Representative histologic and ultrasound images for the controlled and uncontrolled HIFU thermal ablation trials. Each panel shows the vital-stained histologic section (left), the $\log_{10}$-scaled corrected cumulative echo decorrelation (middle), and the dB-scaled cumulative IBS (right) for one trial from the controlled (a, b), 2-cycle (c, d), 5-cycle (e, f) and 9-cycle (g, h) groups. Left and right columns represent trials employing the average and maximum acoustic intensities respectively. Lesion dimensions (width/depth/area) are close to the reported means for each group. The white line indicates tissue boundaries segmented in the B-mode images. In the echo decorrelation images, the control threshold for ablation prediction ($\log_{10}$-scaled echo decorrelation per millisecond: -2.7) is represented by the yellow dashed line. In the IBS images, the threshold for 90% specificity of ablation prediction in preliminary experiments (IBS threshold 3.3 dB) is represented by the yellow dashed line. In the tissue sections, the red and green boundaries indicate the segmented tissue and ablated regions.

($p > 0.3$). However, the 2-cycle uncontrolled group had a significantly smaller AUC value, corresponding to poorer predictive capability, compared to the controlled ($p = 0.042$), 5-cycle ($p = 0.014$), and 9-cycle ($p = 0.012$) groups. For IBS ablation prediction (Fig. 2.6(b)), all AUC values were significantly greater than chance, including the controlled group (AUC = 0.930, $p = 1.1 \cdot 10^{-11}$) as well as the 5-cycle (AUC = 0.981, $p < 10^{-16}$), 9-cycle (AUC = 0.990, $p < 10^{-16}$), and 2-cycle (AUC = 0.839, $p = 2.8 \cdot 10^{-5}$) uncontrolled groups. AUC for the controlled group was statistically equivalent to the 5-cycle, 9-cycle, and 2-cycle uncontrolled groups ($p > 0.3$). Similarly, 5-cycle and 9-cycle uncontrolled groups had statistically equivalent prediction capability ($p = 0.795$). The uncontrolled 2-cycle group had a marginally smaller AUC value than the 5-cycle ($p = 0.109$) and 9-cycle ($p = 0.079$) groups. Statistical results for comparisons between AUC values for echo decorrelation and IBS imaging showed equivalent prediction capability for the controlled, 2-cycle, 5-cycle, and 9-cycle groups ($p > 0.2$).

Optimal thresholds for local ablation prediction and their corresponding sensitivities and specificities for echo decorrelation and IBS imaging are summarized in Table 2.2. For the controlled group, echo decorrelation imaging had slightly higher specificity and lower sensitivity for ablation prediction compared to IBS. However, for all uncontrolled trials, IBS had higher sensitivity and specificity than echo decorrelation imaging for prediction of local tissue ablation.

The optimal threshold for prediction of ablated areas ($N = 40$) using echo decorrelation imaging was -1.8 ($\log_{10}$-scaled decorrelation per ms), corresponding to a minimum RMS area error of 5.51 mm^2. For integrated backscatter imaging, the threshold was 13.2 dB, corresponding to a minimum RMS area error of 5.84 mm^2. For echo decorrelation area prediction, RMS error and NRMSE were 4.32 mm^2 (87.9%) for the controlled group, 6.48 mm^2 (92.4%) for the 5-cycle group, 5.29 mm^2 (56.9%) for the 9-cycle group, and 5.72 mm^2 (99.4%) for the 2-cycle group. For IBS area prediction, RMS error and NRMSE were 4.16 mm^2 (84.6%)

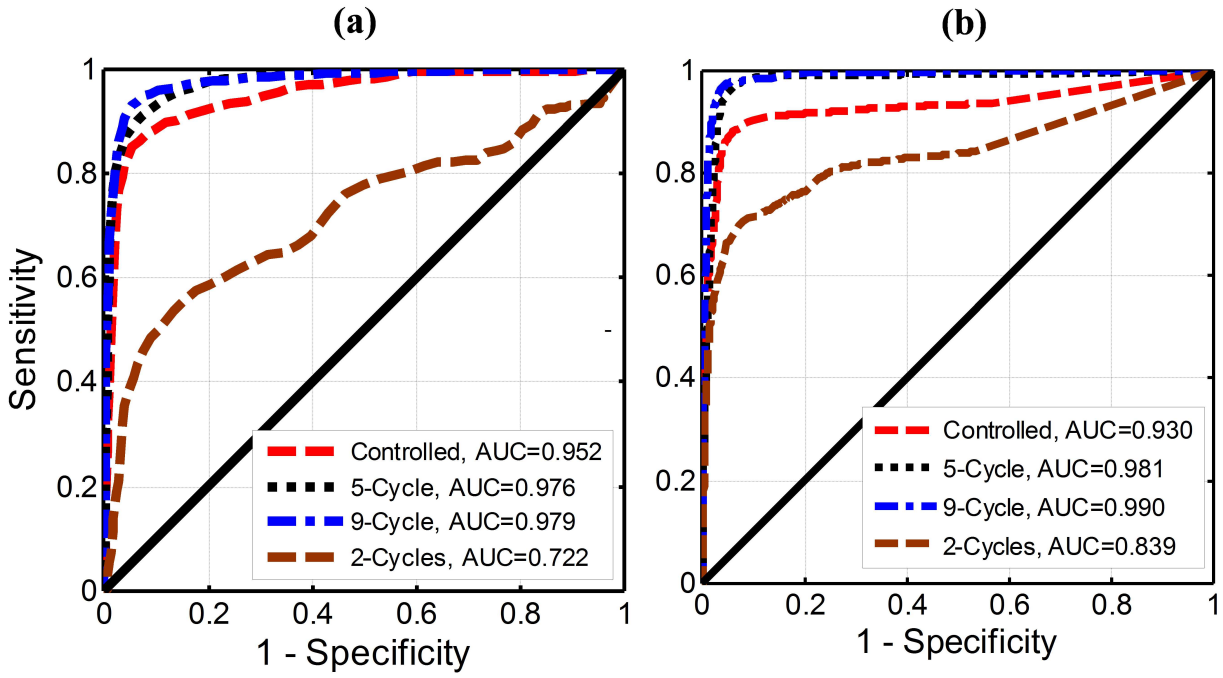

Figure 2.6: ROC curves showing performance of (a) echo decorrelation and (b) IBS imaging as an ablation predictor for each group.

Table 2.1: Results of two-tailed z tests comparing AUC values for echo decorrelation and IBS prediction of local ablation for all HIFU groups.

Echo decorrelation imaging			
	Controlled	5-cycle	9-cycle
5-cycle	−0.40 (0.690)		
9-cycle	−0.47 (0.641)	−0.07 (0.944)	
2-cycle	2.04 (0.042)	2.45 (0.014)	2.53 (0.012)
IBS imaging			
5-cycle	−0.73 (0.468)		
9-cycle	−0.90 (0.368)	−0.26 (0.795)	
2-cycle	0.861 (0.389)	1.60 (0.109)	1.76 (0.079)

Table 2.2: Optimal ablation prediction threshold and corresponding sensitivities and specificities for echo decorrelation ($\log_{10}$-scaled per ms) and IBS (decibel-scaled) imaging for the four HIFU experimental groups.

Echo decorrelation imaging				
Groups	Controlled	5-cycle	9-cycle	2-cycle
Optimum threshold	−3.3	−2.9	−3.0	−4.3
Sensitivity (%)	87.7	91.6	93.3	58.8
Specificity (%)	91.9	92.5	94.6	79.9
IBS imaging				
Groups	Controlled	5-cycle	9-cycle	2-cycle
Optimum threshold	1.6	3.9	5.1	0.8
Sensitivity (%)	89.8	95.9	97.1	73.8
Specificity (%)	91.7	95.1	96.0	86.2

for the controlled group, 7.61 mm^2 (108.4%) for the 5-cycle group, 6.18 mm^2 (66.5%) for the 9-cycle group, and 4.80 mm^2 (83.4%) for the 2-cycle group.

Statistics of segmented lesion dimensions for controlled and uncontrolled trials are shown in Fig. 2.7(a)–(d). For lesion width (Fig. 2.7(a)), means ± standard errors were 1.29 ± 0.10 mm for the controlled group, 1.89 ± 0.09 mm for the 5-cycle group, 2.40 ± 0.11 mm for the 9-cycle group, and 1.01 ± 0.08 mm for the 2-cycle group. The lesion width passed the Shapiro-Wilk normality test ($p > 0.05$). The null hypothesis of the ANOVA test was rejected ($p = 1.3 \cdot 10^{-11}$), indicating a significant difference among lesion widths for the four groups. Pairwise comparisons of mean lesion widths from the Tukey HSD test are shown in Table 2.3. The controlled group had significantly smaller mean lesion width than the 5-cycle or 9-cycle uncontrolled groups, but statistically equivalent lesion width compared to the 2-cycle uncontrolled group. The mean width of the 9-cycle group was significantly larger than the 2-cycle and 5-cycle groups, while the mean width of the 5-cycle group was also significantly larger than the 2-cycle group. Results of the Bartlett test showed no significant difference between variances of the lesion width among all groups ($p = 0.892$).

For the lesion depth (Fig. 2.7(b)), mean ± standard error values were 4.39 ± 0.31 mm for the controlled group, 4.28 ± 0.30 mm for the 5-cycle group, 4.66 ± 0.24 mm for the 9-cycle group, and 6.28 ± 0.49 mm for the 2-cycle group. The null hypothesis of the Shapiro-Wilk test was rejected ($p = 4.5 \cdot 10^{-3}$), indicating a non-normal data distribution. Median ablation depths for the controlled, 5-cycle, and 9-cycle groups were not significantly different based on the Kruskal-Wallis rank-sum test ($p > 0.05$). Median depth for the 2-cycle group was not significantly larger than the 9-cycle group ($p = 5.9 \cdot 10^{-2}$), but was significantly larger than the controlled group ($p = 7.1 \cdot 10^{-3}$) and the 5-cycle group ($p = 4.2 \cdot 10^{-3}$). Results of the Levene test indicated no significant difference in the lesion depth variance among all four groups ($p = 0.218$).

For the segmented lesion area (Fig. 2.7(c)), mean ± standard error values were 4.8 ± 0.47 mm^2 for the controlled group, 7.0 ± 0.56 mm^2 for the 5-cycle group, 9.3 ± 0.58 mm^2 for the 9-cycle group, and 5.6 ± 0.61 mm^2 for the 2-cycle group. Lesion area passed the normality test ($p > 0.05$). The ANOVA test indicated a significant difference among the lesion areas for all groups ($p = 9.31 \cdot 10^{-6}$). Pairwise comparisons of mean lesion areas from the Tukey HSD test are shown in Table 2.4. As for the lesion width, controlled trials had mean lesion area significantly smaller than the 5-cycle or 9-cycle uncontrolled trials but statistically equivalent to the 2-cycle uncontrolled trials. Mean lesion area for the 9-cycle uncontrolled group was also significantly larger than the 2-cycle and 5-cycle uncontrolled groups. Variances of lesion area were not significantly different among the four groups ($p = 0.807$).

Table 2.4: Results of unpaired, two-tailed t-tests comparing measured thermal lesion areas (t statistic (p value)).

	Controlled	5-cycle	9-cycle
5-cycle	2.84 (0.036)		
9-cycle	5.72 ($9.5 \cdot 10^{-6}$)	2.88 (0.032)	
2-cycle	1.06 (0.714)	1.77 (0.302)	4.66 ($2.4 \cdot 10^{-4}$)

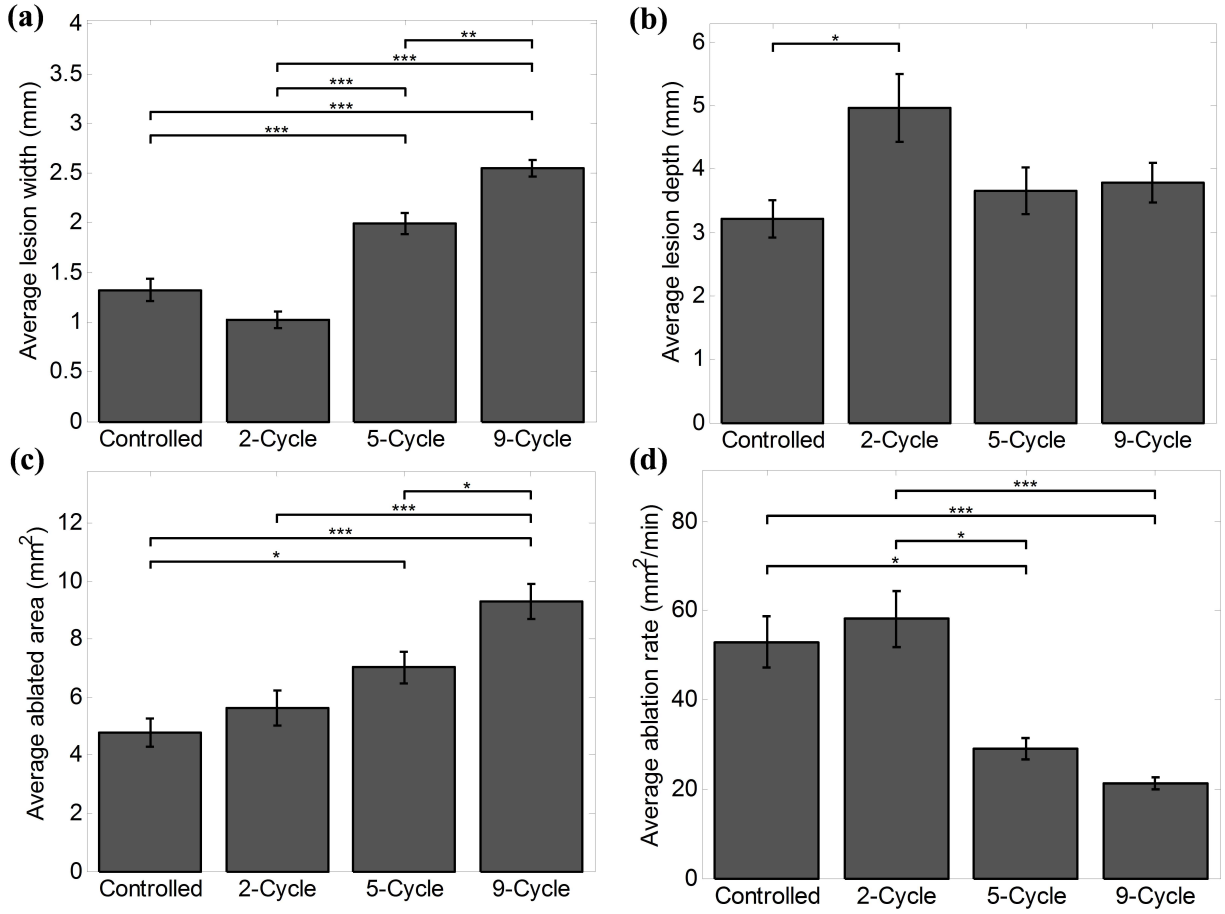

Figure 2.7: Means and standard errors of lesion (a) width, (b) area, (c) depth and ablation rate. ($* \; p < 0.05$, $** \; p < 10^{-2}$, and $*** \; p < 10^{-3}$)

Table 2.3: Results of unpaired, two-tailed t-tests comparing thermal lesion widths (t statistic (p value)).

	Controlled	5-cycle	9-cycle
5-cycle	4.33 ($6.3 \cdot 10^{-4}$)		
9-cycle	8.01 ($<10^{-16}$)	3.67 (0.004)	
2-cycle	-2.05 (0.188)	6.38 ($1.3 \cdot 10^{-6}$)	10.06 ($<10^{-16}$)

For the ablation rate (Fig. 2.7(d)), mean ± standard error values were 52.9±5.8 mm^2/min for the controlled group, 29.1 ± 2.3 mm^2/min for the 5-cycle group, 21.4 ± 1.4 mm^2/min for the 9-cycle group, and 58.2 ± 6.3 mm^2/min for the 2-cycle group. The null hypothesis of the Shapiro-Wilk test was rejected ($p = 7.0 \cdot 10^{-4}$), indicating a non-normal data distribution. Median ablation rates for the controlled, 5-cycle, 9-cycle and 2-cycle groups were significantly different based on the Kruskal-Wallis rank-sum test ($p = 3.4 \cdot 10^{-6}$). Median ablation rate for the controlled group was not significantly less than the 2-cycle group ($p > 0.05$), but was significantly larger than the 5-cycle group ($p = 0.028$) and the 9-cycle group ($p = 6.5 \cdot 10^{-5}$). Median ablation rate for the 2-cycle group was significantly larger than the 5-cycle group ($p = 0.012$) and the 9-cycle group ($p = 1.9 \cdot 10^{-5}$).

Results of the Levene test indicated significant difference in the lesion ablation rate variance among all four groups ($p = 0.048$). The controlled group had significantly greater variances than the uncontrolled 5-cycle ($p = 0.012$) and 9-cycle ($p = 2.0 \cdot 10^{-4}$) groups. The uncontrolled 2-cycle group had significantly greater variances than the uncontrolled 5-cycle ($p = 6.3 \cdot 10^{-3}$) and 9-cycle ($p = 9.2 \cdot 10^{-5}$) groups. Variance for the controlled group was slightly smaller but statistically equivalent compared to the 2-cycle uncontrolled group. Also, there was no significant difference between the variances of the 9-cycle and 5-cycle uncontrolled groups.

2.4 Discussion

This chapter evaluated the potential of echo decorrelation imaging as a feedback approach for real-time control of HIFU thermal ablation in *ex vivo* bovine liver. Our methods and results can be compared with a similar recent study, in which Takagi et al. [84] controlled HIFU exposures in *ex vivo* chicken breast. In that study, tissue coagulation was detected in real-time during HIFU treatment by computing the cross-correlation of echo signals during HIFU treatment with reference signals recorded before treatment. In contrast to the study

reported here, Takagi et al. used separate transducers for therapy (1.25 MHz, 128 element, geometrically focused HIFU array) and for imaging (3 MHz sector-format array placed in the center of the HIFU array). They computed cross-correlation maps over longer time scales (minimum 0.3 s, maximum > 5 s inter-frame time between cross-correlated frames), compared to the short time scales (8.6 ms inter-frame time) employed for decorrelation computations here. They also employed larger dimensions for the control ROI (10×10 mm^2 vs 1×1 mm^2). They observed more homogeneous multi-focal lesions when using treatment feedback control with correlation-coefficient thresholds 0.7 or 0.8, compared to the threshold of 0.9. Average exposure times for each focal lesion were found to range from 4.5–7.8 s for controlled exposures using correlation-coefficient thresholds 0.7, 0.8, and 0.9, comparable to the average exposure time for the controlled group here (5.8 ± 1.9 s). They noted the need for more systematic investigation of optimal control thresholds to judge complete tissue coagulation. Notably, the large inter-frame time used for cross-correlation calculations used in their method can be expected to lessen the specificity of ablation detection in the presence of tissue motion *in vivo*.

Based on the preliminary *ex vivo* experiments reported here ($N = 13$), the echo decorrelation threshold to achieve 90% specificity in predicting local liver ablation was found to be -2.7 ($\log_{10}$-scaled decorrelation per ms). Analogous thresholds for 90% specificity prediction of *in vivo* ultrasound ablation were found by Fosnight et al. [33] to be -2.9 for rabbit liver parenchyma and -2.3 for VX2 tumor within rabbit liver. Sensitivity of local ablation prediction in the preliminary *ex vivo* experiments reported here was 83% at this control threshold, higher than the corresponding sensitivities found previously for both ablated liver (65%) and VX2 tumor (43%) *in vivo* [33]. These discrepancies may be associated with differences between *ex vivo* and *in vivo* ablation, including changes in thermal energy deposition due to blood perfusion and tissue motion. Consequently, longer sonication times [113] may be

required for feedback-controlled HIFU ablation *in vivo* employing the decorrelation thresholds determined here. Other considerations for *in vivo* and clinical controlled ablation are described later in this section.

ROC curves for ablation prediction by echo decorrelation imaging, shown in Fig. 2.6(a), are consistent with previous studies on echo decorrelation monitoring of HIFU thermal ablation [33, 54], with statistically significant prediction of local tissue ablation in every case. Notably, the overall AUC value for controlled HIFU ablation trials (0.952) was significantly higher than for the uncontrolled 2-cycle group (0.722), even though the average sonication time was the same for both groups (5.8 s). The likely reason is that for controlled trials, the minimum cumulative echo decorrelation $\Delta(y, z, m)_{\text{cum}}$ within the ROI exceeded the control threshold Δ_{thresh}, chosen to predict local ablation with 90% specificity, in every case. However, in the 2-cycle group, six of the ten trials failed to meet this threshold within the same ROI. A representative ablation result from a 2-cycle trial failing to meet this threshold is shown in Fig. 2.5(c). In contrast, the AUC value for the controlled group was slightly lower but statistically equivalent to that for the 5-cycle and 9-cycle groups (AUC = 0.976 and 0.979 respectively). For the 5-cycle and 9-cycle groups, the minimum $\Delta(y, z, m)_{\text{cum}}$ within the ROI exceeded Δ_{thresh} in all cases, resulting in effective ablation prediction. In addition, the larger lesion areas obtained from longer HIFU exposures resulted in fewer false-positive predictions of local ablation at focal zone, thus slightly increasing AUC for these groups. Substantial false-positive predictions were found outside the focal zone in 30–50% of controlled and uncontrolled trials due to decorrelation artifacts. One likely source of these artifacts is the presence of air-filled cavities in the *ex vivo* tissue, which can move due to US radiation force during sonication. These artifacts did not affect the present control algorithm because of the small dimensions of control ROI (1×1 mm^2), which was placed at the focal position. These artifacts are likely not relevant to *in vivo* echo decorrelation imaging, because air cavities do not normally exist within the living liver. ROC values for all groups remained high despite

these artifacts because high fractions of the ablated and unablated points were still predicted correctly, corresponding to high prediction sensitivity and specificity respectively.

Local ablation prediction using IBS imaging was significantly better than chance for all groups. IBS imaging showed statistically equivalent performance compared to echo decorrelation imaging in predicting local tissue ablation. Although treatments were controlled based on echo decorrelation feedback, ablation prediction performance of IBS was also improved for the controlled group, relative to the 2-cycle uncontrolled group. This improvement likely occurred because controlled treatments stopped when high decorrelation due to thermal coagulation occurred at the focal zone, usually accompanied by hyperechoic activity (higher echo signal energy). IBS ablation prediction specificity at the optimum thresholds was slightly lower than echo decorrelation specificity for the controlled group, but slightly higher than echo decorrelation prediction specificities for all uncontrolled groups.

For ablated area prediction, high threshold values were found to minimize RMS error for both echo decorrelation ($\log_{10}$-scaled decorrelation per ms: -1.8) and IBS prediction (13.2 dB), possibly because of the small HIFU lesion sizes and low spatial resolution of the parameter maps. Echo decorrelation and IBS under-predicted regions of ablation for most trials in the controlled, 5-cycle, and 2-cycle uncontrolled groups. However, better area prediction capability was observed for 9-cycle uncontrolled trials, possibly due to larger ablation area compared to the controlled, 5-cycle, and 2-cycle groups.

Sensitivity of the control algorithm to ROI size was assessed for the controlled trials, as shown in Fig. 2.4. Smaller ROI sizes ($\leq$ 2 mm) showed small differences between the minimum decorrelation Δ_{min} and the average decorrelation Δ_{avg} within the ROI. However, larger ROIs resulted in much smaller Δ_{min} than Δ_{avg} values. Thus, when Δ_{min} is employed as a control end point as in the present study, a small ROI size is appropriate. When Δ_{avg} is used as a control end point, as done by others [84], a larger ROI may also be usable; however, large ROIs may be more susceptible to echo decorrelation artifacts outside the focal region.

Smaller and more consistent thermal lesion areas were obtained here in the controlled ablation trials (lesion area mean ± standard error 4.8 ± 0.47 mm^2) than in the 5-cycle (7.0 ± 0.56 mm^2), 9-cycle (9.3 ± 0.58 mm^2), or 2-cycle (5.6 ± 0.61 mm^2) uncontrolled trials. A reason for the apparently more consistent thermal lesioning in controlled trials is that echo decorrelation control may automatically compensate for tradeoffs between acoustic intensities and sonication times required for thermal ablation [114]. Another possible reason is that the control algorithm may have ceased HIFU treatments either before significant heat-induced tissue vaporization (boiling) occurred, or soon after the onset of any vaporization. Consistent with this interpretation, the control threshold employed here (-2.7 $\log_{10}$-scaled echo decorrelation per ms) corresponds approximately to the optimal threshold previously found for prediction of temperatures > 80°C in *ex vivo* radiofrequency ablation [92]. These results suggest that HIFU treatments controlled by echo decorrelation imaging can provide consistent, reproducible, completely ablated thermal lesions regardless of changes in the tissue heating rate, which may be caused by differences in the delivered acoustic power, distortion of the HIFU beam, or variations in tissue properties.

The trials reported here included only individual HIFU exposures, with no mechanical or electronic scanning to create larger lesions. However, the results obtained here have implications for scanned HIFU ablation to create larger thermal lesions. The controlled group showed thermal lesions with significantly smaller average area (4.8 mm^2), width (1.29 mm), and treatment time (5.8 s), as well as higher average ablation rate (52.9 mm^2/min) than the 5-cycle (7.0 mm^2, 1.89 mm, 14.5 s, 29.1 mm^2/min) or 9-cycle (9.3 mm^2, 2.4 mm, 26.1 s, 21.4 mm^2/min) uncontrolled trials. These results suggest that HIFU ablation controlled by echo decorrelation imaging may be capable of ablating target volumes in shorter-duration procedures compared to uncontrolled ablation. For instance, based on average lesion widths from the present study, a target region of 10 mm width within the image plane could be ablated using an estimated 8 lesions performed by controlled ablation (46.4 s), compared to

6 lesions using 5-cycle uncontrolled ablation (87 s) or 5 lesions using 9-cycle uncontrolled ablation (130.5 s).

Scanning of HIFU exposures using control by echo decorrelation imaging is anticipated to provide uniform thermally coagulated volumes [84] by automatically varying HIFU exposure time as needed. With HIFU exposure times controlled to achieve consistent echo decorrelation, and thus consistent ablation of each focal lesion, heat accumulation induced by successive HIFU exposures will also be more consistent [84], avoiding undesired over- or under-treatment [115]. The present control algorithm can be straightforwardly extended to monitor and control multiple HIFU lesions [55] using echo decorrelation imaging by consecutively placing control ROIs for individual HIFU exposures filling the targeted region.

For future *in vivo* experiments testing HIFU ablation control by echo decorrelation imaging, real-time correction for artifactual decorrelation caused by tissue motion and electronic noise will be needed. A motion and noise compensation method already established for echo decorrelation imaging [33, 70] can be integrated with the present control algorithm by utilizing the computed cumulative echo decorrelation from sham treatments preceding HIFU sonication. In the case of extracorporeal HIFU treatments, respiratory gating may also be useful to reduce motion effects, both for accurate placement of HIFU foci and for accurate monitoring [116, 117]. In Chapter 4, the later method for motion and noise compensation [70] is tested in real-time, for correcting echo decorrelation maps used to control *in vivo* US thermal ablation.

As implemented here, the real-time control algorithm using echo decorrelation imaging provided feedback at a frame rate of 0.34 Hz, the inverse of the 2.9 s sonication cycle length. Temporal resolution of this method could be improved by computing decorrelation using fewer frames of echo data, which would reduce the time consumed in data acquisition, transfer and computation. For example, on the system employed here, acquiring five RF frames instead of 20 frames per cycle would allow echo data acquisition, processing, and transfer

to occur in 0.33 s (17% of the currently required time), thus reducing the rest period of each sonication cycle to 0.63 s (29% of its current length) and increasing the feedback frame rate to 0.76 Hz. Temporal resolution could also potentially be improved by shortening the duration of each sonication pulse, with the tradeoff of a smaller HIFU duty cycle.

Other considerations important for *in vivo* use of this control algorithm include the accuracy of HIFU ablation near critical tissue structures such as the hepatic vein and bile ducts. In addition to use of the present control algorithm to ensure ablation within targeted ROIs, distinct ROIs could be defined to include critical structures meant to be spared from thermal ablation. In this context, the control algorithm would cease HIFU exposures if the maximum cumulative echo decorrelation within the safety ROI exceeded the control threshold.

2.5 Conclusions

HIFU ablation of *ex vivo* bovine liver tissue was successfully controlled using real-time echo decorrelation imaging feedback. Controlled treatments ablated liver tissue more precisely and in less treatment time than uncontrolled 5-cycle or 9-cycle HIFU treatments. Compared to 2-cycle uncontrolled treatments, controlled treatments provided equivalent ablation time but significantly better capability to confirm local ablation. The precise lesions produced by controlled HIFU exposures could be used to ablate larger volumes by electrically or mechanically scanning, while sparing critical tissue structures. This automatic, ultrasound-based control approach may have advantages over current ultrasound-guided HIFU ablation methods employing manual control with visual feedback.

Chapter 3
Optimized echo decorrelation imaging feedback for bulk ultrasound thermal ablation control

3.1 Objectives

Bulk thermal ablation, including radiofrequency ablation (RFA) as well as microwave ablation (MWA) and ultrasound (US) ablation, is an important approach to tumor treatment. Bulk thermal ablation has the advantage of providing larger ablation volume in less treatment time compared to the high-intensity focused ultrasound (HIFU). However, uncontrolled bulk thermal ablation can cause severe damage to nearby structures (e.g., portal vein and hepatic artery) due to overtreatment or inaccurate ablation outcomes due to undertreatment. Hence, to avoid incomplete treatments and cancer recurrence while reducing morbidity, a real-time monitoring and control approach, capable of providing consistent thermal ablation in minimal time, is needed.

In Chapter 2, echo decorrelation imaging was successfully employed to control HIFU thermal ablation using the minimum cumulative echo decorrelation inside a small region of interest (ROI) (1×1 mm^2), placed at the focal zone in *ex vivo* bovine liver [118]. Another previous study employed a large control ROI (10×10 mm^2), with the average decorrelation within that ROI as a stopping criterion for HIFU ablation in *ex vivo* chicken breast [84].

However, this approach can potentially lead to false alarms, due to any decorrelation artifacts outside the focal ablation region. The present study extends the applicability of echo decorrelation imaging to control of bulk ultrasound ablation [119], which is of interest not only as a potential minimally invasive cancer treatment [29, 30, 33], but also as an analog to bulk ablation by RFA and MWA, with comparable lesion sizes and heating rates [29].

In this chapter, two approaches for controlling bulk thermal ablation using echo decorrelation imaging were implemented and assessed in *ex vivo* bovine liver. An optimization method was applied to determine control ROI dimensions and ablation control thresholds (treatment end points) for two different echo decorrelation feedback predictors, based on results of preliminary ablation and imaging experiments. Bulk US thermal ablation was performed by the same image-ablate array used in previous HIFU experiments [118, 120], allowing accurate image registration with treated tissue histology. The array was used to generate unfocused ultrasound, a configuration mimicking other bulk thermal ablation techniques (e.g., RFA and MWA) by ablating larger volumes with slower heating rates, compared to HIFU ablation. Results of controlled ablation experiments and matching uncontrolled experiments were analyzed to compare the effects of the different control criteria and sonication schemes on ablation outcomes, including lesion dimensions, treatment duration, and local ablation prediction.

3.2 Materials and methods

Materials and methods used in the bulk US ablation experiments were similar to the materials and methods previously employed in the HIFU experiments (Section 2.2.2.a–d), and are briefly discussed here.

3.2.1 Feedback control algorithm

To utilize echo decorrelation imaging feedback for controlling bulk US ablation, a real-time control algorithm was implemented using an integrated real-time US imaging and therapy system, similar to a previous study on control of focused ultrasound ablation, described in Chapter 2 [118]. A flow chart of the closed-loop control algorithm is shown in Fig. 3.1(c).

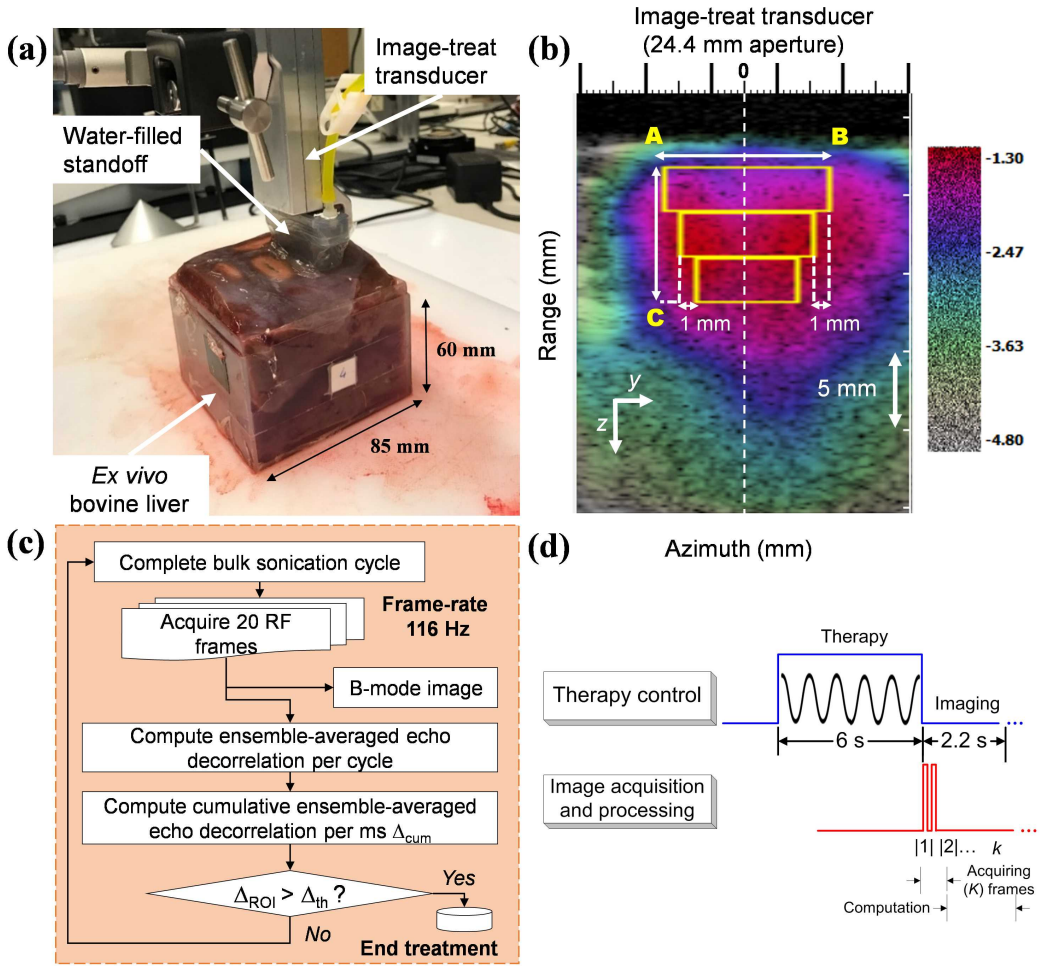

Figure 3.1: Experimental setup. (a) 64-element image-treat array aligned with top surface of *ex vivo* bovine liver. (b) Control geometry for bulk US thermal ablation. The control ROI, bounded by a yellow line, is superimposed on a hybrid B-mode/echo decorrelation image. (c) Feedback control algorithm flow chart. (d) Treatment timing diagram.

Local echo decorrelation per millisecond $\Delta(y, z, t)$ was computed as described in Section 1.5. Derivation and analysis of echo decorrelation imaging has been published previously [70, 88, 89, 118]. Here, the local echo decorrelation was computed between consecutive pulse-echo image frames, recorded immediately after each unfocused sonication cycle. Ensemble-averaged echo decorrelation maps for each cycle were computed (Eq. 1.3). Cumulative echo decorrelation (Δ_{cum}) maps were defined as the temporal maximum of the ensemble-averaged echo decorrelation map for each pixel position (y, z) (Eq. 1.4).

The minimum (Δ_{min}) and average (Δ_{avg}) cumulative echo decorrelation inside a control ROI (Δ_{ROI} in Fig. 3.1(c)) were used as feedback parameters for closed-loop ablation control during two series of ablation experiments. Therapy cycles were repeated until Δ_{min} or Δ_{avg} exceeded a prespecified control threshold Δ_{th} or the sonication cycle index m exceeded a prespecified maximum number of sonication cycles.

3.2.2 Bulk US ablation experiments

Using a custom image-treat array transducer (64-element, 4.8×24.4 mm^2 aperture, 5.0–5.4 MHz; Ardent Sound, Mesa, AZ, USA), pulse-echo US imaging ($> 40\%$ bandwidth, transmit focal depth 3.5 cm, F-number 4) and bulk US ablation (unfocused, maximum acoustic power 35 W) were performed. The transducer was integrated with a 23 mm standoff filled with deionized, degassed ($< 30\%$ dissolved O_2) water. Both US treatment and imaging were controlled by the Iris 2 imaging and therapy system (Ardent Sound, Mesa, AZ, USA) [102].

Fresh bovine liver was obtained from a local slaughterhouse, cut to fit an open-top acrylic cuvette ($85 \times 85 \times 60$ mm^3) as shown in Fig. 3.1(a), and immersed in deionized, degassed 0.01M phosphate-buffered saline (PBS). All tissue was treated within 12 hours *post mortem*. The tissue baseline temperature prior to ablation was 19.0–21.5 °C.

For bulk US treatments, high-intensity sonication cycles were performed, following the timing sequence shown in Fig. 3.1(d). The array fired full-aperture, continuous-wave, unfocused 6 s pulses with an estimated [100] range of *in situ* spatial-peak, temporal-peak intensity (I_{SPTP}) from 24 to 54 W/cm^2 (5% less than the range used in [33]), followed by rest periods of 2.2–2.5 s. The corresponding estimated pressure amplitude range (0.85–1.30 MPa, 5.0 MHz) was less than the threshold of subharmonic emissions (1.68 MPa, 5.0 MHz) for resonant-sized bubbles in blood [121], which ensured minimal acoustic cavitation in tissue, although some cavitation and other gas activity likely occurred as tissue was heated [89].

Immediately after each sonication cycle, 20 frames of beamformed radiofrequency echo data were acquired at a frame rate of 116 Hz. Frames were digitized by a PC-based data acquisition card (14-bit, 33.3 MHz sampling rate; Compuscope 14200, Gage Applied). In-phase and quadrature (IQ) complex components of the digitized frames were computed by applying a Hilbert-transform filter, then demodulated using a 5.0 MHz carrier frequency and decimated by a factor of 6. Processed IQ frames were used to compute B-mode and echo decorrelation images, as described previously [33].

After experiments, treated liver tissue was stored overnight in a −80 °C freezer in the same cuvette to maintain tissue shape and orientation for registration with US images. The tissue was sectioned through the imaging/therapy plane, stained with 2% triphenyl tetrazolium chloride (TTC) vital stain [33, 88], and optically scanned at 1200 dpi (CanoScan 8800F, Canon, Tokyo, Japan). Using a custom MATLAB (The MathWorks, Natick, MA, USA) application, scanned sections were manually segmented into ablated (partial or no TTC uptake) or unablated (full TTC uptake) regions and registered with corresponding B-mode US images [89, 118], using a 2D rigid registration method. Estimated root-mean-square (RMS) image registration error for this method is approximately 0.7 mm [118].

3.2.3 Experiments using minimum-decorrelation criterion

The first series of controlled ablation experiments used the minimum cumulative echo decorrelation inside a control ROI as a stopping criterion. This control approach was motivated by the success of echo decorrelation in locally predicting ablation with high specificity [33, 88], potentially enabling echo decorrelation feedback to ensure ablation of the entire control ROI. This control approach also matched that used in a previous series of experiments on HIFU ablation control using echo decorrelation imaging [118]. In these experiments, a constant-intensity sonication scheme was used, similar to the *in vivo* bulk ablation experiments reported by Fosnight et al. [33]. In those previous *in vivo* experiments, the sonication sequence was chosen to ensure successful tissue ablation in all cases, while potentially exceeding the minimum number of treatment cycles required.

In order to specify an appropriate decorrelation threshold and control ROI dimensions, an optimization approach was applied to a preliminary series of uncontrolled bulk US ablation experiments ($N = 30$) on fresh bovine liver tissue, using the experimental setup shown in Fig. 3.1(a) and the ablation methods described in Section 3.2.2. For all 30 trials, nine sham cycles (zero acoustic power) were followed by 7–18 (mean 11.4) identical sonication cycles, covering the ranges of 5.0–5.4 MHz in frequency, 70.6–73.1% in duty cycle, and 24–54 W/cm^2 I_{SPTP}.

The guiding principle of the optimization approach was to seek control criteria such that ablation of an ROI would be confirmed by the minimum value of echo decorrelation in the ROI, with the expectation that ablation may extend to a region beyond the ROI in all directions. The control ROI shape was chosen to approximate an upside-down isosceles trapezoid, matching the observed typical shape of bulk US thermal lesions in these preliminary experiments, as shown in Fig. 3.2(a). For simplicity, the ROI was formed from three rectangles with fixed widths and lateral edges separated by 1 mm on each side, as shown in

Fig. 3.1(b). ROI width (i.e., width of the topmost rectangle) was varied between 10–24 mm in increments of 2 mm, while ROI height (i.e., height of the three combined rectangles) was 9, 12, or 15 mm. Each ROI was placed parallel to the transducer aperture, centered at the midline of the US image (white dashed line in Fig. 3.1(b)), with its top boundary 2 mm below the tissue surface, to reduce influence of the bright reflection from the tissue surface on echo decorrelation within the ROI.

For a number of candidate ROIs of this type, all preliminary trials were classified into ablated-ROI (ROI fully within the ablated region, as shown in Fig. 3.2(a)) and unablated-ROI (ROI not fully within the ablated region, as shown in Fig. 3.2(b)) groups. The minimum of the spatial-average, cumulative echo decorrelation inside the ROI under investigation was computed for each group. In order to determine an ROI suitable for meaningful testing of control efficacy, optimum control ROI dimensions were chosen as those providing a large difference in mean $\Delta_{\min}$ between ablated-ROI and unablated-ROI groups, while also providing a sufficiently large fraction of ablated-ROI trials. The result was selection of a 16 mm $\times$ 12 mm (width $\times$ height) ROI, which was fully ablated in 23.3% of the preliminary trials.

An optimum control threshold was then sought, with the goal of achieving high prediction specificity and reasonable sensitivity for complete ROI ablation. Rates of true-positive (sensitivity) and true-negative (specificity) predictions of complete ROI ablation were computed as a function of $\Delta_{\min}$, as shown in Fig. 3.2(c). The control threshold was selected as $\Delta_{\text{th}} = -3.20$ ($\log_{10}$-scaled echo decorrelation per ms), corresponding to 91.3% specificity and 57.1% sensitivity for prediction of complete ROI ablation.

To assess this first control approach, a series of controlled and uncontrolled ablation experiments were conducted using the same experimental setup shown in Fig. 3.1(a). In controlled trials ($N = 15$), the control ROI was placed 2 mm below the tissue surface, azimuthally centered on the B-mode image as shown in Fig. 3.1(b). The maximum number of sonication cycles for all controlled trials was set to $M = 18$ [118], twice the maximum

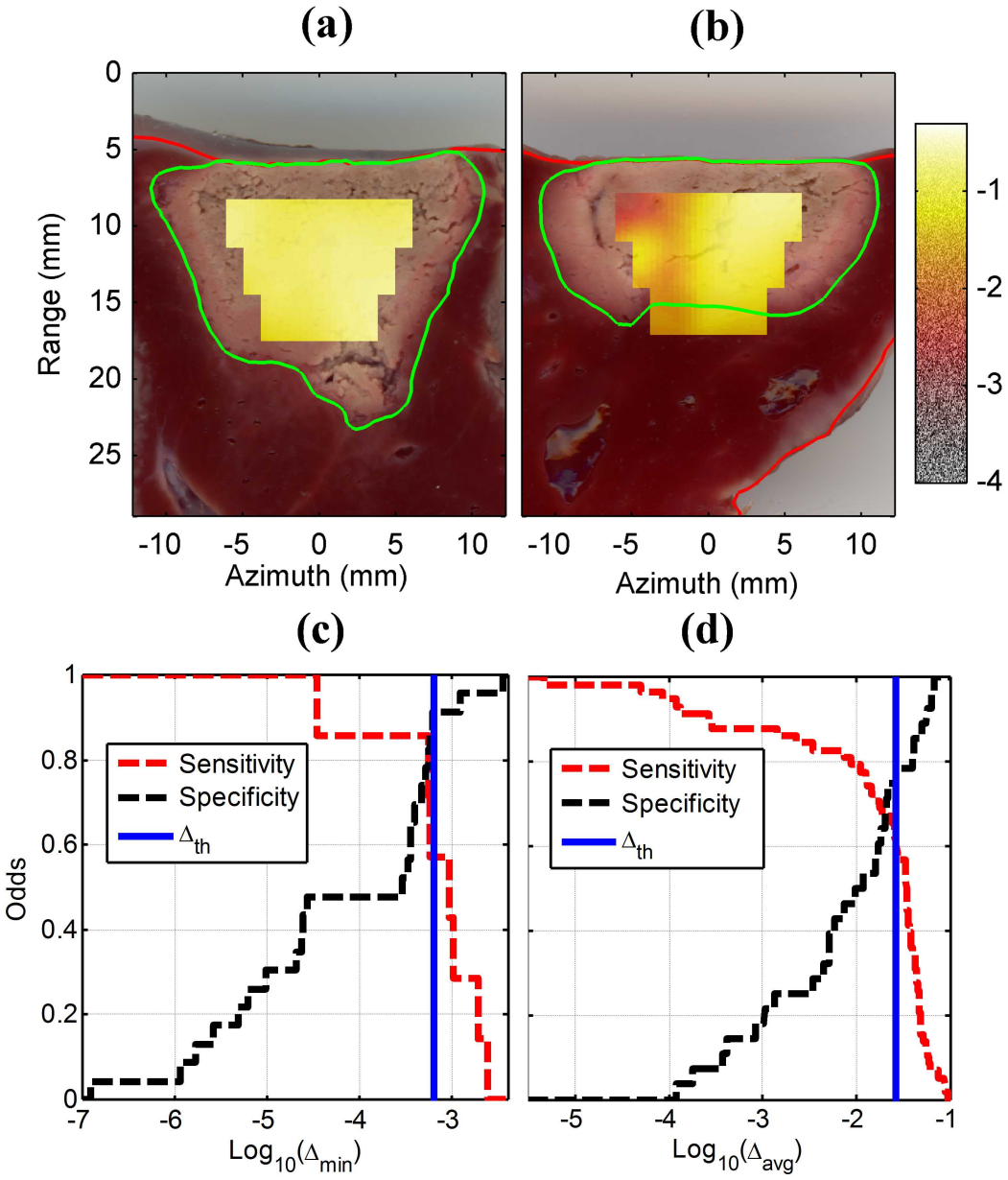

Figure 3.2: Optimization approach for control criteria. Segmented TTC-stained tissue sections of preliminary ablation trials were classified into (a) ablated-ROI and (b) unablated-ROI groups for ROI size selection. Sensitivity and specificity curves for the chosen ROIs were used to optimize Δ_{th} for (c) minimum-decorrelation ($N = 30$) and (d) average-decorrelation ($N = 86$) prediction of complete ROI ablation. The blue line represents the selected ablation control threshold for each approach.

number of sonication cycles used by Fosnight et al. [33] for *in vivo* bulk ultrasound ablation. For the controlled treatments, sonication sequences (73.1% duty cycle, 5.0 MHz frequency) began with 9 sham cycles, followed by constant-intensity sonication cycles (I_{SPTP} range of 38–49 W/cm^2), with treatments ending when the minimum cumulative echo decorrelation Δ_{min} within the ROI exceeded Δ_{th} or when the sonication cycle index m exceeded M. During the rest period of each cycle (2.2 s), echo decorrelation maps were computed and overlaid on the B-mode images. Controlled trials were compared with uncontrolled trials employing 9 ($N = 15$) or 18 ($N = 14$) cycles of the same sonication sequence, as described in Section 3.2.5.

3.2.4 Experiments using average-decorrelation criterion

To test the sensitivity of the closed-loop control algorithm and the proposed optimization method to choice of echo decorrelation feedback predictors, a second series of controlled ablation experiments was performed using the average cumulative echo decorrelation as a stopping criterion, similar to the approach used in another study of HIFU ablation control by echo decorrelation imaging [84].

These experiments also employed variable-intensity sonication (lower-power sonication cycles followed by higher-power cycles) in an attempt to increase the depth of thermal lesioning. The variable sequence started with a series of lower-intensity sonication cycles, followed by a series of higher-intensity sonication cycles, to reduce shadowing effects associated with overtreatment at shallow tissue depths [29]. In these controlled ablation experiments, treatments were terminated once the average echo decorrelation within the control ROI exceeded a predefined threshold.

To optimize the control ROI dimensions and ablation threshold, the approach described in Section 3.2.3 was applied. The preliminary experiments analyzed here comprised the previous preliminary experiments ($N = 30$), controlled trials ($N = 15$), and uncontrolled

trials ($N = 29$) trials described in Section 3.2.3, as well as additional preliminary experiments (N = 12, 9–18 therapy cycles, 73.1% duty, I_{SPTP} = 36.1 W/cm^2, 5.0 MHz). For all 86 preliminary trials analyzed here, nine sham cycles were followed by 7–18 (average 12.3) sonication cycles.

Similar to the optimization approach described in Section 3.2.3, *post hoc* analysis was employed to specify control ROI dimensions, based on successful ablation of the entire ROI and echo decorrelation contrast between ablated-ROI and unablated-ROI groups. ROI widths considered ranged from 12–18 mm with a 2 mm increment, while ROI heights considered were 9 mm and 10.5 mm. The spatially averaged cumulative echo decorrelation inside the ROI under investigation was computed for each group. The optimum ROI dimensions were chosen as 12 mm × 9 mm, corresponding to complete ROI ablation in 67.4% of the preliminary trials. The control threshold was selected as -1.576 ($\log_{10}$-scaled echo decorrelation per ms), corresponding to 78.6% specificity and 60.3% sensitivity for prediction of complete ROI ablation, as shown in Fig. 3.2(d).

To assess the ability of average decorrelation feedback approach for controlling bulk US thermal ablation using the optimized control ROI and threshold, a series of controlled and uncontrolled ablation experiments ($N = 33$) was conducted using the same approach and experimental setup (Fig. 3.1(a)). In the controlled trials ($N = 13$), the control ROI was placed as described in the previous section. For controlled bulk US treatments ($N = 13$), the variable sonication sequence (73.1% duty cycle, 5.4 MHz frequency) began with 9 sham cycles, followed by 9 sonication cycles at 38.3 W/cm^2 I_{SPTP} and up to 9 cycles at 43.1 W/cm^2. This initial lower intensity approximately equals the lowest intensity employed in the constant-intensity sonication sequences described in Section 3.2.2, while the higher intensity approximately equals the average of all constant intensities employed. Treatments ended when the average cumulative echo decorrelation Δ_{avg} within the ROI exceeded Δ_{th} or when the sonication cycle index m exceeded M. Controlled trials were compared with

uncontrolled trials employing 9 ($N = 10$) or 18 ($N = 10$) cycles of the same sonication sequence.

During treatments, the occurrence of audible popping sounds [122] associated with tissue vaporization was noted by the operator, together with the corresponding therapy cycle index, to study the relationship between the popping-sound phenomenon and the average decorrelation Δ_{avg} inside the control ROI. For statistical analysis, trials were classified into audible sound ($N = 17$) and no audible sound ($N = 16$) groups for comparison of Δ_{avg} levels in each group. The same analyses were done for the IBS values inside the control ROI to compare between the behavior of the two imaging methods.

3.2.5 Data Analysis

After treatments, tissue handling and processing followed the procedures described in Section 3.2.2. Segmented TTC-stained tissue sections were used to characterize bulk thermal lesions by their depth, width, and area [118]. Lesion depth was defined as the distance between the most proximal and distal ablated points along the vertical line at zero azimuth of the transducer (white dashed line in Fig. 3.1(b)). Lesion width was defined as the horizontal distance between the left and right edges of the ablated region, measured at the midpoint of the lesion depth. Lesion area was computed as the total area of all pixels in the ablated region. Ablation rate (cm^2/min) was defined as the ablated area divided by the treatment time.

Statistical analysis was done using R software (R Foundation, Vienna, Austria). Means and standard errors of the lesion width, depth, area, treatment time and ablation rate were calculated for all groups. Normality of the data was tested using the Shapiro-Wilk test [123]. For non-normally distributed groups, a Kruskal-Wallis rank sum test [109] (significance criterion $p < 0.05$) was conducted to test the hypothesis of no median difference, followed by

Dunn's test [110] for multiple pairwise comparisons with Bonferroni adjustment [111]. Homogeneity of variances was tested statistically for the normally and non-normally distributed groups using the Bartlett test [124] and Levene test [125], respectively. For normally distributed groups, analysis of variance (ANOVA) was applied to test the hypothesis of equal means. If significant, ANOVA was followed by a *post hoc* Tukey's honest significance difference (HSD) test for multiple comparison of means.

To assess the ablation prediction capability of echo decorrelation and integrated backscatter (IBS) imaging for each group, receiver operating characteristics (ROC) curves and area under ROC (AUC) values were computed for each group [33, 88, 89]. Cumulative echo decorrelation maps were corrected for motion and noise artifacts using a method described previously [33, 70]. ROC curves were computed by comparing the corrected cumulative echo decorrelation and IBS maps to the TTC-segmented tissue binary mask point-by-point, plotting rates of true positive predictions and false positive predictions over all image pixels for all echo decorrelation thresholds as described previously in Section 2.2.2.e. AUC was calculated and statistical significance of AUC values was determined vs. the null hypothesis (AUC = 0.5), vs. each other (controlled vs. uncontrolled), and between the two parameter maps (echo decorrelation vs. IBS) for each group, as previously described in Section 2.2.2.e. AUC statistical tests were adjusted for their effective sample size as previously described in Section 2.2.2.e.

The average lesion width of each group for both approaches was tested against the transducer aperture using one-sample t-tests (two-tailed, significance criterion $p < 0.05$). The average treatment time of each controlled group was tested against the corresponding fixed treatment times of the 9-cycle and 18-cycle uncontrolled groups using one-sample t-tests (two-tailed, significance criterion $p < 0.025$ including Bonferroni correction).

To compare between the minimum-decorrelation and average-decorrelation feedback approaches, lesion dimensions (width and depth), ablation rates, and treatment times of the

successfully controlled trials for each criterion were statistically compared using two-sample t-tests (two-tailed, significance criterion $p < 0.05$). In addition, relative differences between outcomes of controlled and matching uncontrolled trials were compared between the two experimental series.

To assess the ability of echo decorrelation and IBS imaging to predict tissue ablation area, optimal decorrelation and IBS cutoffs for ablation prediction were determined, such that the estimated ablated area was equal to the area of all pixels exceeding the cutoff. RMS errors between measured and estimated ablated areas were calculated, for all groups of both approaches ($N = 70$), for a range of echo decorrelation cutoffs from -4 to -1 ($\log_{10}$-scaled echo decorrelation per ms) and a range of IBS cutoffs from -5 to 30 dB using the echo decorrelation and IBS maps respectively. The echo decorrelation and IBS cutoffs corresponding to the minimum overall RMS ablated area errors were considered the optimum for ablated area prediction. Using these cutoffs, absolute RMS errors and normalized RMS error (NRMSE) were computed for all bulk US groups as described previously in Section 2.2.4.

A retrospective study was also performed to compare performance of the two control criteria investigated. For trials using the minimum-decorrelation feedback approach, the 12 mm $\times$ 9 mm control ROI from the average-decorrelation experiments, together with its associated control threshold ($\Delta_{\text{th}} = -1.576$), were applied to archived echo data from all controlled experiments. For each of these experiments, control using the average-decorrelation feedback criterion was simulated by computing Δ_{avg} within the control ROI for each cycle. The *post hoc* threshold-crossing time for each trial (i.e., the treatment time if the average-decorrelation feedback criterion had been employed) was defined as the number of therapy cycles required to exceed the alternative control threshold, multiplied by the therapy cycle duration (8.2 s). Similarly, controlled trials employing the average-decorrelation feedback criterion were retrospectively analyzed by applying the 16 mm $\times$ 12 mm control ROI from

the minimum-decorrelation experiments with its selected control threshold ($\Delta_{\text{th}} = -3.20$). Means and standard errors of the *post hoc* threshold-crossing time for all controlled trials of each feedback criterion were computed and statistically compared using two-sample t-tests (two-tailed, significance criterion $p < 0.05$). In addition, all successfully controlled trials using the minimum-decorrelation approach were assessed for complete ablation of the smaller control ROI employed in the average-decorrelation approach. Similarly, all successfully controlled trials using the average-decorrelation approach were assessed for complete ablation of the larger control ROI employed in the minimum-decorrelation approach.

3.3 Results

3.3.1 Experiments using minimum-decorrelation criterion

In the first series of experiments, employing constant-intensity sonication and the minimum-decorrelation stopping criterion, successful control (Δ_{min} exceeding Δ_{th}) was achieved in 11 of the 15 controlled trials (73.3%), with the threshold reached in an average of 9.7 cycles or 79.8 s (maximum 14 cycles or 114.8 s; minimum 7 cycles or 57.4 s). The 16 mm $\times$ 12 mm control ROI was fully ablated in 3 of 11 successfully controlled trials, 0 of 4 unsuccessfully controlled trials, 3 of 15 9-cycle uncontrolled trials, and 3 of 14 18-cycle uncontrolled trials.

Fig. 3.3 and 3.4 show final B-mode image frames, overlaid by final cumulative echo decorrelation and IBS maps, together with corresponding registered and segmented TTC-stained tissue sections for representative trials from the 9-cycle, successfully controlled, and 18-cycle groups. The white line and dashed green lines indicate the segmented tissue boundaries and predicted ablation region boundaries in the hybrid B-mode/echo decorrelation or B-mode/IBS images. In the TTC-stained sections, red and green lines indicate segmented tissue boundaries and ablated regions respectively. Lesion depths for the trials shown in

column (a), (b), and (c) approximately match the minimum, average, and maximum values for each group, respectively.

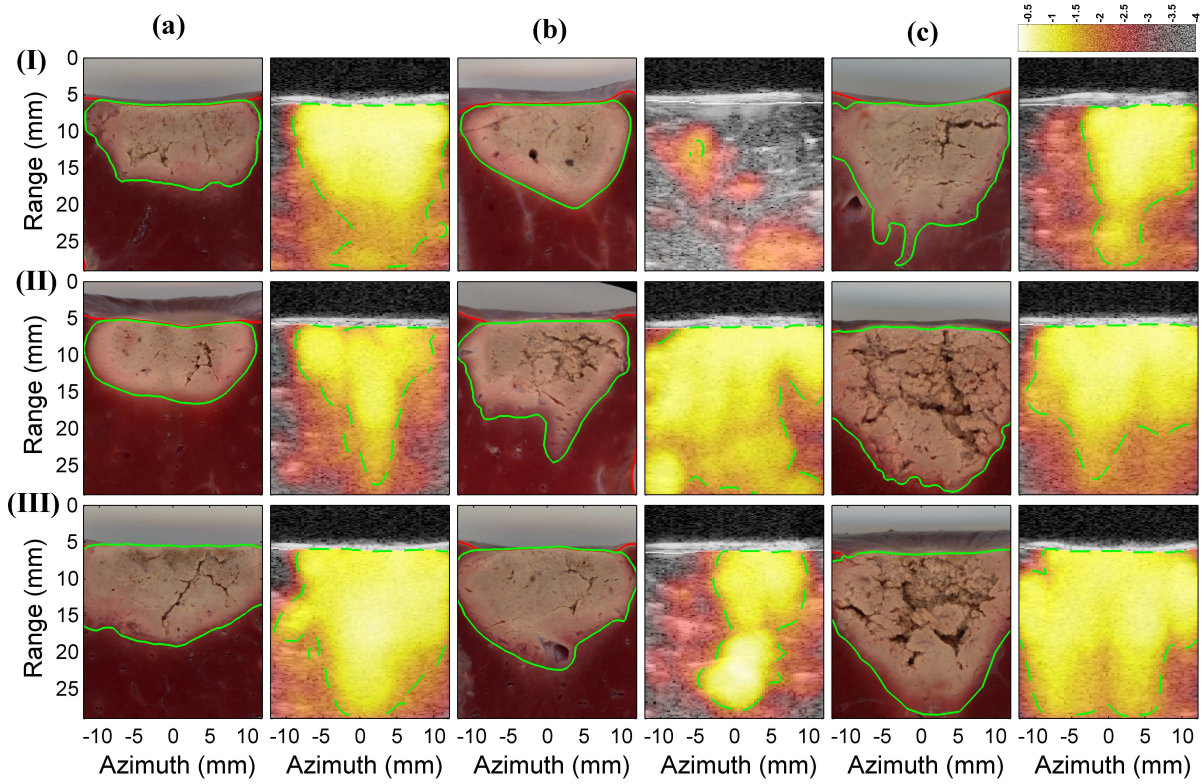

Figure 3.3: Representative histologic and hybrid B-mode/echo decorrelation images for controlled and uncontrolled trials using the minimum-decorrelation feedback approach. Rows (I)–(III) represent 9-cycle uncontrolled, successfully controlled, and 18-cycle uncontrolled trials with segmentation of tissue boundaries and ablated regions. Red and green lines represent segmented tissue and ablation region boundaries, while white and dashed green lines indicate the segmented tissue and predicted ablation region boundaries ($\log_{10}$-scaled decorrelation per ms: -2.6) in the hybrid B-mode/echo decorrelation images. Columns (a)–(c) represent trials with approximately minimum, average, and maximum measured lesion depth for each group.

Fig. 3.5(a), (b) shows ROC curves and AUC values for prediction of local ablation using echo decorrelation and IBS imaging. Statistical results for pairwise AUC comparisons

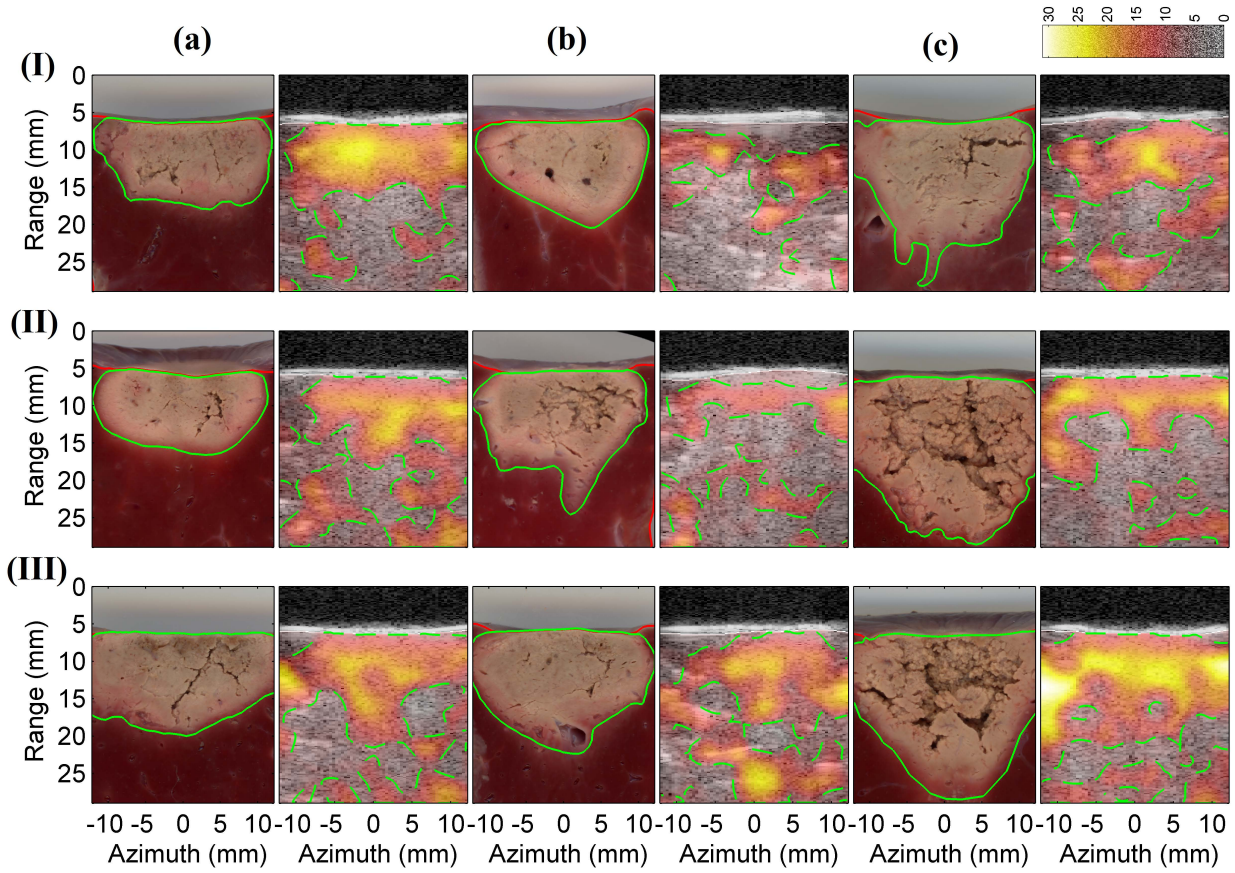

Figure 3.4: Representative histologic and hybrid B-mode/IBS images for controlled and uncontrolled trials using the minimum-decorrelation feedback approach. Rows (I)–(III) represent 9-cycle uncontrolled, successfully controlled, and 18-cycle uncontrolled trials with segmentation of tissue boundaries and ablated regions. Red and green lines represent segmented tissue and ablation region boundaries, while white and dashed green lines indicate the segmented tissue and predicted ablation region boundaries (IBS threshold 4.0 dB) in the hybrid B-mode/IBS images. Trials shown are the same as in Fig. 3.3.

between all groups for echo decorrelation and IBS imaging are shown in Table 3.1. For echo decorrelation ablation prediction (Fig. 3.5(a)), AUC values for the successfully controlled (AUC = 0.862), 9-cycle uncontrolled (AUC = 0.668), and 18-cycle uncontrolled (AUC = 0.842) groups were significantly greater than chance ($p < 10^{-16}$), and were significantly larger for the controlled and 18-cycle groups, compared to the 9-cycle group

($p < 10^{-16}$). For IBS ablation prediction (Fig. 3.5(b)), AUC values for the successfully controlled (AUC = 0.725), 9-cycle uncontrolled (AUC = 0.690), and 18-cycle uncontrolled (AUC = 0.755) groups were significantly greater than chance ($p < 10^{-16}$), and were significantly larger for the 18-cycle groups, compared to the 9-cycle group ($p = 1.3 \cdot 10^{-3}$). Statistical comparisons between echo decorrelation and IBS imaging for the 9-cycle uncontrolled group showed significantly greater AUC for the IBS prediction compared to echo decorrelation imaging ($p < 10^{-16}$). However, echo decorrelation predicted local tissue ablation significantly better than IBS in the successfully controlled and 18-cycle uncontrolled groups ($p < 10^{-16}$).

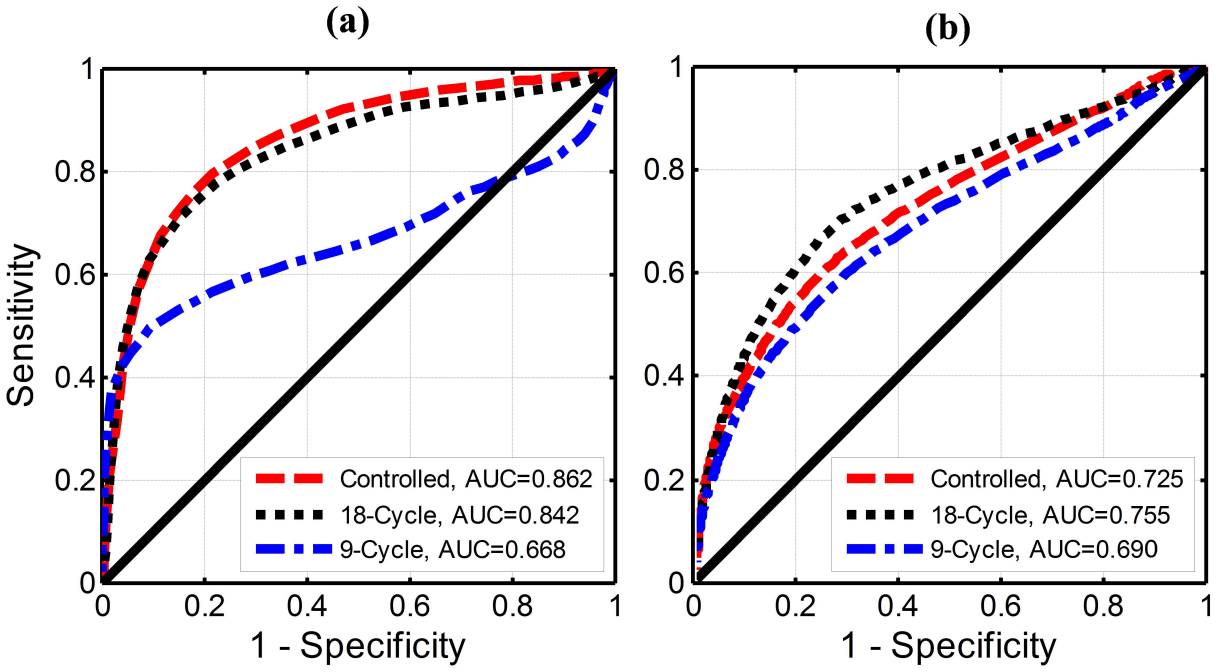

Figure 3.5: ROC curves for (a) echo decorrelation and (b) IBS ablation prediction for successfully controlled, 9-cycle uncontrolled, and 18-cycle uncontrolled groups (AUC: area under ROC curve) using the minimum-decorrelation feedback approach.

Table 3.1: Results of two-tailed z tests comparing AUC values for echo decorrelation and IBS prediction of local ablation among all bulk US groups using the minimum-decorrelation criterion.

Echo decorrelation imaging		
	Controlled	9-cycle
9-cycle	9.48 ($< 10^{-16}$)	
18-cycle	1.21 (0.224)	-9.19 ($< 10^{-16}$)
IBS imaging		
9-cycle	1.61 (0.108)	
18-cycle	-1.42 (0.154)	-3.20 ($1.3 \cdot 10^{-3}$)

Optimal thresholds for local ablation prediction and their corresponding sensitivities and specificities for echo decorrelation and IBS imaging are summarized in Table 3.2. For the controlled and 18-cycle uncontrolled groups, echo decorrelation imaging had higher sensitivity and specificity for local ablation prediction compared to IBS. For the 9-cycle uncontrolled group, echo decorrelation had slightly lower sensitivity and higher specificity than IBS imaging for local tissue ablation prediction.

Fig. 3.6(a)–(d) shows statistics of lesion dimensions and ablation rates for successfully controlled trials and uncontrolled trials employing the minimum-decorrelation, constant-intensity approach. Means $\pm$ standard errors of the lesion width were 23.2 ± 1.0 mm for successfully controlled trials, 21.2 ± 0.8 mm for the 9-cycle group, and 25.2 ± 0.6 mm for the 18-cycle group, as shown in Fig. 3.6(a). For the segmented lesion depth, means $\pm$ standard errors were 14.8 ± 1.1 mm for successfully controlled trials, 13.4 ± 0.7 mm for the 9-cycle group, and 15.5 ± 1.0 mm for the 18-cycle group, as shown in Fig. 3.6(b). For the lesion area, mean $\pm$ standard error values were 3.1 ± 0.3 cm^2 for successfully controlled trials, 2.75 ± 0.1 cm^2 for the 9-cycle group and 3.48 ± 0.2 cm^2 for the 18-cycle group, as shown in Fig. 3.6(c). For ablation rate, mean $\pm$ standard error values were 2.37 ± 0.1 cm^2/min for

Table 3.2: Optimal thresholds for local ablation prediction and corresponding sensitivities and specificities for echo decorrelation ($\log_{10}$-scaled per ms) and IBS (decibel-scaled) imaging for all groups using the minimum-decorrelation criterion.

Echo decorrelation imaging			
Groups	Controlled	9-cycle	18-cycle
Optimum threshold	−2.2	−2.6	−2.2
Sensitivity (%)	79.6	56.6	74.7
Specificity (%)	78.5	78.6	81.6
IBS imaging			
Groups	Controlled	9-cycle	18-cycle
Optimum threshold	5.4	4.0	5.1
Sensitivity (%)	64.2	60.9	69.1
Specificity (%)	70.3	69.0	72.6

successfully controlled trials, 2.23±0.1 cm^2/min for the 9-cycle group, and 1.41±0.1 cm^2/min for the 18-cycle group, as shown in Fig. 3.6(d). For treatment time, mean ± standard error was 79.8 ± 5.9 s for successfully controlled trials, compared to fixed durations of 73.8 s for the 9-cycle group and 147.6 s for the 18-cycle group. For the unsuccessfully controlled trials ($N = 4$), means ± standard errors for the lesion width (23.5 ± 0.9 mm), lesion depth (14.9 ± 0.94 mm), ablated area (3.2 ± 0.2 cm^2), and ablation rate (1.3 ± 0.1 cm^2/min) were close to the 18-cycle uncontrolled trials.

Ablated lesion widths, depths and rates passed the Shapiro-Wilk test ($p > 0.05$), indicating normal data distribution. ANOVA tests showed significant differences between lesion widths and ablation rates ($p = 3.2 \cdot 10^{-3}$, $p = 9.4 \cdot 10^{-8}$, respectively), but no significant differences between ablation depths ($p = 0.23$). Based on Tukey's HSD test, average ablation rate for the 18-cycle group was found to be significantly smaller than for the successfully controlled and 9-cycle groups ($p < 10^{-4}$). Average lesion width for the 9-cycle group was found to be significantly smaller than for the 18-cycle group ($p = 2.2 \cdot 10^{-3}$) and the transducer

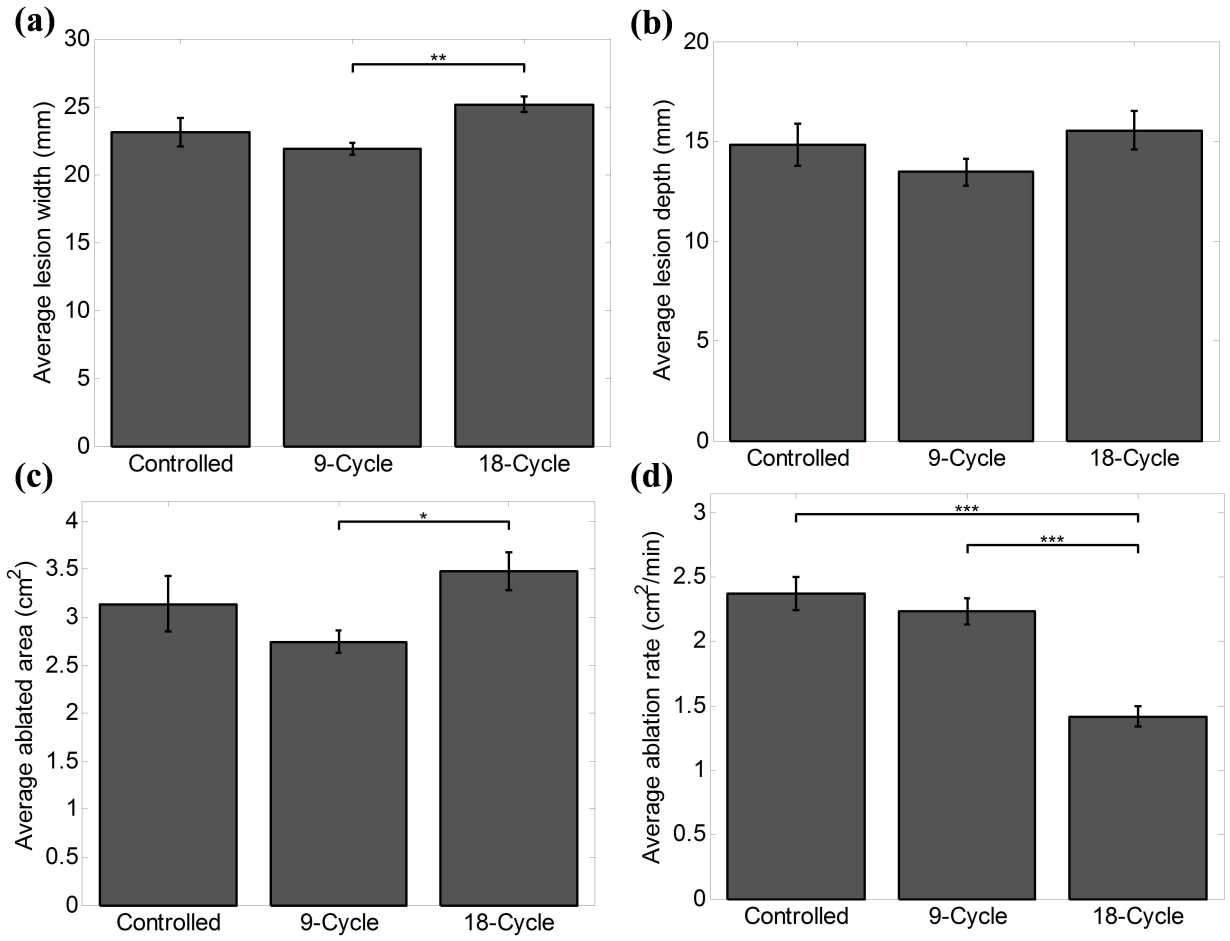

Figure 3.6: Statistical analysis of ablation results using the minimum-decorrelation feedback approach. Means and standard errors are shown for (a) lesion width, (b) lesion depth, (c) lesion area, and (d) ablation rate. ($** \; p < 10^{-2}$ and $*** \; p < 10^{-3}$)

aperture ($p = 6.3 \cdot 10^{-5}$). The Bartlett test indicated no significant difference among the variances of ablation widths, depths, or rates. Ablation areas were non-normally distributed according to the Shapiro-Wilk test and were significantly different according to the Kruskal-Wallis test ($p = 0.031$), with the 9-cycle group (2.74 ± 0.12 cm^2) significantly smaller than the 18-cycle group (3.48 ± 0.19 cm^2; $p = 0.0137$), but with the successfully controlled group

(3.14 ± 0.28 cm^2) not significantly different from either uncontrolled group, and with no significant differences in variance. Successfully controlled trials were completed in a treatment time statistically equivalent to the 9-cycle group, but significantly smaller the 18-cycle group ($p = 4.1 \cdot 10^{-7}$).

3.3.2 Experiments using average-decorrelation criterion

In the second series of experiments, employing variable-intensity sonication and average-decorrelation as the stopping criterion, successful control (Δ_{avg} exceeding Δ_{th}) was achieved in 10 of the 13 controlled trials (77%), with the threshold reached in an average of 13.9 cycles or 114.0 s (maximum 16 cycles or 131.2 s; minimum 12 cycles or 98.4 s). The ROI was fully ablated in 8 of 10 successfully controlled trials, 3 of 3 unsuccessfully controlled trials, 1 of 10 9-cycle uncontrolled trials, and 8 of 10 18-cycle uncontrolled trials.

Fig. 3.7 and 3.8 show final B-mode image frames, overlaid by final cumulative echo decorrelation and IBS maps, together with corresponding registered and segmented TTC-stained tissue sections for representative trials from the 9-cycle, successfully controlled, and 18-cycle groups. The white line and dashed green lines indicate the segmented tissue boundaries and predicted ablation region boundaries in the hybrid B-mode/echo decorrelation or B-mode/IBS images. In the TTC-stained sections, red and green lines indicate segmented tissue boundaries and ablated regions respectively. Lesion depths for the trials shown in column (a), (b), and (c) approximately match the minimum, average, and maximum values for each group, respectively.

Fig. 3.9(a), (b) shows ROC curves and AUC values for prediction of local ablation using echo decorrelation and IBS imaging. Statistical results for pair-wise AUC comparisons between all groups for echo decorrelation and IBS imaging are shown in Table 3.3. For echo decorrelation prediction (Fig. 3.9(a)), AUC values for the successfully controlled (AUC = 0.871) and 18-cycle (AUC = 0.722) uncontrolled groups were significantly greater

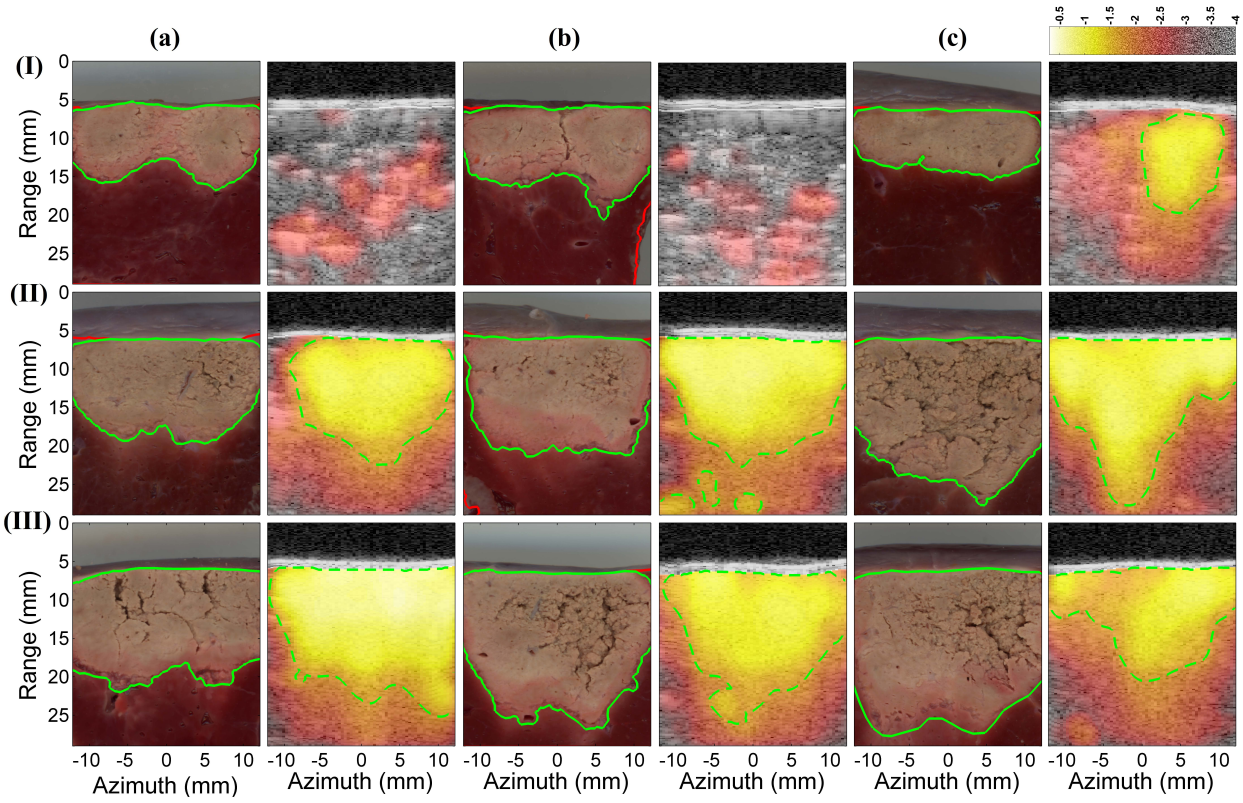

Figure 3.7: Representative histologic and hybrid B-mode/echo decorrelation images for controlled and uncontrolled trials using the average-decorrelation feedback approach. Rows (I)–(III) represent 9-cycle, controlled, and 18-cycle trials with segmentation of tissue boundaries and ablated regions. Red and green lines represent segmented tissue and ablation region boundaries, while white and dashed green lines indicate the segmented tissue and predicted ablation region boundaries ($\log_{10}$-scaled decorrelation per ms: -2.6) in the hybrid B-mode/echo decorrelation images. Columns (a)–(c) represent trials with approximately minimum, average, and maximum measured lesion depth of each group.

than 0.5 ($p < 10^{-16}$). Successfully controlled trials showed significantly better prediction capability than 18-cycle uncontrolled trials ($p < 10^{-8}$). For IBS ablation prediction (Fig. 3.9(b)), AUC values for the successfully controlled (AUC = 0.682) and 18-cycle uncontrolled (AUC = 0.689) groups were significantly greater than chance ($p < 10^{-16}$). The successfully controlled group had slightly smaller AUC than 18-cycle uncontrolled trials ($p = 0.797$). Statistical comparisons between AUC values for echo decorrelation and IBS imaging showed

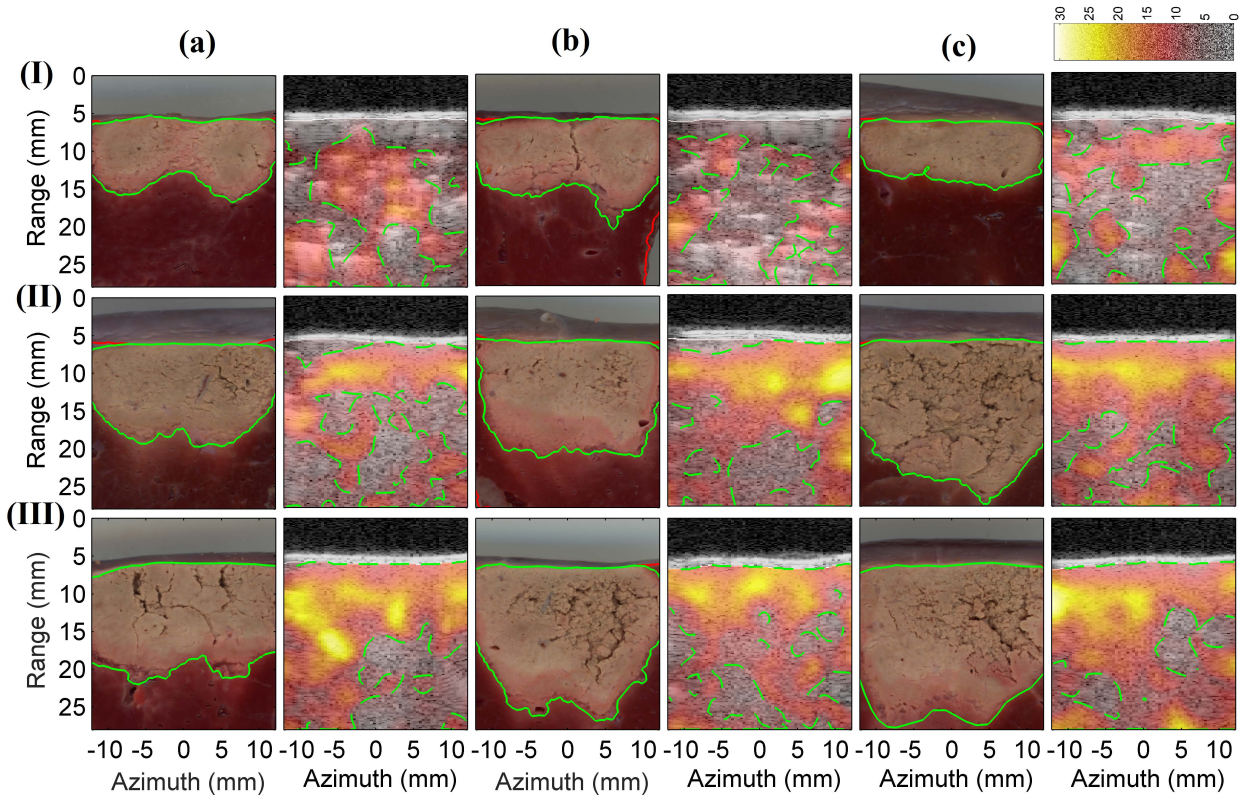

Figure 3.8: Representative histologic and hybrid B-mode/IBS images for controlled and uncontrolled trials using the average-decorrelation feedback approach. Rows (I)–(III) represent 9-cycle, controlled, and 18-cycle trials with segmentation of tissue boundaries and ablated regions. Red and green lines represent segmented tissue and ablation region boundaries, while white and dashed green lines indicate the segmented tissue and predicted ablation region boundaries (IBS threshold 4.0 dB) in the hybrid B-mode/IBS images. Trials shown are the same as Fig. 3.7.

statistically equivalent prediction capability for the 18-cycle uncontrolled group ($p = 0.159$). However, echo decorrelation predicted local tissue ablation significantly ($p = 4.6 \cdot 10^{-10}$) better than IBS in the successfully controlled group.

Optimal thresholds for local ablation prediction and their corresponding sensitivities and specificities for echo decorrelation and IBS imaging are summarized in Table 3.4. For the controlled and 18-cycle groups, echo decorrelation imaging had higher sensitivity and

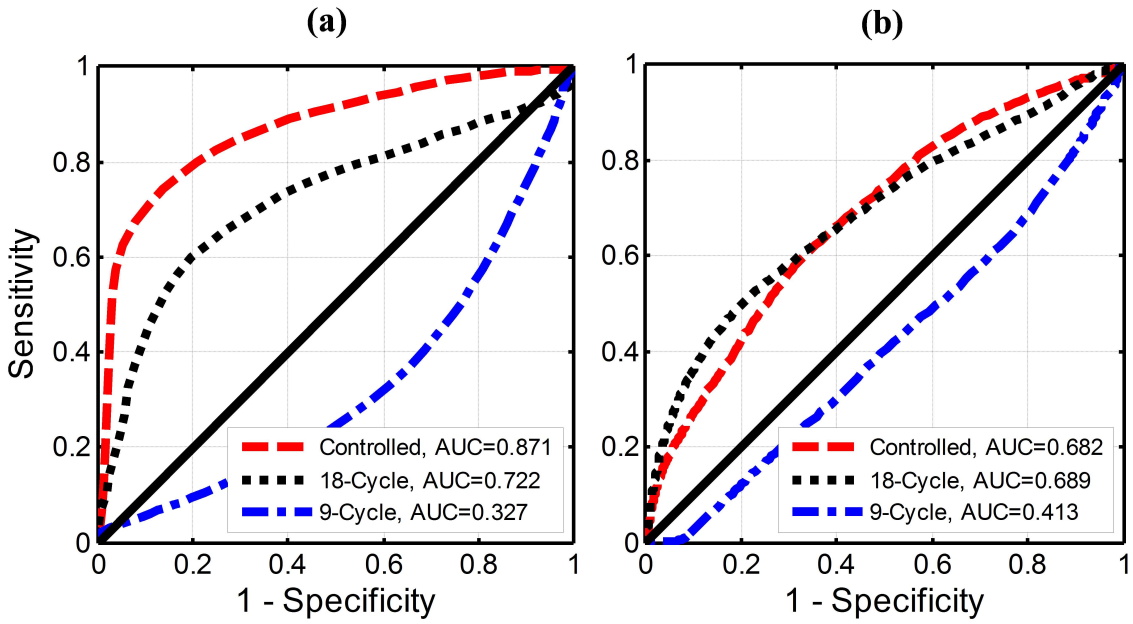

Figure 3.9: ROC curves for (a) echo decorrelation and (b) IBS ablation prediction for successfully controlled, 9-cycle uncontrolled, and 18-cycle uncontrolled groups (AUC: area under ROC curve) using the average-decorrelation feedback approach.

Table 3.3: Results of two-tailed z tests comparing AUC values for echo decorrelation prediction of local ablation among all bulk US groups using the average-decorrelation criterion.

Echo decorrelation imaging		
	Controlled	9-cycle
9-cycle	24.7 ($< 10^{-16}$)	
18-cycle	7.09 ($1.4 \cdot 10^{-12}$)	-15.5 ($< 10^{-16}$)
IBS imaging		
9-cycle	10.0 ($< 10^{-16}$)	
18-cycle	-0.26 (0.797)	-10.2 ($< 10^{-16}$)

specificity for local ablation prediction compared to IBS. For the 9-cycle uncontrolled groups, both echo decorrelation and IBS showed anomalous prediction behavior for tissue ablation.

Table 3.4: Optimal thresholds for local ablation prediction and corresponding sensitivities and specificities for the corrected echo decorrelation ($\log_{10}$-scaled per ms) and IBS (decibel-scaled) imaging for all bulk US groups using average-decorrelation criterion.

Echo decorrelation imaging			
Groups	Controlled	9-cycle	18-cycle
Optimum threshold	−2.3	−4.1	−2.7
Sensitivity (%)	77.3	21.0	65.3
Specificity (%)	82.8	56.4	73.5
IBS imaging			
Groups	Controlled	9-cycle	18-cycle
Optimum threshold	6.4	3.6	6.5
Sensitivity (%)	61.5	43.2	59.4
Specificity (%)	65.2	95.1	68.8

Fig. 3.10(a)–(d) shows statistics of lesion dimensions and ablation rates for successfully controlled trials and uncontrolled trials employing the average-decorrelation, variable-intensity approach. Means ± standard errors for the segmented lesion width were 26.4 ± 0.7 mm for the successfully controlled group, 25.2 ± 0.5 mm for the 9-cycle group, and 26.9 ± 0.6 mm for the 18-cycle group, as shown in Fig. 3.10(a). For the lesion depth, means ± standard errors were 14.7 ± 0.9 mm for successfully controlled trials, 8.3 ± 0.7 mm for the 9-cycle group, and 16.0 ± 1.2 mm for the 18-cycle group, as shown in Fig. 3.10(b). For the lesion area, mean ± standard error values were 3.65 ± 0.2 cm^2 for successfully controlled trials, 2.14 ± 0.1 cm^2 for the 9-cycle group, and 4.06 ± 0.3 cm^2 for the 18-cycle group, as shown in Fig. 3.10(c). For ablation rate, mean ± standard error values were 1.93 ± 0.1 cm^2/min for successfully controlled trials, 1.73 ± 0.1 cm^2/min for the 9-cycle group, and 1.65 ± 0.1 cm^2/min for the 18-cycle group, as shown in Fig. 3.10(d). For treatment time, mean ± standard error was 114.0 ± 4.1 s for successfully controlled trials, compared to fixed values of 73.8 s for

the 9-cycle group, and 147.6 s for the 18-cycle group. As in the minimum feedback control approach, means ± standard error values for unsuccessfully controlled trials ($N = 3$) were close to the 18-cycle uncontrolled trials for lesion width (26.1 ± 0.29 mm), lesion depth (17.0 ± 0.7 mm), ablated area (4.32 ± 0.25 cm^2), and ablation rate (1.75 ± 0.08 cm^2/min)

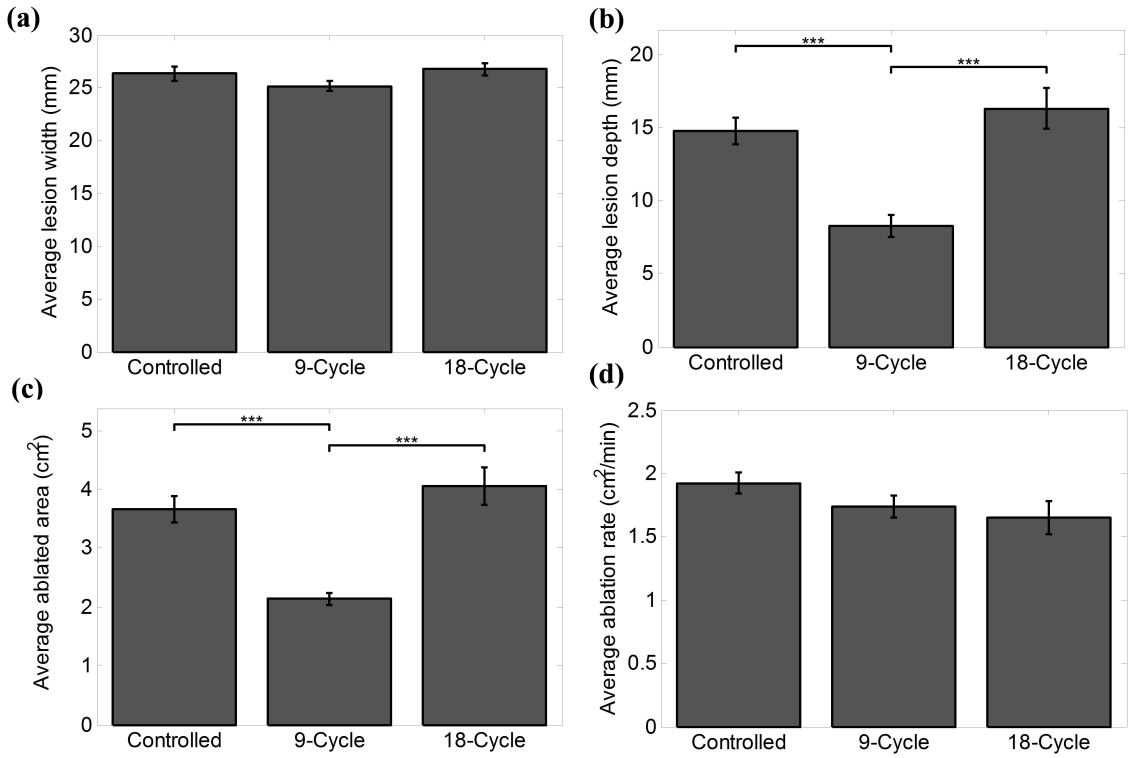

Figure 3.10: Statistical analysis of results from ablation trials using the average-decorrelation feedback approach. Means and standard errors are shown for (a) lesion width, (b) lesion depth, (c) lesion area, and (d) ablation rate. (*** $p < 10^{-3}$)

Shapiro-Wilk test results indicated all ablation lesion dimensions and rates were normally distributed ($p > 0.05$). ANOVA tests showed significant differences between depths ($p = 1.9 \cdot 10^{-5}$) and areas ($p = 8.2 \cdot 10^{-6}$), but no significant differences between ablation rates or lesion widths. Successfully controlled trials and 18-cycle uncontrolled trials had statistically equivalent lesion depths and areas, both significantly larger than the 9-cycle uncontrolled

group ($p < 10^{-3}$). The Bartlett test indicated no significant difference among the variances of ablated lesion depths, widths, or rates for all groups. However, the lesion area of the 9-cycle group (2.13 ± 0.10 cm^2) had smaller mean ($p < 10^{-3}$) and variance ($p < 0.04$) compared to the successfully controlled (3.66 ± 0.22 cm^2) and 18-cycle (4.06 ± 0.32 cm^2) groups. Average lesion widths for the successfully controlled and 18-cycle uncontrolled group were significantly larger than the transducer aperture ($p = 0.016$, $p = 3.1 \cdot 10^{-3}$, respectively). Mean $\pm$ standard error for the duration of successfully controlled treatments was 114.0 ± 4.1 s for successfully controlled trials, significantly larger than the fixed 73.8 s duration of 9-cycle uncontrolled treatments ($p = 4.6 \cdot 10^{-6}$) but significantly smaller than the fixed duration of 147.6 s for 18-cycle uncontrolled treatments ($p = 2.0 \cdot 10^{-5}$). As in the minimum feedback control approach, means $\pm$ standard error values for unsuccessfully controlled trials ($N = 3$) were close to the 18-cycle uncontrolled trials for lesion width (26.1 ± 0.29 mm), depth (17.0 ± 0.7 mm), area (4.32 ± 0.25 cm^2), and rate (1.75 ± 0.08 cm^2/min).

Fig. 3.11 shows statistics of final Δ_{avg} values within the control ROI for the group with audible popping sounds ($N = 17$) and with no audible sound ($N = 16$). Based on the Shapiro-Wilk test, values of Δ_{avg} were non-normally distributed ($p < 0.05$). The median of Δ_{avg} for the audible-sound group was significantly greater than the no-sound group ($p = 8.4 \cdot 10^{-6}$). Maximum values of the ensemble-averaged decorrelation $\overline{\Delta}(y, z, m)$ for cycles with observed popping sounds ranged from -1.91 to -0.82, with mean $\pm$ standard deviation -1.23 ± 0.31 ($\log_{10}$-scaled decorrelation per ms). The audible popping sound synchronized with the treatment end point for 60% of successfully controlled trials using the average-decorrelation criterion.

Fig. 3.12 shows statistics of final cumulative IBS values within the control ROI for the group with audible popping sounds ($N = 17$) and with no audible sound ($N = 16$). Based on the Shapiro-Wilk test, values of ensemble-averaged IBS were non-normally distributed

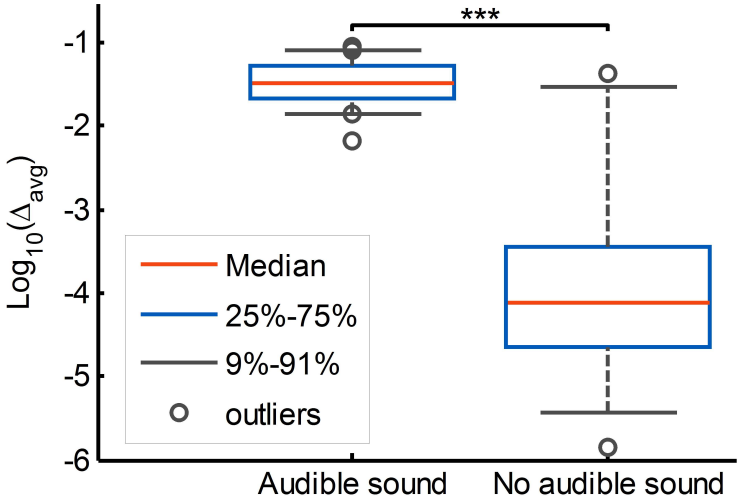

Figure 3.11: Box plot of average echo decorrelation value inside the control ROI for trials with observed audible sound ($N = 17$) and with no audible sound ($N = 16$). ($*** p < 10^{-3}$)

($p < 0.05$). The median of ensemble-averaged IBS for the audible-sound group was significantly greater than the no-sound group ($p = 2.6 \cdot 10^{-6}$). Maximum values of the ensemble-averaged IBS for cycles with observed popping sounds ranged from 16.0 to 27.9 dB, with mean $\pm$ standard deviation 22.9 ± 3.6 dB.

3.3.3 Comparison of Control Approaches

Ablation outcomes differed somewhat between the two control approaches, as illustrated in Figs. (3.13–3.15). Successfully controlled trials employing the average-decorrelation criterion and variable-intensity sonication (Section 3.3.2) showed significantly greater lesion width ($p = 0.020$, Fig. 3.13(a)), statistically equivalent lesion depth ($p = 0.97$, Fig. 3.13(b)), significantly greater treatment time ($p = 1.63 \cdot 10^{-4}$, Fig. 3.13(c)), and significantly smaller ablation rate ($p = 0.011$, Fig. 3.13(d)) compared to successfully controlled trials employing the minimum-decorrelation criterion with constant-intensity sonication (Section 3.3.1).

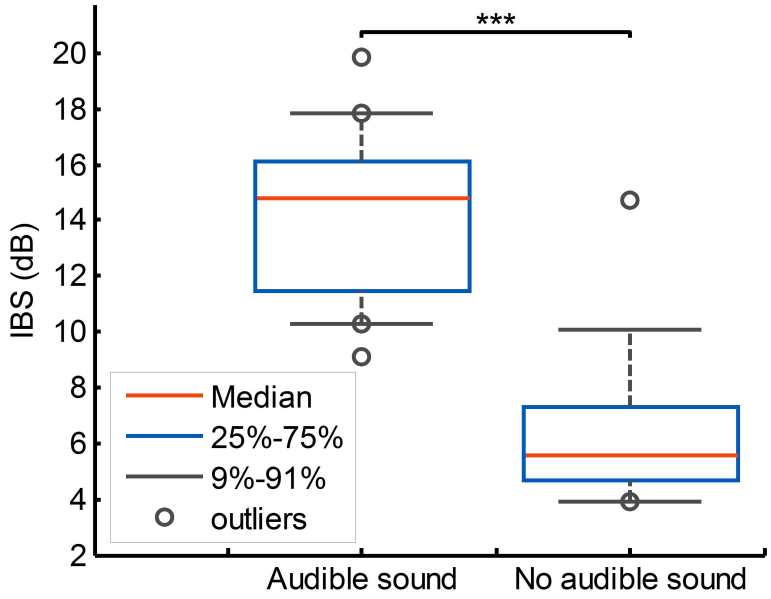

Figure 3.12: Box plot of average IBS value inside the control ROI for trials with observed audible sound ($N = 17$) and with no audible sound ($N = 16$). ($*** \; p < 10^{-3}$)

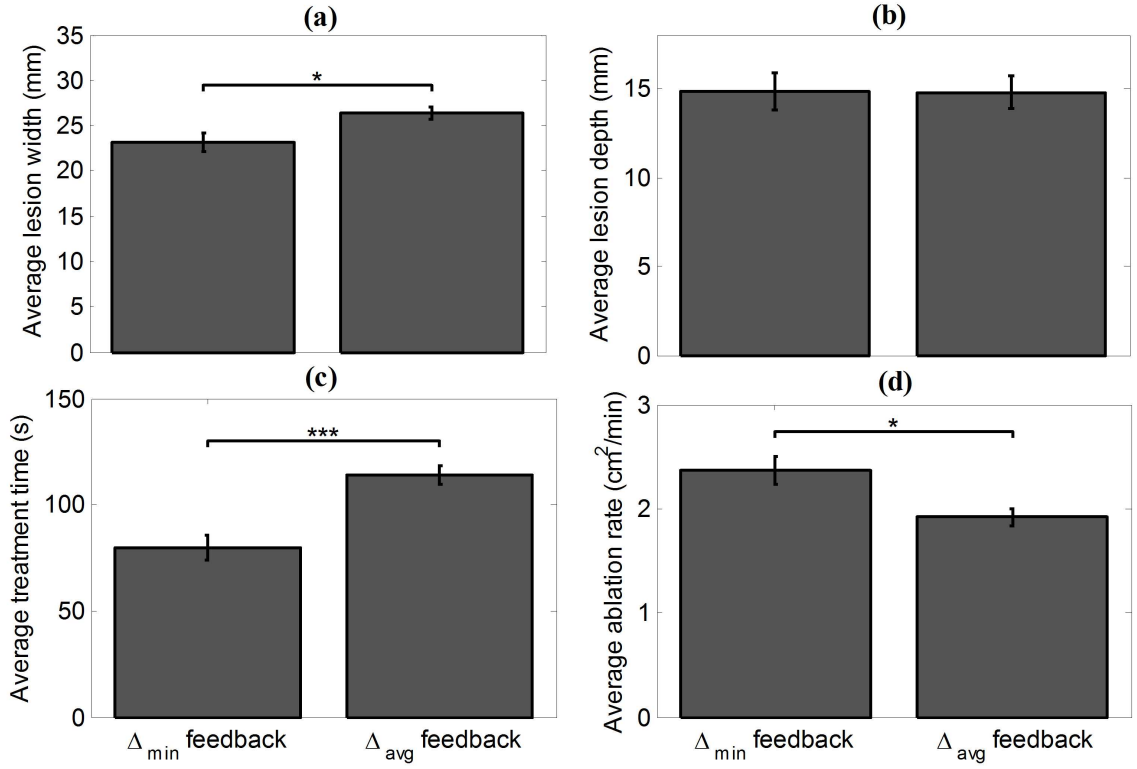

Figure 3.13: Statistical comparison of ablation results for successfully controlled trials using the minimum-decorrelation and average-decorrelation feedback criteria. Means and standard errors are shown for (a) lesion width, (b) lesion depth, (c) treatment time, and (d) ablation rate. ($* \; p < 0.05$ and $*** \; p < 10^{-3}$)

For prediction of ablated area by echo decorrelation, the cutoff for minimum RMS error (1.42 cm^2) between predicted and measured areas over all trials ($N = 70$) was found to be -2.6 ($\log_{10}$-scaled decorrelation per ms). Fig. 3.14 shows scatter plots of ablated areas predicted by this optimum echo decorrelation cutoff for all treatment groups using both the minimum-decorrelation and average-decorrelation approaches. In the series of experiments employing the minimum-decorrelation criterion with constant-intensity sonication, absolute and normalized RMS errors for predicted areas were 0.94 cm^2 (30.3%) for successfully controlled trials, 1.69 cm^2 (62.0%) for 9-cycle uncontrolled trials, and 0.78 cm^2 (23.6%) for 18-cycle uncontrolled trials. In the series of experiments employing the average-decorrelation criterion with variable-intensity sonication, corresponding absolute and normalized RMS errors were 0.74 cm^2 (21.6%) for successfully controlled trials, 1.87 cm^2 (90.0%) for 9-cycle uncontrolled trials and 1.99 cm^2 (52.6%) for 18-cycle uncontrolled trials.

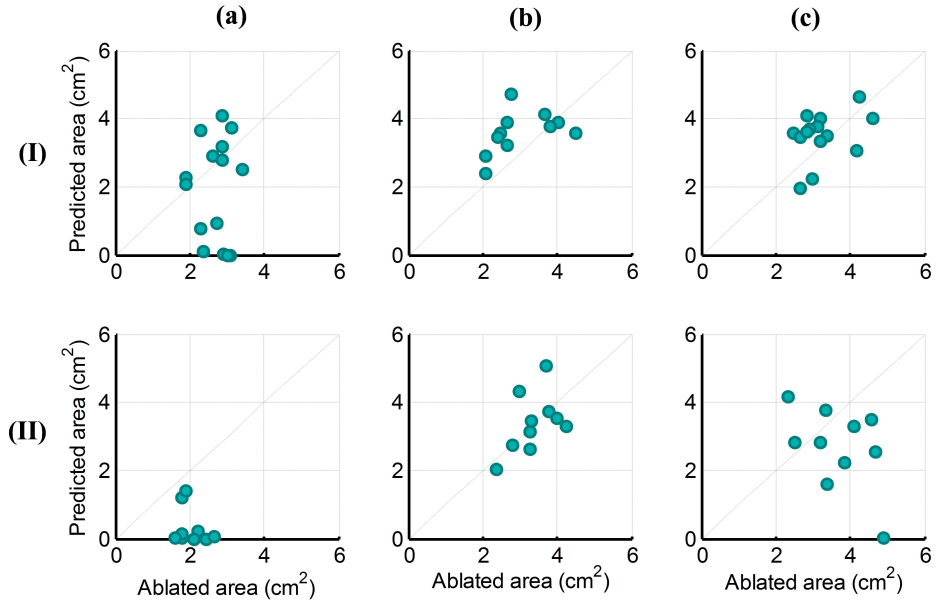

Figure 3.14: Comparison of echo decorrelation predicted vs. measured ablation areas. Scatter plots are shown for (a) 9-cycle, (b) successfully controlled, and (c) 18-cycle groups using (I) minimum-decorrelation and (II) average-decorrelation control approaches.

For prediction of ablated area by IBS, the cutoff for minimum RMS error (0.81 cm^2) between predicted and measured areas over all trials ($N = 70$) was found to be 4.0 dB. Fig. 3.15 shows scatter plots of ablated areas predicted by this optimum IBS cutoff for all treatment groups using both the minimum-decorrelation and average-decorrelation approaches. In the series of experiments employing the minimum-decorrelation criterion with constant-intensity sonication, absolute and normalized RMS errors for predicted areas were 0.99 cm^2 (31.7%) for successfully controlled trials, 0.81 cm^2 (29.7%) for 9-cycle uncontrolled trials, and 0.64 cm^2 (19.5%) for 18-cycle uncontrolled trials. In the series of experiments employing the average-decorrelation criterion with variable-intensity sonication, corresponding absolute and normalized RMS errors were 0.72 cm^2 (21.1%) for successfully controlled trials, 0.79 cm^2 (37.9%) for 9-cycle uncontrolled trials and 0.90 cm^2 (23.6%) for 18-cycle uncontrolled trials.

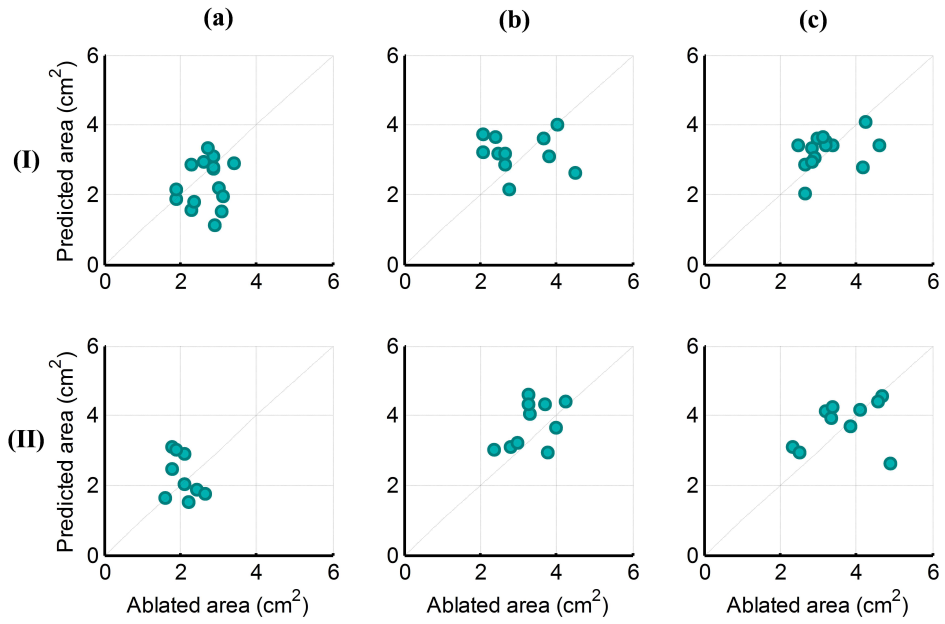

Figure 3.15: Comparison of IBS predicted vs. measured ablation areas using IBS imaging. Scatter plots are shown for (a) 9-cycle, (b) successfully controlled, and (c) 18-cycle groups using (I) minimum-decorrelation and (II) average-decorrelation control approaches.

Post hoc analysis results for both series of controlled ablation experiments are shown in Fig. 3.16. For all trials controlled using the minimum-decorrelation criterion ($N = 15$), Fig. 3.16(a) shows final Δ_{min} values from each experiment together with final Δ_{avg} values from *post hoc* analysis using the average-decorrelation feedback parameter and the corresponding 12 mm $\times$ 9 mm control ROI. In the *post hoc* analysis, the average-decorrelation threshold of -1.576 was crossed in 11 of these 15 trials with average threshold-crossing time 81.3 ± 6.7 s. Notably, the average threshold-crossing time for trials from the minimum-controlled group, subjected *post hoc* to the average-decorrelation criterion, was statistically equivalent to the treatment time for trials successfully controlled using the average-decorrelation criterion.

For all trials controlled using the average-decorrelation criterion ($N = 13$), Fig. 3.16(b) shows final Δ_{avg} values from each experiment together with final Δ_{min} values from *post hoc* analysis using the minimum-decorrelation criterion and its corresponding 16 mm $\times$ 12 mm control ROI. In the *post hoc* analysis, the minimum-decorrelation threshold of -3.20 was crossed in 8 of these 13 trials with average threshold-crossing time 111.7 ± 4.6 s. Similar to the minimum-decorrelation controlled trials, the average threshold-crossing time for trials from the average-decorrelation controlled group, subjected *post hoc* to the minimum-decorrelation criterion, was statistically equivalent to the treatment time for trials successfully controlled using the minimum-decorrelation criterion.

Both control approaches showed similar success in ablation of equivalent control ROIs. Successfully controlled trials using the minimum-decorrelation criterion achieved complete ablation of the 12 mm $\times$ 9 mm average-decorrelation control ROI in 7 of 11 cases, compared to 8 of 10 cases for trials successfully controlled using the average-decorrelation approach. Similarly, successfully controlled trials using the average-decorrelation criterion achieved complete ablation of the 16 mm $\times$ 12 mm minimum-decorrelation control ROI in 3 of 10 cases, compared to 3 of 11 cases for trials successfully controlled using the minimum-decorrelation approach.

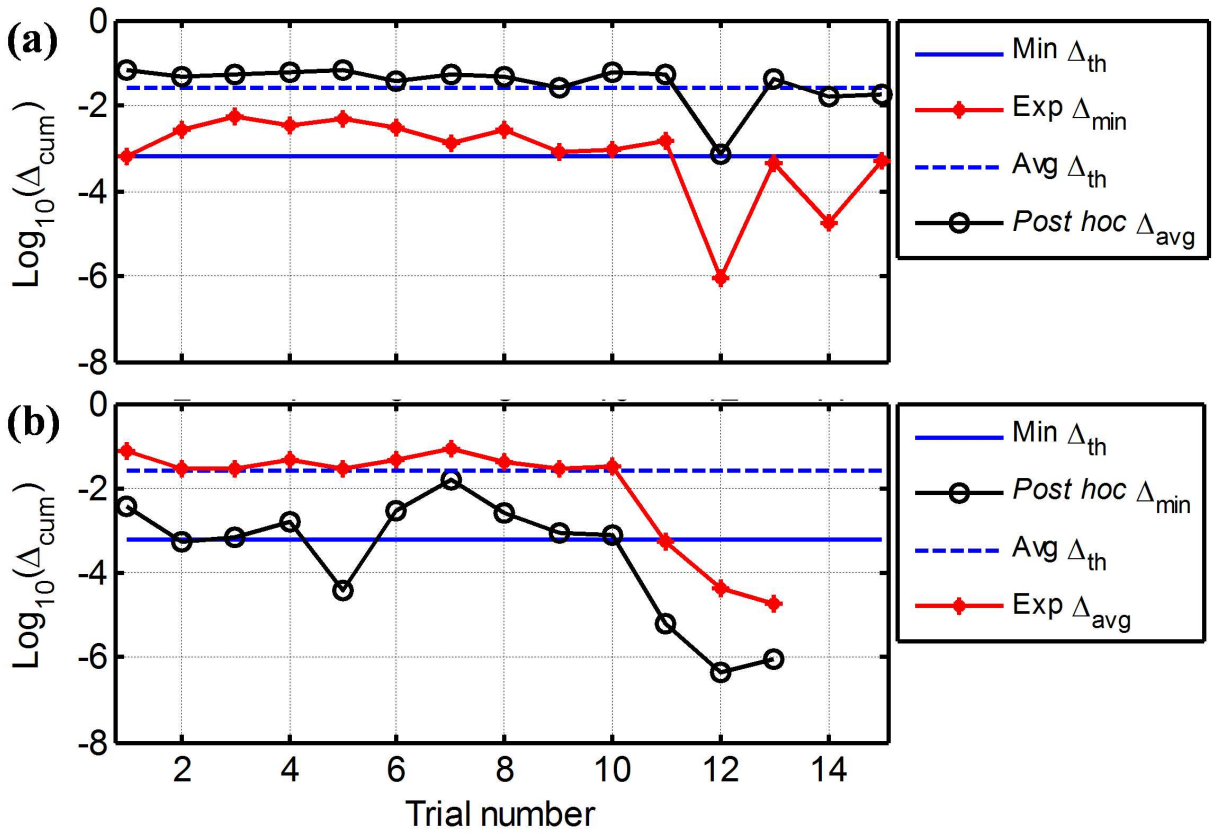

Figure 3.16: Experimental and *post hoc* results for trials controlled by (a) minimum-decorrelation and (b) average-decorrelation criteria. Red, black and blue lines represent the experimental, *post hoc*, and threshold echo decorrelation values inside the region of interest, respectively.

3.4 Discussion

In this chapter, the concept of controlling bulk thermal ablation using US echo decorrelation imaging feedback was demonstrated in *ex vivo* bovine liver using two feedback approaches. Successful control, defined as meeting the prespecified echo decorrelation feedback threshold, was achieved in $> 70\%$ of trials for either approach. Successfully controlled trials using either feedback approach resulted in higher ablation rates and better capability to predict local ablation, as judged by area under the ROC curve, than matching 9-cycle or

18-cycle uncontrolled groups. However, successfully controlled trials using either feedback approach did not provide improved consistency for the ablated tissue area; for either approach, ablated area variance for the controlled group was not significantly smaller than for either matching uncontrolled group. In either group, results of controlled ablation trials were similar to those for the matching 18-cycle group, both in terms of thermal lesion dimensions and capability to predict ablation; however, controlled ablation trials required significantly less treatment time, which could be considered an advantage of this control approach.

The proposed optimization method resulted in different ROI sizes and decorrelation thresholds for the two echo decorrelation feedback predictors. The optimum ROI selected for the minimum-decorrelation criterion was larger than that for the ROI-average criterion experiments (16 mm $\times$ 12 mm vs. 12 mm $\times$ 9 mm), while the corresponding decorrelation threshold was smaller (-3.20 vs. -1.576 $\log_{10}$-decorrelation per ms). Nonetheless, retrospective comparison of the two control approaches showed that their control performance was very similar. For either series of controlled ablation experiments, the average treatment time for successfully controlled ablation nearly matched the threshold-crossing time for the other series when subjected *post hoc* to the same feedback approach used experimentally. Similarly, when assessing complete ablation of the same ROI, successful control by either approach resulted in nearly equal success rates. These results imply that the proposed optimization successfully set appropriate control criteria for both feedback approaches, such that meeting either stopping criterion had a nearly equivalent effect on ablation outcomes. In general, control thresholds optimized using this approach will increase with smaller control ROI sizes, and will be larger when based on the average echo decorrelation, compared to the minimum echo decorrelation.

Successfully controlled trials for both feedback approaches showed better echo decorrelation prediction capability for local ablation than 9-cycle or 18-cycle uncontrolled trials of the same ablation sequence reported here, as well as the uncontrolled *in vivo* bulk US ablation

experiments ($N = 10$, AUC = 0.620 in liver, AUC = 0.675 in VX2 tumor) reported by Fosnight et al. [33] using a constant-intensity sonication scheme (7–9 therapy cycles, 60–70.5% duty cycle, 50–63 W/cm^2 I_{SPTP}, 5.0–5.4 MHz frequency). Echo decorrelation imaging predicted local tissue ablation significantly better than IBS imaging in successfully controlled trials using both feedback approaches. For both echo decorrelation and IBS imaging, successfully controlled trials using the average-decorrelation criterion showed ability to predict local ablation (AUC = 0.871, AUC = 0.682 respectively) statistically equivalent to trials controlled by the minimum-decorrelation criterion (AUC = 0.862, AUC = 0.725 respectively), consistent with the observation that either approach provided equivalent feedback on ablation progress.

For ablated area prediction using echo decorrelation or IBS, better prediction capability was observed for successfully controlled trials using the average-decorrelation criterion, compared to the 9-cycle and 18-cycle uncontrolled groups. However, better area prediction capability was observed for the 18-cycle uncontrolled group using the minimum-decorrelation criterion, compared to the controlled and 9-cycle uncontrolled groups. RMS error of predicted ablated area for IBS was smaller than for echo decorrelation in all groups using both feedback approaches (minimum RMSE: 0.81 cm^2 vs. 1.42 cm^2), even though local ablation prediction capability was better for the echo decorrelation than for IBS. This discrepancy may have occurred because the threshold (4.0 dB) for minimum RMS error in area prediction using IBS imaging was low, which reduced the specificity of local ablation prediction, while also reducing area prediction error by predicting ablation at positions of hyperechoic artifacts at depths > 20 mm, as shown in Fig. 3.4 and 3.8.

Echo decorrelation and IBS imaging showed anomalous prediction performance for the 9-cycle uncontrolled group (AUC = 0.327 and AUC = 0.413, respectively) using the average-decorrelation criterion with variable-intensity sonication. AUC values less than 0.5 correspond to negative prediction outcomes, i.e., for these experiments, higher echo decorrelation

and IBS tended to predict the absence of thermal ablation. The probable reason for these anomalous results is that 9 cycles of sonication at 38.3 W/cm^2 induced heating insufficient to cause high decorrelation or hyperechoic activity (high tissue reflectivity) at the ablation site. Previous analyses have shown that high decorrelation occurs most consistently for temperatures exceeding 80 °C [92]. In addition, prediction performance for this group was adversely affected by false-positive predictions due to substantial echo decorrelation and tissue brightness outside the heated region (Fig. 3.7 (I-a,b) and Fig. 3.8 (I-a,b)), believed to be associated with air-filled cavities in the *ex vivo* tissue [118].

Comparing ablation outcomes of the two control approaches, successfully controlled trials using the average-decorrelation criterion with variable-intensity sonication showed larger and more consistent coagulation areas but also significantly longer treatment times, compared to successfully controlled trials using the minimum-decorrelation criterion with constant-intensity sonication (Fig. 3.13). Results of the retrospective study comparing *post hoc*-applied feedback criteria indicate that the different feedback approaches did not cause these differences in ablation outcomes. Therefore, the likely reason is the different sonication scheme used for each control approach. The larger observed ablation area for controlled ablation using the variable-intensity sonication scheme was primarily due to a significant increase in lesion width (along the azimuthal direction, parallel to the transducer surface), rather than in lesion depth as originally anticipated for the variable-intensity sonication sequence, possibly because the overall tissue heating rate was lower. Similarly, the shorter treatment time for controlled trials using the constant-intensity sonication scheme is likely due to the faster heating rate early in these trials, leading to earlier occurrence of high echo decorrelation.

Several studies [122, 126, 127] have investigated the relation between complications (e.g., bleeding, dissemination, and tumor metastasis) arising from RFA treatment and the occurrence of audible popping sounds due to tissue vaporization, believed to cause significant

mechanical damage to tissue. Methods employed to delay this vaporization have included monitoring tissue impedance [122], applying lower RF power (i.e., maximum 70 W) [127] and injecting Sonazoid® microbubbles [126]. In the experiments reported here, audible popping sounds always coincided with large echo decorrelation (maximum ensemble-averaged decorrelation $> 10^{-2}$ per ms) or IBS (maximum ensemble-averaged IBS > 15 dB) values at the same cycle. These results suggest that control by echo decorrelation or IBS, e.g. using lower thresholds, could be useful to reduce or prevent tissue vaporization and the concomitant undesirable mechanical tissue damage. The same control approach may also help avoid RFA-induced vapor bubbles that obscure B-mode image quality during tumor ablation [89, 128].

Compensation for motion and noise artifacts is also important for successful clinical translation of the control approach investigated here. Recently in offline processing, echo decorrelation artifacts due to tissue motion and electronic noise were successfully compensated by the method described in Hooi et al. [70] for *in vivo* bulk US thermal ablation [33] and have also been compensated using motion gating for *in vivo* RFA [88]. For better control performance during future *in vivo* ablation experiments, motion and noise correction to echo decorrelation imaging [70] could be implemented in real time. This approach is employed in Chapter 4, where the cumulative ensemble-averaged echo decorrelation map from initial sham sonication cycles is utilized to compensate echo decorrelation maps during therapy [33]. For *in vivo* bulk US ablation, higher acoustic intensities will be needed to overcome the heat-sink effect due to blood perfusion. Further improved performance in the presence of tissue motion may be achievable by combining echo decorrelation imaging with real-time image fusion approaches employing automatic tracking of ultrasound probe position [85].

3.5 Conclusion

Two optimized echo decorrelation imaging feedback approaches were investigated for control of bulk US thermal ablation in *ex vivo* bovine liver. Feedback using either the minimum-decorrelation or average-decorrelation criteria, with constant- or variable-intensity sonication respectively, resulted in greater ablation rate compared to matching uncontrolled trials. Either feedback criterion, when employing control thresholds and ROIs optimized by the same approach, provided equivalent information on ablation progress. Successfully controlled ablation trials using either approach also provided better prediction of local ablation than uncontrolled trials. These results indicate that echo decorrelation imaging feedback, using either minimum-decorrelation or average-decorrelation criteria, is feasible for control of bulk thermal ablation.

Chapter 4
In vivo ultrasound thermal ablation controlled using echo decorrelation imaging

4.1 Objectives

In Chapters 2 and 3, echo decorrelation imaging was successfully validated for controlling *ex vivo* ultrasound (US) thermal ablation in bovine liver [118, 119]. Results from the previous *ex vivo* studies indicated that preclinical translation of the proposed real-time control method is feasible with some considerations. These considerations include necessary modifications to the stopping criteria previously employed in the controlled *ex vivo* US experiments, to be consistent with *in vivo* tissue acoustical and anatomical characteristics. Also, compensating the effect of artifactual echo decorrelation due to motion and noise is an essential consideration for controlling thermal ablation *in vivo*.

The ability of echo decorrelation imaging to monitor *in vivo* US treatments in rabbit liver and VX2 tumor was successfully demonstrated by Fosnight et al. [33], without real-time control. In spite of the low sensitivity of echo decorrelation imaging to motion artifacts, liver motion during treatment was thought to cause overprediction in some trials [33]. A motion and noise correction method [70] was used to correct cumulative echo decorrelation maps computed from stored echo data. Here, the same correction method was implemented

to work simultaneously with the real-time control algorithm to provide corrected cumulative echo decorrelation maps in real time.

In this chapter, the feasibility of controlling *in vivo* US thermal ablation, including HIFU and unfocused (bulk) US, using motion-corrected echo decorrelation imaging feedback in rabbit liver and VX2 tumor was investigated. Ablation outcomes and the prediction capability of echo decorrelation imaging for the controlled trials were compared with the uncontrolled *in vivo* US experiments reported by Fosnight et al. [33].

4.2 Materials and methods

In this section, the experimental setup and procedures for controlled *in vivo* US thermal ablation in rabbit liver and VX2 tumor are explained in detail. Methods described previously in Chapter 2 for treatment imaging and control (Section 2.2.2.b), image processing (Section 2.2.2.c), image segmentation and registration (Section 2.2.2.d), and ablation prediction assessment (Section 2.2.2.e) were utilized here with minor modifications.

4.2.1 Motion-corrected feedback control algorithm

The real-time feedback control algorithm employed here was previously validated in *ex vivo* bovine liver experiments to control HIFU [118] (Chapter 2) and bulk US [119] (Chapter 3) ablation treatments. For better prediction and control performance, the motion and noise compensation method previously described by Hooi et al. [70] was integrated with the control algorithm, such that the effect of motion-induced decorrelation was corrected in real time. Corrected cumulative ensemble-averaged echo decorrelation maps (Δ_{corr}) [33] for each therapy cycle were computed as

$$\Delta(y,z,m)_{\text{corr}} = \frac{\Delta(y,z,m)_{\text{cum}} - \Delta_{\text{sham}}}{1 - \Delta_{\text{sham}}} \tag{4.1}$$

where y and z are azimuth and range image coordinates, m is the therapy cycle index, and Δ_{sham} is the cumulative ensemble-averaged echo decorrelation map computed for sham cycles (i.e., treatments with zero acoustic power). In the corrected decorrelation map, points where $\Delta(y, z, m)_{\text{corr}} < 0$ were replaced by the minimum of Δ_{sham}.

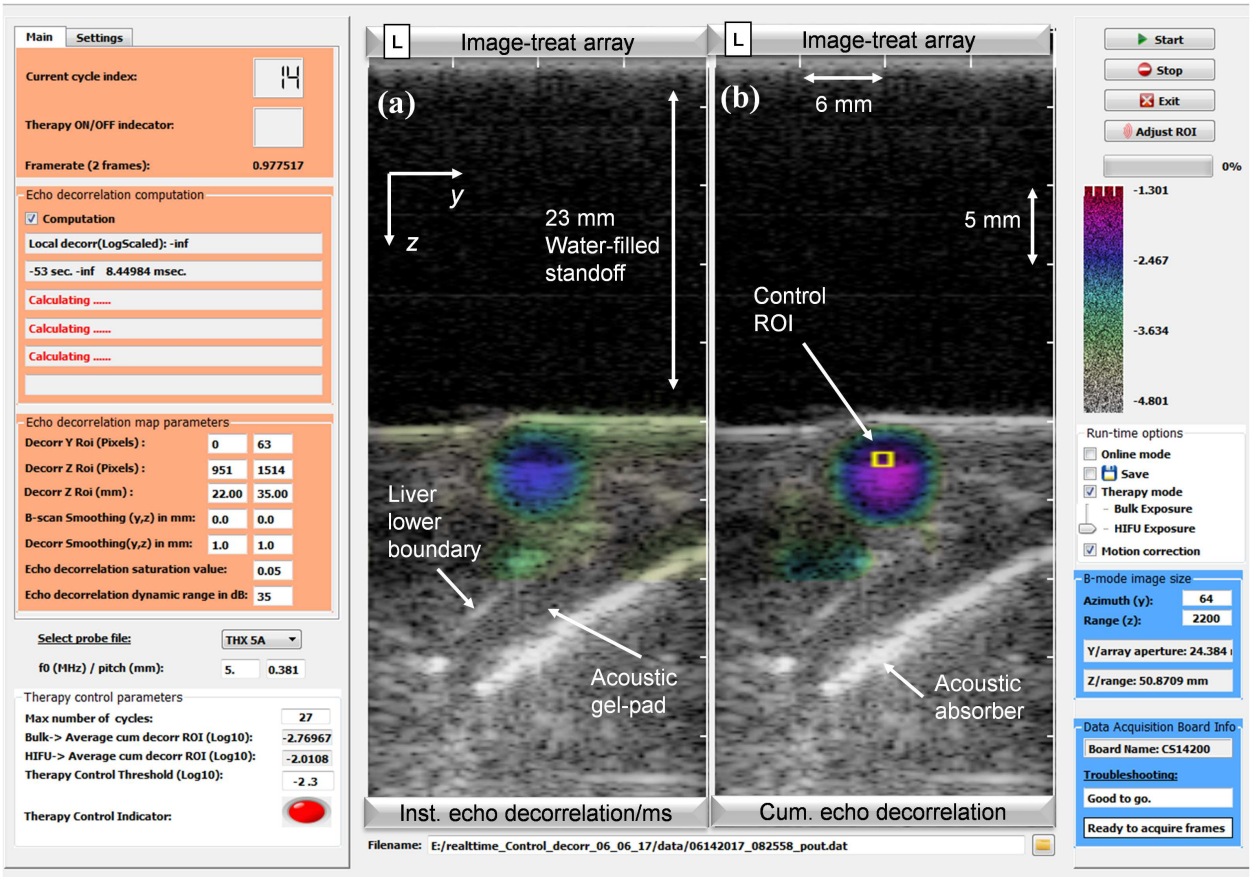

Figure 4.1: GUI of the C++ application used for *in vivo* US thermal ablation imaging and control. (a) Instantaneous hybrid B-mode/echo decorrelation image. (b) Cumulative echo decorrelation map for each therapy cycle, corrected in real time using decorrelation from sham ablation cycles; the control region of interest is bounded by a yellow line.

The average of $\Delta(y, z, m)_{\text{corr}}$ inside the control ROI (Δ_{avg}) was used as a feedback criterion to control HIFU or bulk US treatments. Therapy cycles were repeated until Δ_{avg} exceeded a

prespecified control threshold (Δ_{th}) or the sonication cycle index m exceeded the maximum number of therapy cycles [118] ($M = 18$).

The graphical user interface (GUI) utilized previously in Chapters 2 and 3 was modified by adding more features for better monitoring and control performance, as shown in Fig. 4.1. The user was able to select the appropriate control ROI shape and size for HIFU or bulk US ablation. Coordinates of both control and decorrelation ROIs were adjusted when needed to be within liver lobe boundaries.

4.2.2 *In vivo* US ablation experiments

Tumor implantation and US ablation experiments were performed according to a protocol approved by the University of Cincinnati Institutional Animal Care and Use Committee. For tumor implantation, New Zealand white rabbits were sedated using ketamine (10 mg/kg) and xylazine (3 mg/kg) and anesthetized using isoflurane. VX2 tumor fragments were implanted in the three liver lobes of each animal ($N = 8$). Each tumor fragment was implanted such that the distance from the inferior liver lobe edge to the tumor was approximately half the azimuthal width of the transducer's standoff (19 mm).

After two weeks tumor growth, US ablation experiments were performed on rabbit liver and VX2 tumor in open surgery. Before each treatment, the animal was sedated and its liver was exposed. Before starting US ablation, the tumor was located on each liver lobe surface by inspection and palpation. A standalone acrylic standoff, identical to the standoff integrated with the US transducer, was used to center the transducer over the tumor surface by marking the standoff corners on the liver capsule with a skin marking pen (Accu-line Products Inc., Hyannis, MA). Thereafter, an acoustic gel pad (Aquaflex, Parker Laboratories Inc., Fairfield, NJ) and acoustic absorber (Precision Acoustics Ltd, Dorset, UK) were cut, thinned, and placed beneath the target zone to minimize acoustic reflection and to constrain the shape of the liver lobe (Fig. 4.2(b)). The array was aligned using a 3D positioning arm

(NOGA Engineering Ltd, Israel) over the marked target zone (Fig. 4.2(a)) and the tumor location was confirmed visually using the B-mode image on the IRIS 2 system screen. At the end of US ablation experiments, the rabbit was sacrificed using Euthasol (200 mg/kg), and its liver was excised and placed in a 0.01M phosphate buffered saline solution.

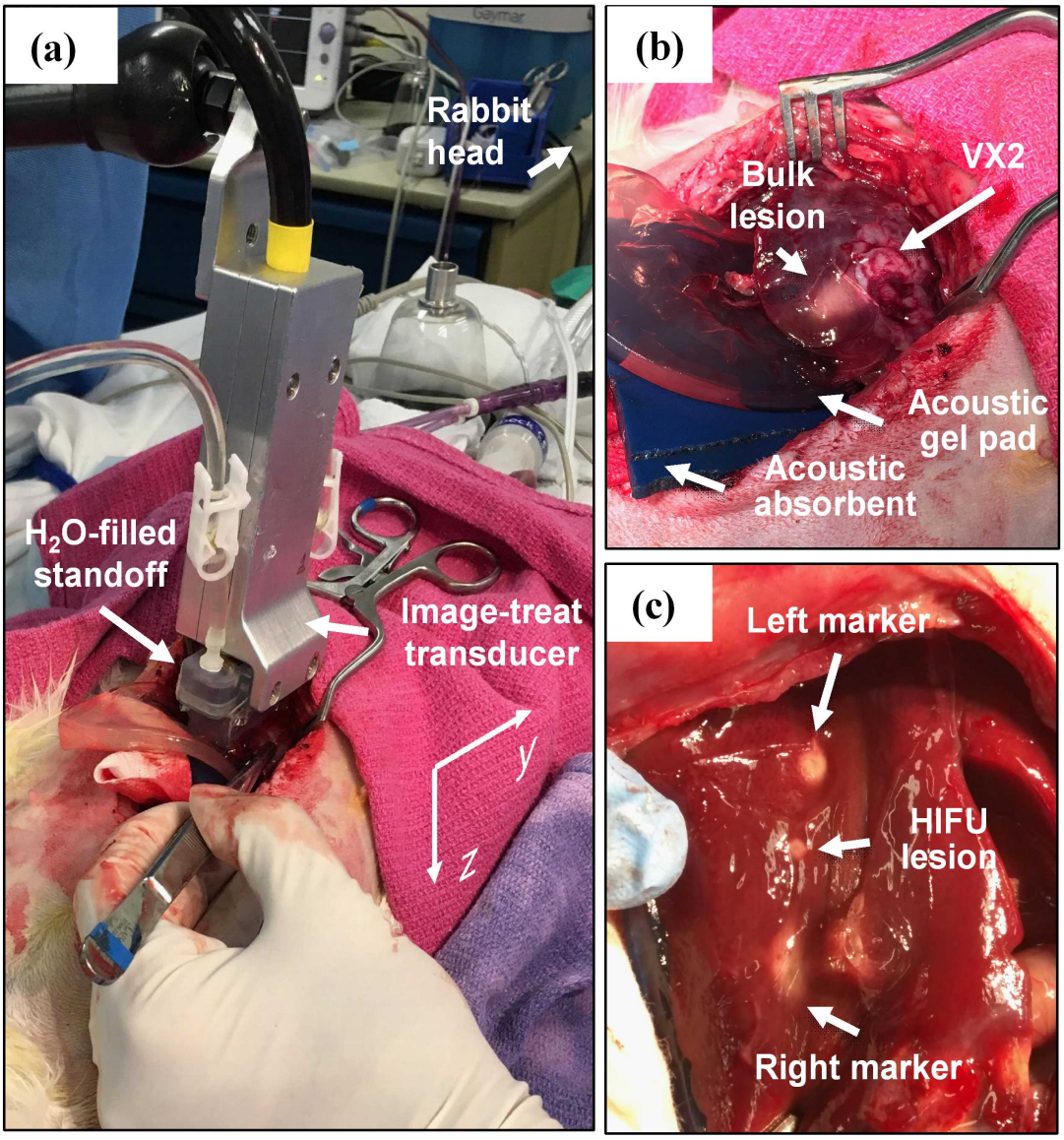

Figure 4.2: Experimental setup. (a) Image-treat array placed on the rabbit liver capsule during open surgery. (b) Bulk thermal ablation of VX2 tumor. (c) HIFU thermal ablation of liver followed by left and right marking exposures.

Ultrasound treatment and imaging were controlled by the Iris 2 US imaging and therapy system (Ardent Sound Mesa, AZ, USA) [102]. Using a dual-mode custom image-treat array transducer (64 element, 4.8×24.4 mm^2 aperture, 5.35–5.50 MHz), pulse-echo US imaging ($> 40\%$ bandwidth, transmit focal depth 3.5 cm, F-number 4) and US ablation (maximum acoustic power 35 W) were performed. The transducer was integrated with a 23 mm standoff which was sealed by a transparent film (Tegaderm, 3M Health Care, St. Paul, MN) and filled with deionized, degassed water.

As with the *ex vivo* experiments described in Chapters 2 and 3, US exposures were performed in cycles with sonication followed by pulse-echo imaging and RF data acquisition. During the imaging period, twenty beamformed RF echo frames were acquired with an 8.62 ms inter-frame time (frame rate 116 Hz). RF frames were sampled and digitized using a data acquisition card (14-bit, 33.3 MHz sampling rate; Compuscope 14200, Gage Applied). Digital RF frames were processed by Hilbert transform to provide in-phase and quadrature (IQ) complex components, demodulated using a 5.0 MHz carrier frequency, and decimated by a factor of 6. Processed IQ frames were used to compute B-mode and echo decorrelation images

Within 3 hours after animal sacrifice, ablated liver and VX2 tumor tissue were sectioned along the image plane and stained with 2% triphenyl tetrazolium chloride (TTC) vital stain. Ablated tissue histology was assessed based on TTC stain uptake. For liver tissue, regions of full TTC uptake (stained red) were interpreted as non-ablated, regions of partial or no TTC uptake (stained pale red) were interpreted as treated, and regions of no TTC uptake (stained brown) were interpreted as ablated [105]. For tumor tissue, regions of full TTC uptake (stained pale red) were interpreted as non-ablated, regions of partial or no TTC uptake (stained faint white) were interpreted as treated, and regions of no TTC uptake (stained white) were interpreted as ablated. TTC-stained sections were optically scanned at 1200 dpi (CanoScan 8800F, Canon, Tokyo, Japan). Of the two facing cross-sections, one

was chosen for segmentation by examining the treated lesion and tumor size. The cross-section with the larger lesion size (or if those were equal, the larger tumor size) was chosen. Scanned histologic images were then manually segmented into non-ablated, treated, and ablated regions [33]. TTC-segmented sections were co-registered using a custom 2D rigid registration MATLAB application as described in Section 2.2.2.d [118].

4.2.3 Controlled HIFU ablation experiments

HIFU treatments were performed using the same timing sequence (0.7 s therapy and 2.2 s imaging per cycle) and control ROI (1×1 mm^2) previously employed in Chapter 2 [118]. The variable intensity sonication sequence previously tested in *ex vivo* bulk US ablation (Chapter 3) was employed. The echo decorrelation threshold Δ_{th} was chosen as the optimal threshold for local ablation prediction in VX2 tumor computed by Fosnight et al. [33] in a similar *in vivo* study. This threshold was -2.3 ($\log_{10}$-scaled decorrelation per ms), which corresponded to 90% specificity and 43% sensitivity in the previous study [33].

For HIFU treatments ($N = 14$), the control ROI was placed 2 mm below the tissue surface. The variable sonication sequence began with 9 sham cycles, followed by 9 sonication cycles (5.35–5.50 MHz, 24% duty) at 1022.0 W/cm^2 I_{SPTP} and up to 9 cycles at 1192.4 W/cm^2, with treatments ending when Δ_{avg} within the control ROI exceeded Δ_{th} or when m exceeded M. The lower and higher intensities employed here were selected as the average and maximum values of the intensities used by Fosnight et al. [33] for uncontrolled *in vivo* HIFU experiments, to increase the likelihood of ablation completion. Controlled trials were compared with *in vivo* uncontrolled HIFU trials ($N = 12$) [33] (6–9 cycles, 5.0–5.4 MHz, 17.5–20.0% duty, 911–1351 W/cm^2 I_{SPTP}).

After each HIFU treatment, two marking lesions were performed at the left and right of each HIFU lesion, as shown in Fig. 4.2(c), to facilitate post-treatment tissue sectioning and for better registration of histologic and US images. Marking lesions were performed

using controlled unfocused exposures fired from the first (1 to 10) or last 10 elements (55 to 64) of the transducer. For the marking exposures, a control ROI, with the same size as the control ROI for HIFU exposures, was positioned 2 mm below the tissue top surface and azimuthally at the center of each 10-element's aperture (10.3 mm left or right from the focal point [33]). Marking exposures were controlled using the same control criteria employed for HIFU ablation. Unfocused sonications employed 6 s pulses (73.1% duty) with 53.8 W/cm^2 I_{SPTP} up to a maximum of 9 therapy cycles, or ended when Δ_{avg} within the control ROI exceeded Δ_{th}. Further details on all controlled *in vivo* HIFU trials can be found in the Appendix.

4.2.4 Controlled bulk US ablation experiments

Bulk US treatments were performed using variable intensity sonication sequences using the same timing scheme (6.0 s therapy and 2.2 s imaging per cycle) previously described in Chapter 3 for *ex vivo* bulk US ablation experiments [119].

Bulk US thermal treatments were controlled using the average-decorrelation criterion (Section 3.2.4) with minor modifications in ROI shape to match the size of rabbit liver lobe's cross-section and the thermal lesion shape. A *post hoc* analysis was performed on archived TTC-segmented tissue sections of rabbit liver and VX2 tumor ($N = 10$) [33] to compute the average and standard deviation of lesion widths, depths, and areas. Results of the *post hoc* analysis were compared with average lesion dimensions of the bulk *ex vivo* trials controlled using the average-decorrelation criterion (Fig. 3.10). Lesion depths (11.2 ± 3.8 mm) and areas (2.4 ± 0.8 cm^2) for rabbit liver were smaller than lesion depths and areas for the bovine liver by approximately 30%. Hence, the control ROI depth used in previous *ex vivo* bulk experiments was reduced by 30% to be 6 mm. For consistency, ROI area was kept the same by increasing the lateral distance between the rectangle edges by 50% on each side. The

resulting control ROI was selected as 18 mm in width × 6 mm in depth, as shown in Fig. 4.3.

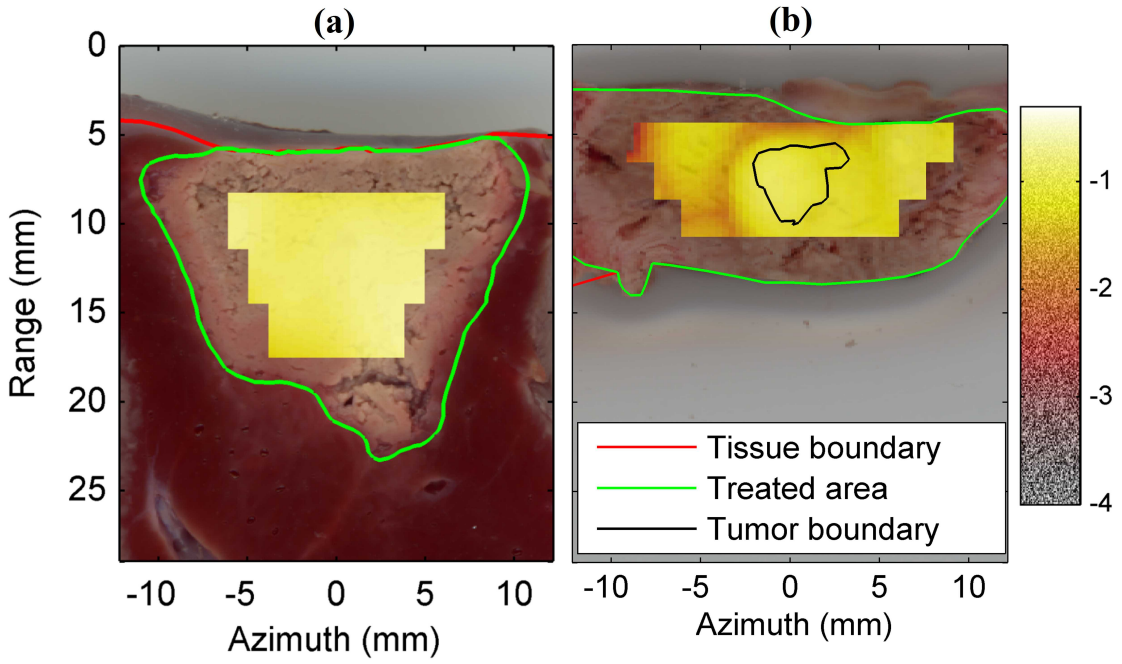

Figure 4.3: Control ROI selection. (a) The control ROI for previous bulk *ex vivo* ablation experiments (12 mm × 9 mm) was modified to match (b) a typical *in vivo* lesion shape, resulting in an ROI width of 18 mm and depth of 6 mm.

For bulk US treatments ($N = 10$), the control ROI was placed 2 mm below the tissue surface. For some thinner liver lobes, the ROI was approximately centered between the top and bottom lobe boundaries. For controlled bulk US treatments, the variable sonication sequence began with 9 sham cycles, followed by 9 sonication cycles (5.35–5.50 MHz, 73.1% duty) at 38.12 W/cm^2 I_{SPTP} and up to 9 cycles at 44.47 W/cm^2, with treatments ending when Δ_{avg} within the ROI exceeded Δ_{th} or when m exceeded M. The lower and higher intensities employed here were selected as the average and maximum values of the intensities used by Fosnight et al. [33] for the uncontrolled *in vivo* bulk US experiments. Controlled

trials were compared with uncontrolled *in vivo* trials ($N = 10$) (7–9 therapy cycles, 5.0–5.4 MHz, 60–70.5% duty, 50–63 W/cm^2 I_{SPTP}), previously reported by Fosnight et al. [33]. Further details on all controlled *in vivo* bulk US trials can be found in the Appendix.

4.2.5 Data analysis

Tumor growth was assessed and effective tumor diameters were computed after tissue processing. Using the binary histology masks for all trials with tumors ($N = 17$), effective tumor diameters were calculated for the tissue cross-section from the imaging/therapy plane with greater tumor area using the MATLAB built-in function **regionprops()**. Effective tumor diameter was defined as the length of the major axis of the ellipse with the same normalized second central moments as the segmented tumor region.

Previous uncontrolled HIFU and bulk US experiments [33] which utilized echo decorrelation imaging feedback to monitor thermal therapy, without using the proposed control algorithm, are referred to here as uncontrolled groups. For consistent comparison with the controlled groups, cumulative echo decorrelation maps for HIFU ($N = 13$) and bulk US ($N = 10$) uncontrolled trials were computed using only the first 20 RF frames from each cycle to match the controlled trials reported here.

Successfully controlled trials for both the controlled HIFU and bulk US groups were defined as trials stopped by the control algorithm when Δ_{avg} exceeded Δ_{th}. Unsuccessfully controlled trials were defined as trials that were not stopped by the control algorithm, but instead by the predefined maximum number of therapy cycles ($M = 18$). HIFU and bulk US trials were excluded from all statistical analyses if they stopped due to software malfunction or if they incurred problems in histology processing. Also excluded were HIFU trials with lesions that extended from the top to bottom boundaries of the liver lobe [33].

In a *post hoc* analysis, both the controlled and uncontrolled groups were assessed for complete treatment of the control ROI. For HIFU exposures, the control ROI (1×1 mm^2)

was placed 2 mm below the tissue surface for both controlled and uncontrolled HIFU trials. For bulk US exposures, the control ROI (18 mm $\times$ 6 mm) was placed 2 mm below the tissue surface for both controlled and uncontrolled bulk US trials. The control ROI was considered fully treated if it was completely encompassed by the treated tissue (partial or no TTC uptake region) boundaries.

In a retrospective analysis, the effect of motion and noise correction on all trials for the controlled group was assessed by comparing Δ_{avg} with and without applying the compensation method of Eq. (4.1). For both HIFU and bulk US exposures, the control ROI (1×1 mm^2 and 18 mm $\times$ 6 mm respectively) was placed 2 mm below the tissue surface and the computation ROI for the echo decorrelation map was adjusted to the same coordinates recorded during the *in vivo* experiment. Means and standard deviations of corrected and uncorrected Δ_{avg} were computed for both controlled HIFU and bulk US trials. Differences between corrected and uncorrected Δ_{avg} were tested statistically using the two-sample t-test (one-tailed, significance criterion $p < 0.05$) for both controlled HIFU and bulk US trials.

To statistically compare the ablation outcomes of controlled and uncontrolled groups for HIFU and bulk US trials, thermal lesions for each trial were characterized by their dimensions. For HIFU treatments, lesion width, depth, and area of treated regions (partial or no TTC uptake) were computed from segmented histologic images using a custom MATLAB application. Lesion depth was defined as the difference between the deepest treated point along the array axis and its projection on the tissue surface. Lesion width was defined as the difference between the left and right edges of the treated region along the azimuthal direction at half the measured lesion depth. Lesion area was calculated as the total area of all pixels classified as treated tissue. Ablation rate was computed as the treated area (cm^2) per unit treatment time in minutes (min).

For bulk US treatments, treated lesion dimensions and ablation rate for each trial were computed as described for HIFU trials. Lesion depths were excluded from the analysis

because all treated regions extended from the top to bottom boundaries of the rabbit liver lobe.

Statistical analysis of lesion dimensions and ablation rate were done using R software (R Foundation, Vienna, Austria). Means and standard errors of lesion width, area, and ablation rate were computed for the controlled and uncontrolled groups. Normality of data was tested using the Shapiro-Wilk test [123] with the significance criterion $p < 0.05$. Equality of variances between the controlled and uncontrolled groups was tested using the two-sample F-test. For normally distributed groups with equal variances, the difference in means was tested statistically using the two-sample t-test (significance criterion $p < 0.05$). For normally distributed groups with unequal variances, the difference in means was tested statistically using Welch's two-sample t-test (significance criterion $p < 0.05$). For non-normally distributed groups with equal variances, the difference in medians was tested statistically using the two-sample Wilcoxon signed-rank test [129] (significance criterion $p < 0.05$). For non-normally distributed groups with unequal variances, the difference in cumulative data distributions was tested statistically using the two-sample Kolmogorov-Smirnov (KS) test [130] (significance criterion $p < 0.05$).

To investigate the effect of different tissue types on HIFU ablation outcomes and treatment time, additional statistical analyses for trials treating liver only or VX2 tumor only (i.e., HIFU lesions within the tumor margins) were performed. Lesion dimensions, ablation rate, and treatment time were compared for liver-only vs. tumor-only for both controlled and uncontrolled groups using the methods described above.

Prediction of US thermal ablation in rabbit liver and VX2 tumor using echo decorrelation and integrated backscatter imaging was assessed by computing receiver operating characteristic (ROC) curves and area under the ROC curve (AUC) values for each group, as previously described in Section 2.2.2.e [33, 88]. ROC curves were computed by comparing thresholded corrected cumulative echo decorrelation or IBS images to segmented binary masks for each

trial [33, 88]. The rate of true-positive predictions (Sensitivity) versus the rate of false-positive predictions (1 − Specificity) was plotted over the entire range of echo decorrelation or IBS cutoffs [106]. AUC was computed using the trapezoidal rule. ROC curves and AUC values were computed separately for echo decorrelation and IBS prediction of treated and ablated regions in liver and VX2 tumor for HIFU exposures, bulk US exposures, and all exposures combined within both the controlled and uncontrolled groups.

AUC values were tested for statistical significance against the null hypothesis (AUC = 0.5) using a general model for the AUC standard error [106] (one-tailed, significance criterion $p < 0.05$). Differences between AUC values (controlled vs. uncontrolled groups, VX2 tumor vs. liver, and echo decorrelation vs. IBS prediction) were tested using the method of DeLong et al. [107, 108] (significance criterion $p < 0.05$, two-tailed). Statistical tests of AUC were adjusted using effective sample sizes determined from the maximum packing density (hexagonal packing) of circular windows with diameter matching the spatial resolution of echo decorrelation images ($d = 2.355$ mm for a Gaussian correlation window width $\sigma = 1$ mm) as previously described in Section 2.2.2.e [33, 88].

Differences between average cumulative decorrelation ($\log_{10}$-scaled decorrelation per ms) or average cumulative decibel-scaled IBS values in treated vs. non-treated, as well as in ablated vs. non-ablated rabbit liver and VX2 tumor were tested statistically using the two-sample t-test (one-tailed, significance criterion $p < 0.05$) for both the controlled and uncontrolled groups. Differences between average cumulative decorrelation or average cumulative decibel-scaled IBS values for controlled versus uncontrolled trials, or in VX2 tumor versus rabbit liver, were tested using the two-sample t-test (two-tailed, significance criterion $p < 0.05$), as previously employed by Fosnight et al. [33].

To assess the ability of echo decorrelation and IBS imaging to predict ablated area (i.e., area of the tissue region with no TTC uptake), optimal echo decorrelation and IBS thresholds for local ablation prediction in rabbit liver and VX2 tumor were determined from ROC curves

computed for all exposures combined from both controlled and uncontrolled trials ($N = 43$). Optimum cutoffs were selected as the thresholds nearest to the top-left corner of the ROC curves. Using these cutoffs, absolute and normalized RMS errors between predicted and ablated areas were computed separately for HIFU and bulk exposures from both controlled and uncontrolled groups as previously described in Section 2.2.4. The same analysis was employed to assess the ability of echo decorrelation and IBS imaging to predict treated area (i.e., area of the tissue region with partial or no TTC uptake). A similar method was previously employed by Fosnight et al. [33], using ROC curves computed for bulk US exposures only.

4.3 Results

Tissue sectioning results revealed that 22 out 24 implanted VX2 tumors were successfully grown in two weeks. Mean and standard deviation of measured effective diameters for the ablated VX2 tumors ($N = 17$) was 9.57 ± 5.24 mm. Effective tumor diameters for each the controlled HIFU ($N = 7$) and bulk US ($N = 10$) thermal ablation trial are shown in Table A.4 and A.5 respectively.

Four controlled trials were excluded from further analysis, including 2 trials out of 14 attempts for the controlled HIFU group and 2 trials out of 10 attempts for the controlled bulk US group. One HIFU trial was successfully stopped by the control algorithm after only one therapy cycle when Δ_{avg} exceeded Δ_{th}, resulting in a very small HIFU lesion and inconclusive TTC-stained gross histology. Another HIFU trial with a lesion extending from the top to bottom boundary of the liver lobe was also excluded, as done in the previous uncontrolled *in vivo* ablation study [33]. One bulk US trial was stopped prematurely due to synchronization problems in data acquisition, resulting in erroneously high decorrelation. Another bulk US trial encountered a software malfunction due to an unknown operating system error, leading to a sudden restart of the computer.

The modified closed loop control algorithm, employing similar stopping criteria for both HIFU ($N = 12$) and bulk US ($N = 8$) ablation experiments, successfully ceased treatment when the control threshold ($\log_{10}$-scaled echo decorrelation per ms: -2.3) was exceeded in all successfully controlled trials. Treatment (defined as a region of partial or no TTC uptake) was confirmed in all successfully controlled trials for both series of experiments. The control ROI (18 mm $\times$ 6 mm) for bulk US treatments was completely treated (i.e., falling within the region of partial or no TTC uptake) in 7 out of 8 controlled trials (mean $\pm$ standard deviation $99.5\% \pm 1.1\%$ of full ROI treatment) and 8 out of 10 uncontrolled trials ($98.5\% \pm 5.5\%$ of full ROI treatment). The control ROI (1×1 mm^2) for HIFU treatments was fully treated in 6 out of 12 controlled trials ($87.9\% \pm 19.7\%$ of full ROI treatment) and 10 out of 13 uncontrolled trials ($87.5\% \pm 29.7\%$ of full ROI treatment).

Means and standard deviations for the corrected vs. uncorrected Δ_{avg} inside the control ROI were -1.99 ± 0.18 vs. -2.04 ± 0.20 for the HIFU controlled group and -2.05 ± 0.20 vs. -2.06 ± 0.20 for the bulk US controlled group. There were no significant differences between corrected and uncorrected Δ_{avg} values for either controlled HIFU or bulk US trials.

Histologic (I), hybrid B-mode/echo decorrelation (II), and hybrid B-mode/IBS (III) images for HIFU and bulk US controlled trials are shown in Fig. (4.4)–(4.8). In the tissue sections, the red, black, blue, and green boundaries indicate the segmented tissue, tumor, treated (partial or no TTC uptake), and ablated (no TTC uptake) regions. In the US images (II) and (III), the white line indicates segmented tissue boundaries and the yellow dashed line represents the optimum prediction threshold for local tissue ablation for both controlled and uncontrolled US exposures ($N = 43$) using echo decorrelation imaging ($\log_{10}$-scaled echo decorrelation per ms: -2.9) and IBS imaging (2.3 dB), respectively. Echo decorrelation and IBS prediction of thermal lesioning showed reasonable agreement with the TTC-stained histology for HIFU and bulk experiments, except for the trial treating a tumor with a large necrotic core, as shown in Fig. 4.5(G).

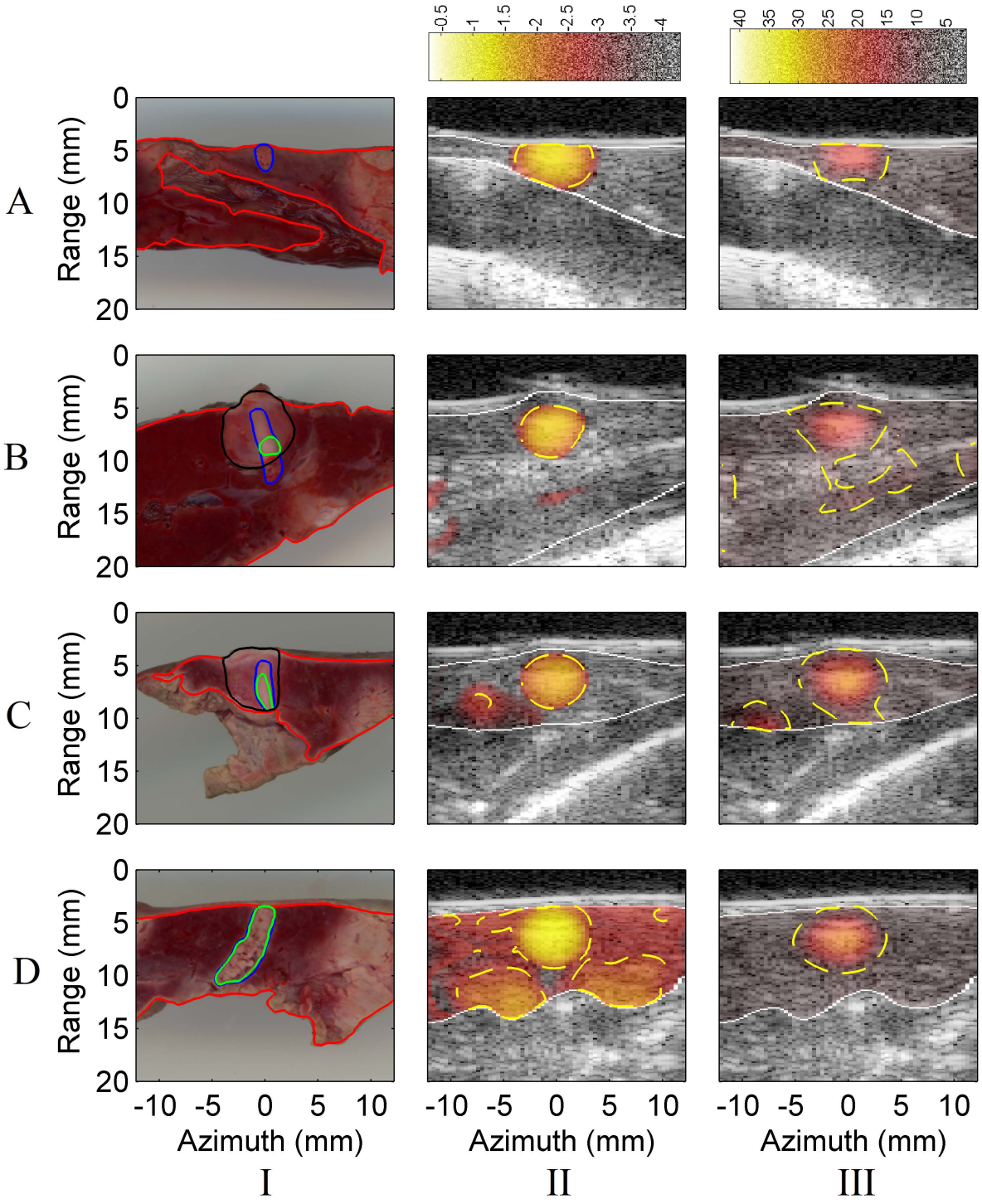

Figure 4.4: Histologic, hybrid B-mode/echo decorrelation, and hybrid B-mode/IBS images for HIFU controlled trials. In the tissue sections, the red, black, blue, and green boundaries indicate the segmented tissue, tumor, treated, and ablated regions. In the US images, the white line indicates segmented tissue boundaries and the yellow dashed line represents the optimum prediction threshold for local tissue ablation for all US exposures of both groups.

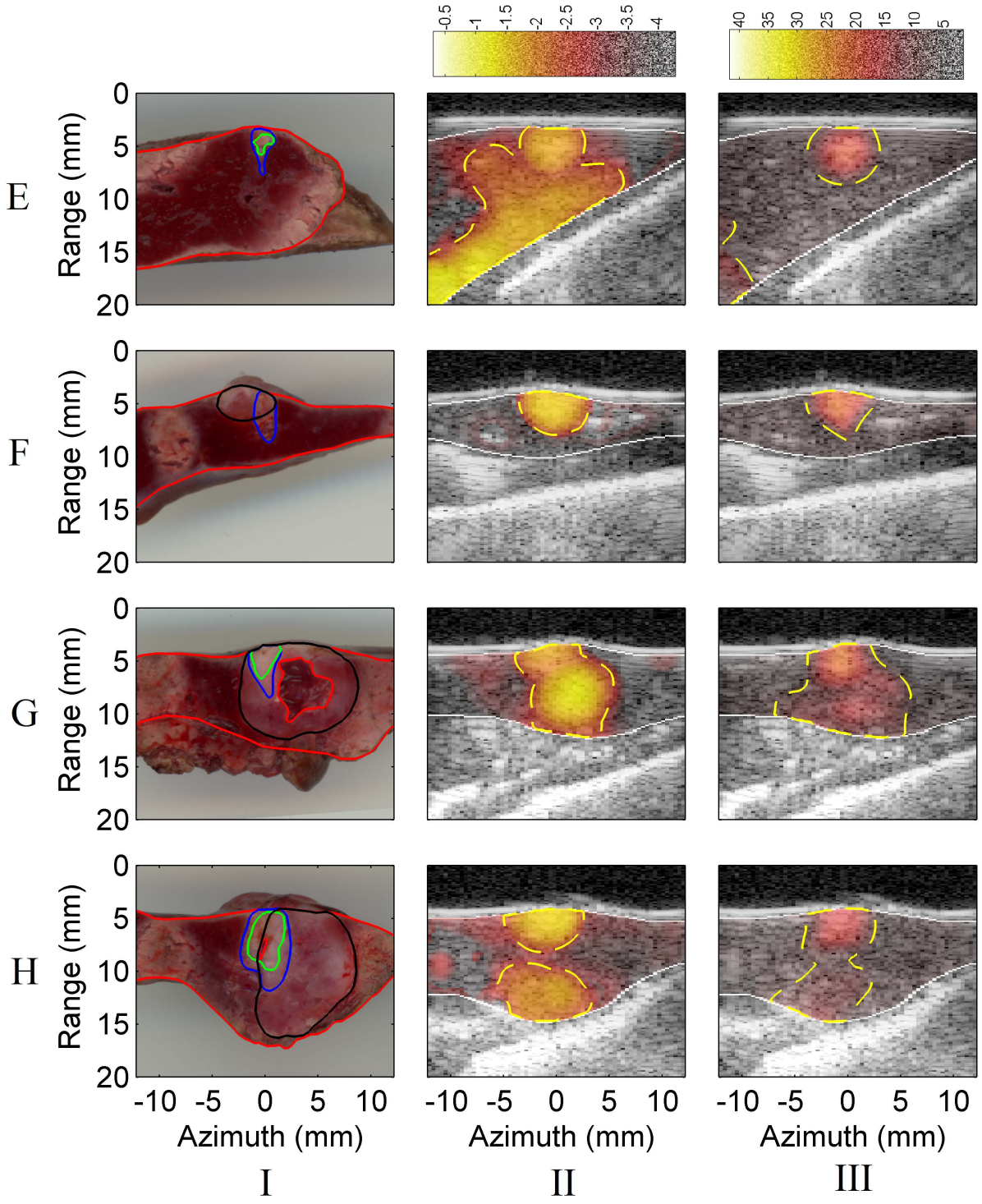

Figure 4.5: Continued histologic, hybrid B-mode/echo decorrelation, and hybrid B-mode/IBS images for HIFU controlled trials.

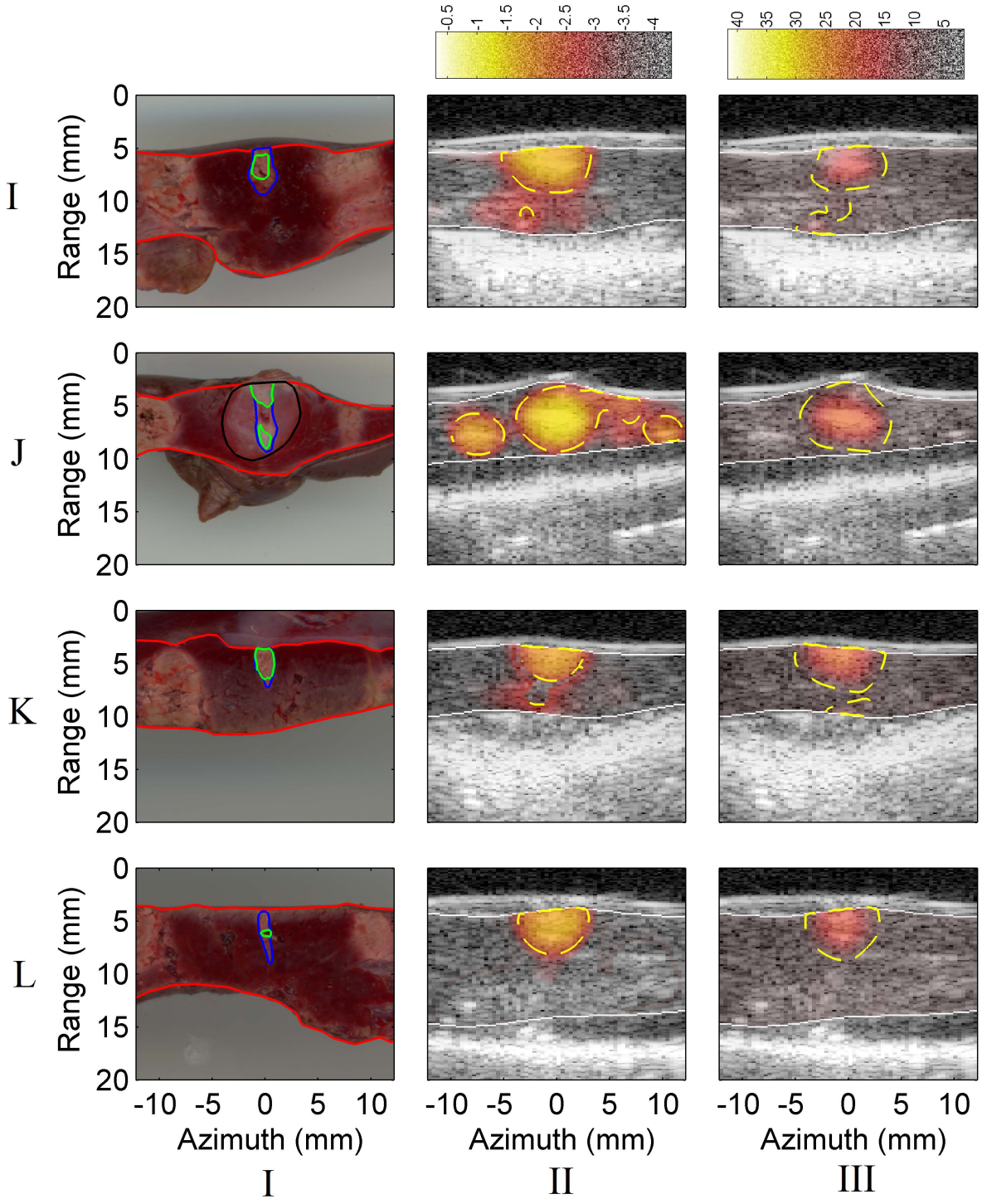

Figure 4.6: Continued histologic, hybrid B-mode/echo decorrelation, and hybrid B-mode/IBS images for the HIFU controlled trials.

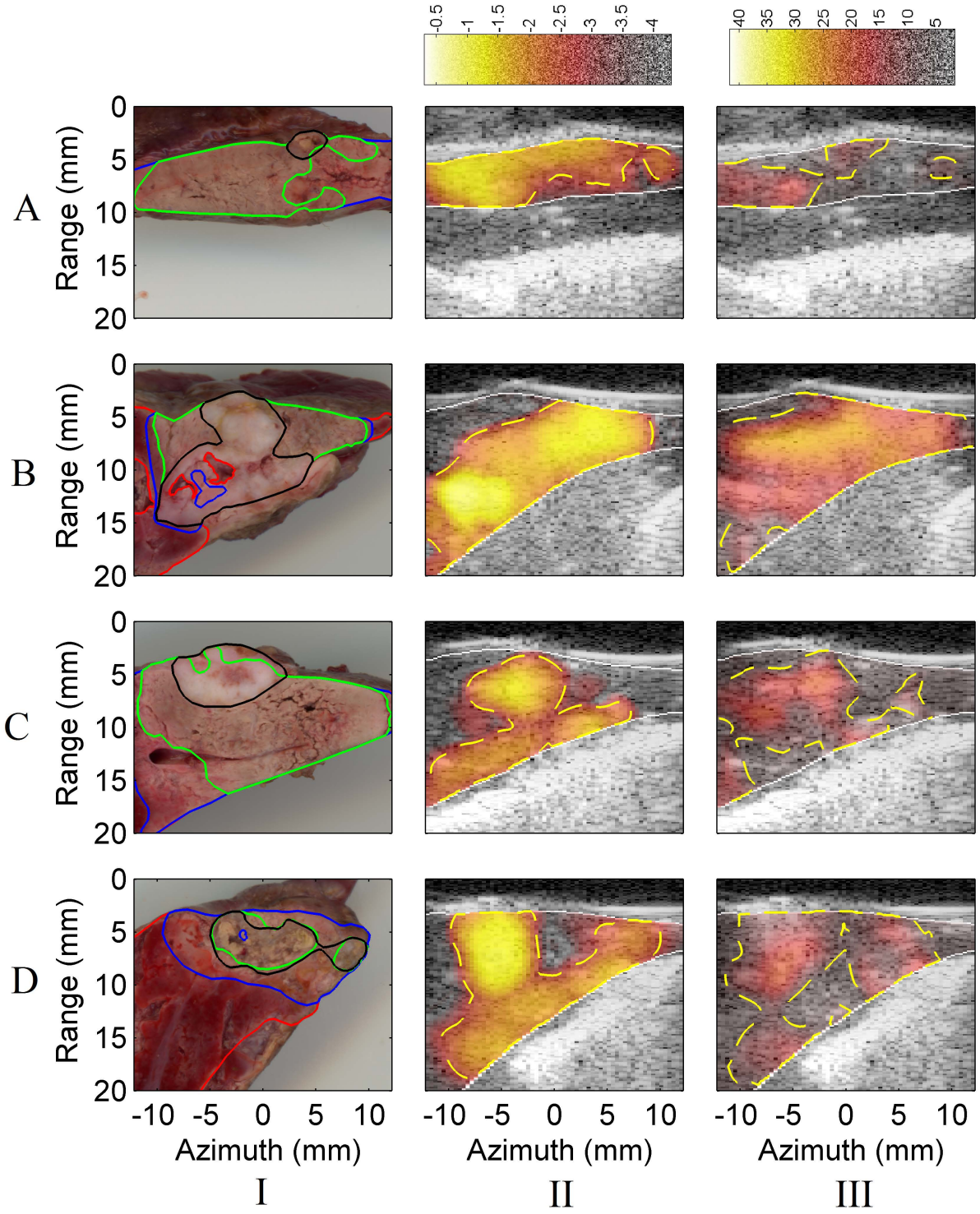

Figure 4.7: Histologic, hybrid B-mode/echo decorrelation, and hybrid B-mode/IBS images for bulk US controlled trials. In the tissue sections, the red, black, blue, and green boundaries indicate the segmented tissue, tumor, treated, and ablated regions. In the US images, the white line indicates segmented tissue boundaries and the yellow dashed line represents the optimum prediction threshold for local tissue ablation for all US exposures.

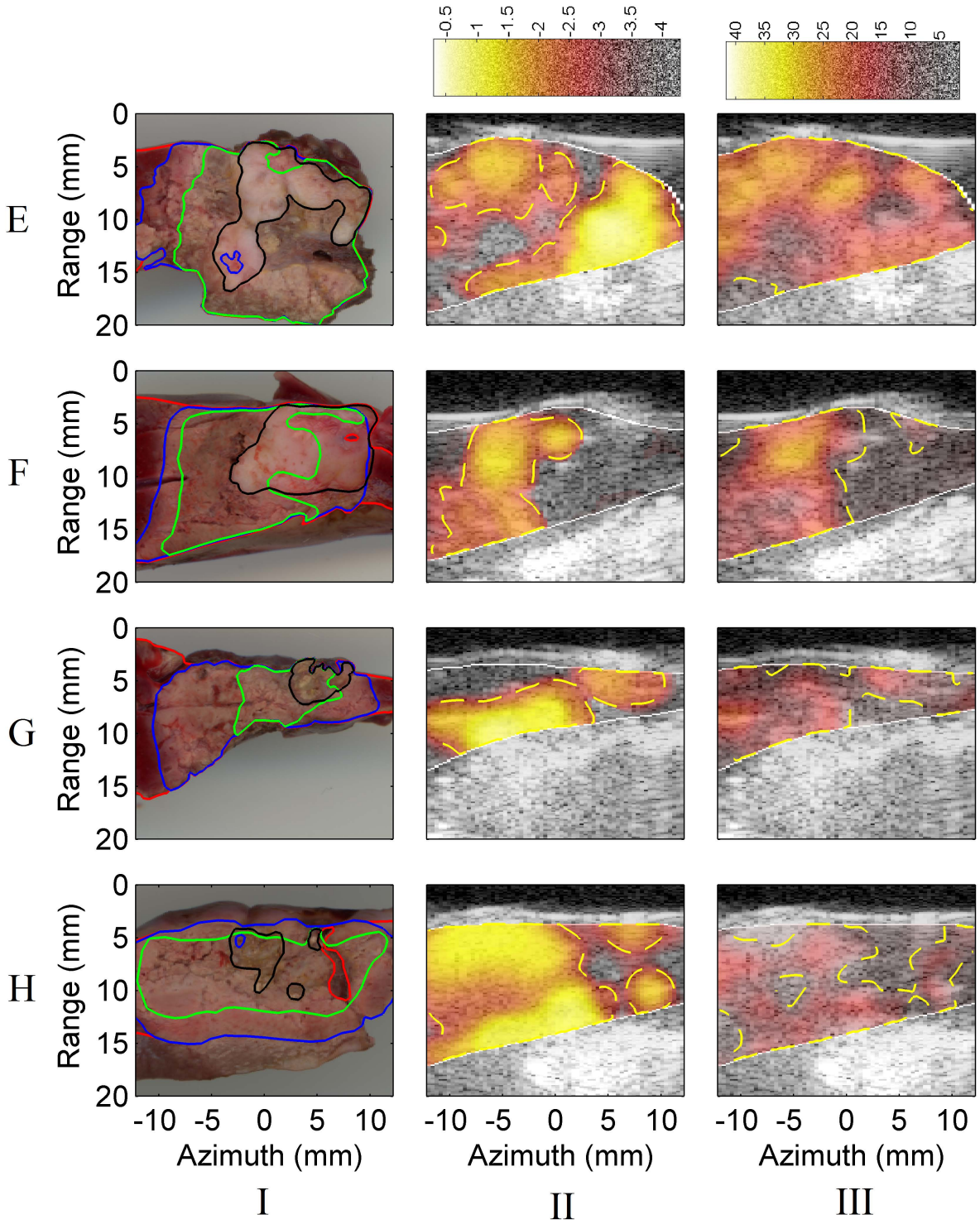

Figure 4.8: Continued histologic, hybrid B-mode/echo decorrelation, and hybrid B-mode/IBS images for bulk US controlled trials.

Statistical analyses of ablation outcomes and treatment time for all successfully controlled ($N = 12$) and uncontrolled ($N = 13$) HIFU trials are shown in Fig. 4.9(a)–(d). For lesion widths (Fig. 4.9(a)), means ± standard errors were 2.10 ± 0.27 mm for the controlled group and 2.65 ± 0.27 mm for the uncontrolled group. For lesion depths, means ± standard errors were 4.69 ± 0.41 mm for the controlled group and 4.56 ± 0.54 mm for the uncontrolled group. For lesion areas (Fig. 4.9(b)), means ± standard errors were 0.10 ± 0.02 cm^2 for the controlled group and 0.12 ± 0.02 cm^2 for the uncontrolled group. For treatment times (Fig. 4.9(c)), means ± standard errors were 14.5 ± 3.31 s for the controlled group and 33.9 ± 0.64 s for the uncontrolled group. For ablation rates (Fig. 4.9(d)), means ± standard errors were 0.48 ± 0.06 cm^2/min for the controlled group and 0.22 ± 0.04 cm^2/min for the uncontrolled group. All lesion dimensions and ablation rates passed the Shapiro normality test ($p > 0.05$) and the F-test for equality of variances ($p > 0.05$). Controlled trials had significantly higher average ablation rate than uncontrolled trials ($p = 8.4 \cdot 10^{-4}$). There were no significant differences between lesion dimensions for the controlled group vs. the uncontrolled group. Controlled trials had smaller average lesion width, depth, and area than the uncontrolled trials ($p = 0.170$, $p = 0.842$, and $p = 0.457$, respectively). Treatment time data failed the normality ($p < 0.05$) and equality of variances ($p = 3.5 \cdot 10^{-6}$) tests. Based on the KS test, there was a significant difference between distributions of treatment times ($p = 3.4 \cdot 10^{-4}$) for the controlled group vs. uncontrolled group, consistent with smaller mean treatment time for the controlled group (14.5 ± 3.31 s compared to 33.9 ± 0.64 s).

Statistical analyses of ablation outcomes and treatment time for HIFU trials treating rabbit liver only are shown in Fig. 4.10(a)–(d) for controlled ($N = 6$) and uncontrolled ($N = 7$) groups. For lesion widths (Fig. 4.10(a)), means ± standard errors were 1.80 ± 0.24 mm for the controlled group and 3.26 ± 0.19 mm for the uncontrolled group. For lesion depths, means ± standard errors were 3.72 ± 0.29 mm for the controlled group and 5.63 ± 0.51 mm for the uncontrolled group. For lesion areas (Fig. 4.10(b)), means ± standard

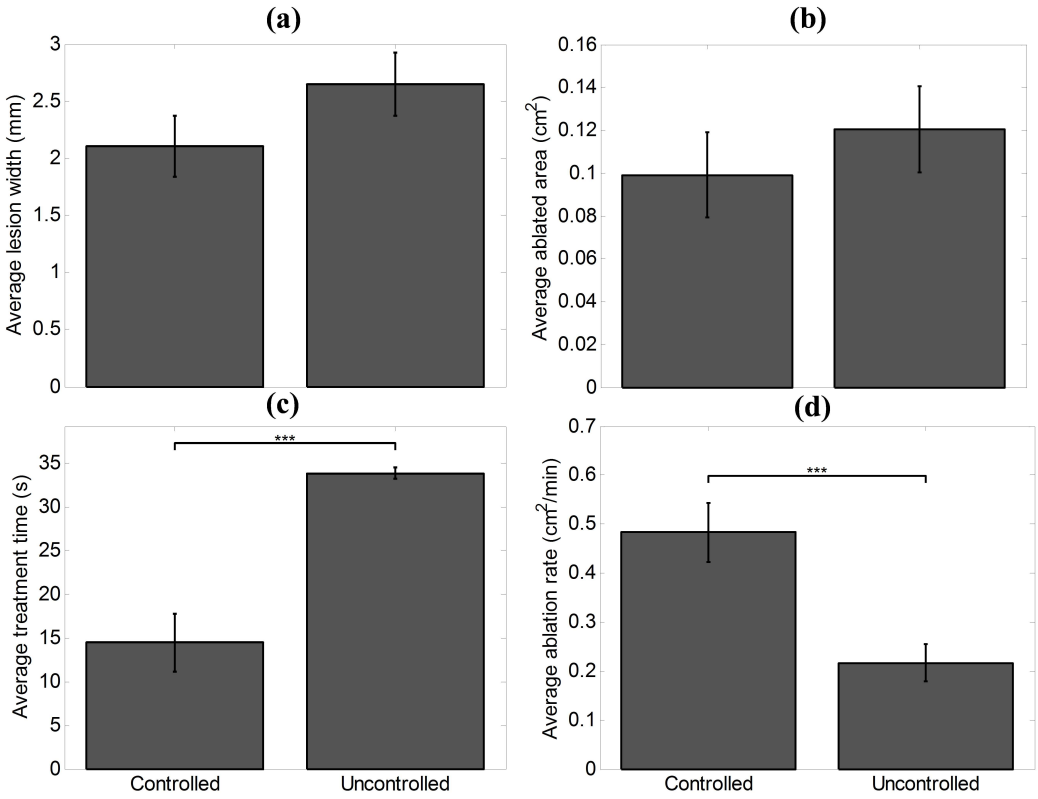

Figure 4.9: Statistical analysis of ablation results in rabbit liver and VX2 tumor for controlled and uncontrolled HIFU trials. Means and standard errors of (a) lesion width, (b) treated area, (c) treatment time, and (d) ablation rate. ($***$ $p < 10^{-3}$)

errors were 0.07 ± 0.025 cm^2 for the controlled group and 0.16 ± 0.018 cm^2 for the uncontrolled group. For treatment times (Fig. 4.10(c)), means $\pm$ standard errors were 9.2 ± 2.0 s for the controlled group and 34.7 ± 0.8 s for the uncontrolled group. For ablation rates (Fig. 4.10(d)), means $\pm$ standard errors were 0.51 ± 0.09 cm^2/min for the controlled group and 0.27 ± 0.04 cm^2/min for the uncontrolled group. All lesion dimensions and ablation rates passed the Shapiro normality test ($p > 0.05$) and the F-test for equality of variances ($p > 0.05$). Controlled trials had significantly smaller lesion width ($p = 4.6 \cdot 10^{-3}$), depth ($p = 0.010$), and area ($p = 0.022$) than the uncontrolled trials. Controlled trials had significantly higher

average ablation rate than uncontrolled trials ($p = 0.025$). Treatment time data failed the normality test ($p < 0.05$), but passed the equality of variances test ($p = 0.07$). Based on the Wilcoxon signed-rank test, median treatment time for controlled trials was significantly less than uncontrolled trials ($p = 2.5 \cdot 10^{-3}$).

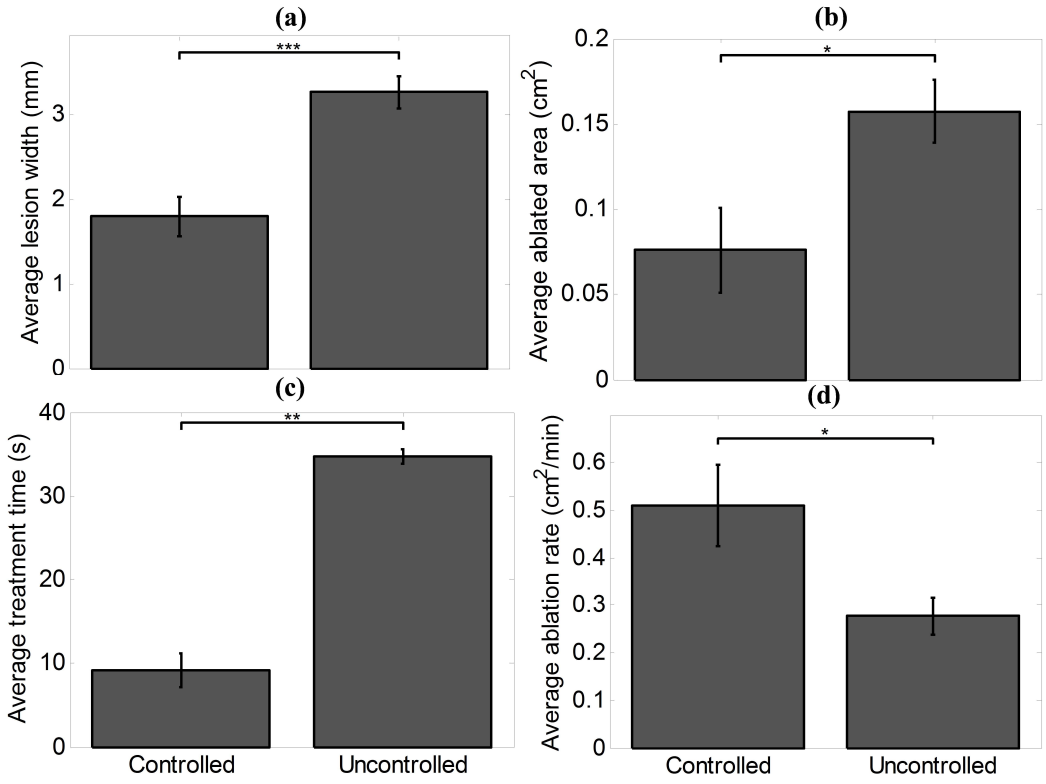

Figure 4.10: Statistical analysis of ablation results for controlled and uncontrolled HIFU trials treating rabbit liver only. Means and standard errors of (a) lesion width, (b) treated area, (c) treatment time, and (d) ablation rate. ($* \; p < 0.05$, $** \; p < 10^{-2}$, and $*** \; p < 10^{-3}$)

Statistical analyses of ablation outcomes and treatment time for HIFU trials treating VX2 tumor only are shown in Fig. 4.11(a)–(d) for controlled ($N = 3$) and uncontrolled ($N = 5$) groups. For lesion widths (Fig. 4.11(a)), means $\pm$ standard errors were 1.86 ± 0.20 mm for the controlled group and 1.75 ± 0.42 mm for the uncontrolled group. For

lesion depths, means ± standard errors were 5.19 ± 0.65 mm for the controlled group and 3.08 ± 0.87 mm for the uncontrolled group. For lesion areas (Fig. 4.11(b)), means ± standard errors were 0.09 ± 0.012 cm^2 for the controlled group and 0.06 ± 0.031 cm^2 for the uncontrolled group. For treatment times (Fig. 4.11(c)), means ± standard errors were 20.3 ± 8.9 s for the controlled group and 33.3 ± 1.1 s for the uncontrolled group. For ablation rates (Fig. 4.11(d)), means ± standard errors were 0.39 ± 0.18 cm^2/min for the controlled group and 0.11 ± 0.06 cm^2/min for the uncontrolled group. All lesion dimensions passed the Shapiro normality test ($p > 0.05$) and the F-test for equality of variances ($p > 0.05$). Ablation rates failed the normality test ($p < 0.05$), but passed the equality of variances test ($p = 0.14$). There were no significant differences between lesion dimensions for the controlled and uncontrolled group. Controlled trials had larger but statistically equivalent lesion width ($p = 0.850$), depth ($p = 0.141$), and area ($p = 0.513$) than uncontrolled trials. Based on the Wilcoxon signed-rank test, median ablation rate for controlled trials was not significantly greater than uncontrolled trials ($p = 0.136$). Treatment time data failed the normality test ($p < 0.05$) and the equality of variances test ($p = 4.8 \cdot 10^{-3}$). Based on the KS test, there was no statistical difference between treatment times ($p = 0.375$) for controlled group vs. uncontrolled group.

Results of the statistical comparisons between outcomes for controlled trials treating liver only vs. VX2 tumor only showed smaller but statistically equivalent lesion width ($t = -0.18$, $p = 0.739$), area ($t = -0.35$, $p = 0.739$), ablation rate ($t = -0.35$, $p = 0.512$), and treatment time ($D = 0.5$, $p = 0.69$), but significantly smaller lesion depth ($t = -2.46$, $p = 0.0438$) in treated liver compared to treated tumor. However, uncontrolled trials treating liver only had significantly greater lesion width ($t = 3.65$, $p = 0.004$), depth ($t = 2.70$, $p = 0.023$), area ($t = 2.89$, $p = 0.016$), and ablation rate ($t = 2.43$, $p = 0.035$), but statistically equivalent longer treatment time ($U = 23$, $p = 0.343$) compared to trials treating tumor only.

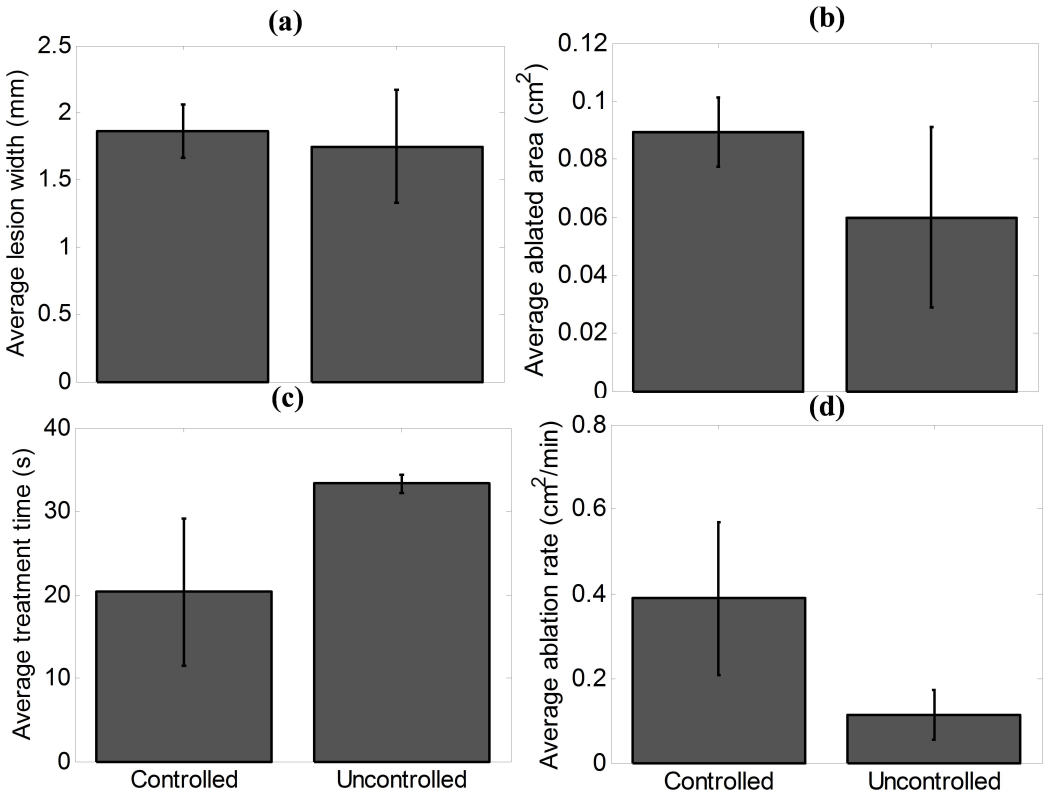

Figure 4.11: Statistical analysis of ablation results for controlled and uncontrolled HIFU trials treating VX2 tumor only. Means and standard errors of (a) lesion width, (b) treated area, (c) treatment time, and (d) ablation rate.

Ablation outcomes and treatment time statistics for controlled and uncontrolled bulk US trials are shown in Fig. 4.12(a)–(d). For lesion widths (Fig. 4.12(a)), means ± standard errors were 22.17±1.28 mm for the controlled group and 24.79±0.85 mm for the uncontrolled group. For lesion areas (Fig. 4.12(b)), means ± standard errors were 2.04±0.24 cm^2 for the controlled group and 2.54 ± 0.26 cm^2 for the uncontrolled group. For treatment times (Fig. 4.12(c)), means ± standard errors were 52.28 ± 6.74 s for the controlled group and 75.95 ± 3.02 s for the uncontrolled group. For ablation rates (Fig. 4.12(d)), means ± standard errors were 2.50 ± 0.29 cm^2/min for the controlled group and 2.05 ± 0.24 cm^2/min for the uncontrolled

group. All data passed the Shapiro normality test ($p > 0.05$) and the F-test for equality of variances ($p > 0.05$) except that lesion areas failed the normality test ($p = 0.038$). There were no significant differences between lesion dimensions for the controlled group vs. the uncontrolled group. Controlled trials had smaller average lesion width than the uncontrolled trials ($p = 0.098$). According to the Wilcoxon signed-rank test, median area for controlled trials was not significantly smaller than uncontrolled trials ($p = 0.351$). Controlled trials were completed in significantly less time than uncontrolled trials ($p = 0.034$). Controlled trials had higher average ablation rate than uncontrolled trials ($p = 0.251$). ROC curves

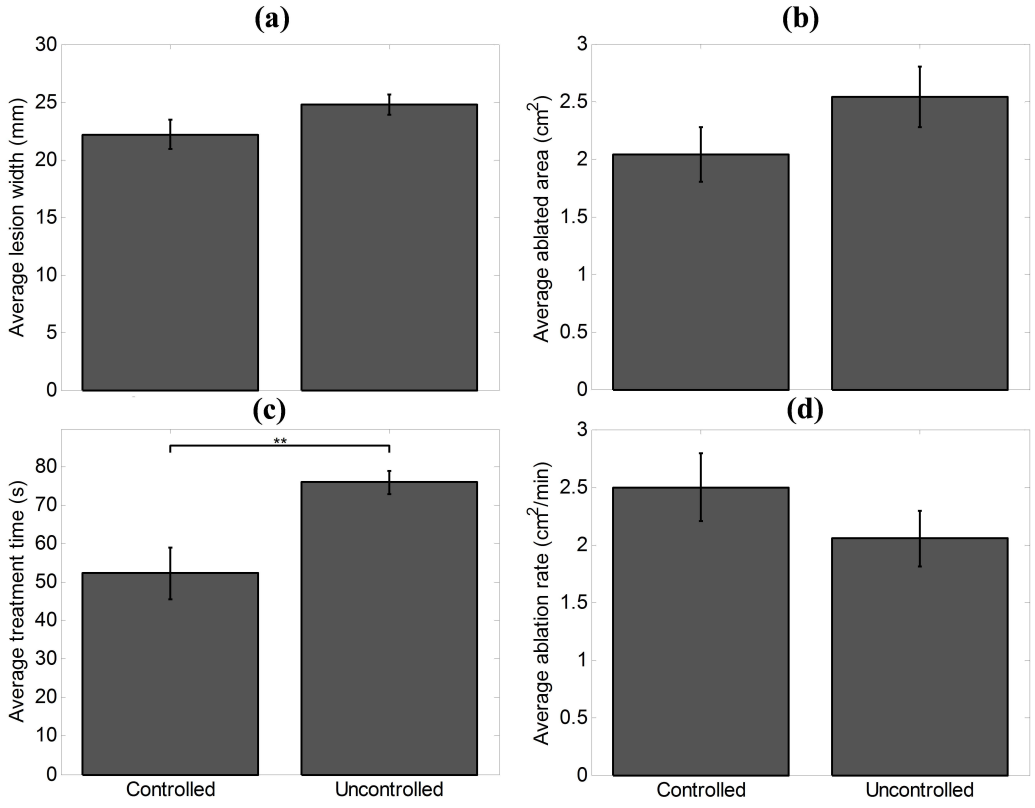

Figure 4.12: Statistical analysis of ablation results for controlled and uncontrolled bulk US trials. Means and standard errors of (a) lesion width, (b) treated area, (c) treatment time, and (d) ablation rate. ($** p < 10^{-2}$)

Table 4.1: Results of paired, one-tailed z tests comparing AUC values for echo decorrelation prediction of treated and ablated regions in liver and VX2 tumor vs. chance (AUC = 0.5) (z-statistic (p value)).

	Liver		VX2 tumor	
HIFU	Treated	Ablated	Treated	Ablated
Controlled	5.58 ($1.19 \cdot 10^{-8}$)	5.28 ($6.29 \cdot 10^{-8}$)	2.49 (0.006)	1.09 (0.139)
Uncontrolled	8.88 ($< 10^{-16}$)	7.29 ($1.55 \cdot 10^{-13}$)	1.62 (0.052)	1.55 (0.061)
Bulk				
Controlled	3.44 ($2.9 \cdot 10^{-4}$)	2.20 (0.015)	1.08 (0.140)	3.74 ($9.2 \cdot 10^{-5}$)
Uncontrolled	3.74 ($8.9 \cdot 10^{-5}$)	3.96 ($3.7 \cdot 10^{-5}$)	3.39 ($3.4 \cdot 10^{-4}$)	2.05 (0.020)
All exposures				
Controlled	12.43 ($< 10^{-16}$)	8.40 ($< 10^{-16}$)	1.82 (0.034)	2.77 ($2.8 \cdot 10^{-3}$)
Uncontrolled	19.70 ($< 10^{-16}$)	17.90 ($< 10^{-16}$)	2.54 ($5.6 \cdot 10^{-3}$)	2.72 ($3.2 \cdot 10^{-3}$)

and AUC values for echo decorrelation prediction of treatment (partial or no TTC uptake) and ablation (no TTC uptake) in rabbit liver and VX2 tumor for HIFU, bulk US, and all exposures combined are shown in Figs. (4.13)–(4.15). Statistical analysis results for comparisons between AUC values for the controlled and uncontrolled groups and relative to chance (AUC = 0.5) are shown in Table 4.1. For liver treatment and ablation, AUC values were significantly greater than chance for HIFU, bulk US, and all exposures combined for both controlled and uncontrolled trials. For VX2 tumor treatment, AUC was significantly greater than chance for controlled HIFU trials, uncontrolled bulk US trials, and all exposures combined for both controlled and uncontrolled trials. For VX2 tumor ablation, AUC was significantly greater than chance for bulk US exposures and all exposures combined for both controlled and uncontrolled trials.

Statistics of AUC comparisons between the controlled and uncontrolled groups for echo decorrelation prediction of treated and ablated regions in rabbit liver and VX2 tumor are shown in Table 4.2. In all cases, the controlled group showed statistically equivalent prediction capability compared to the uncontrolled group.

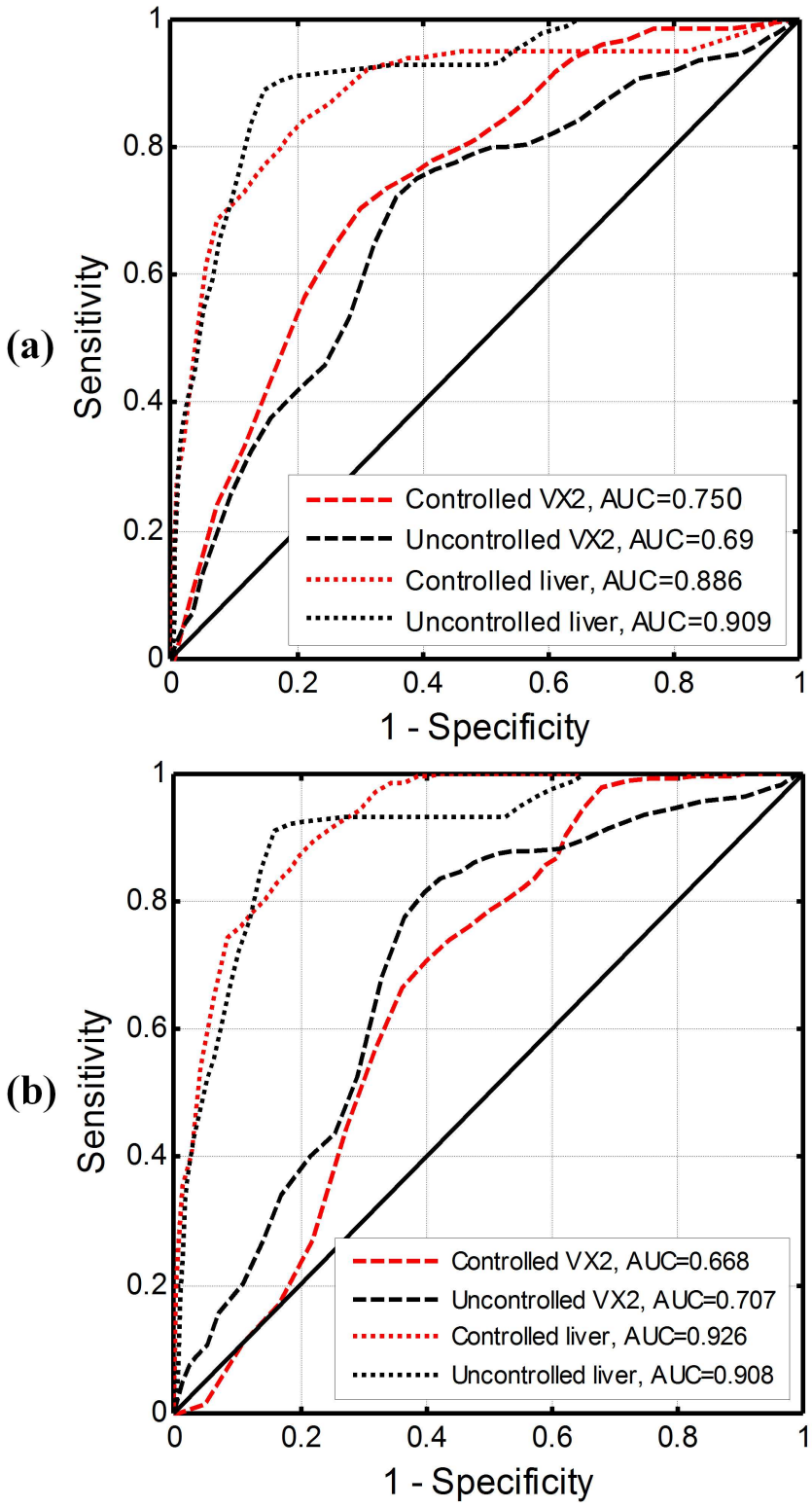

Figure 4.13: Receiver operating characteristic curves for echo decorrelation prediction of (a) treatment and (b) ablation in rabbit liver and VX2 tumor for controlled and uncontrolled HIFU experiments.

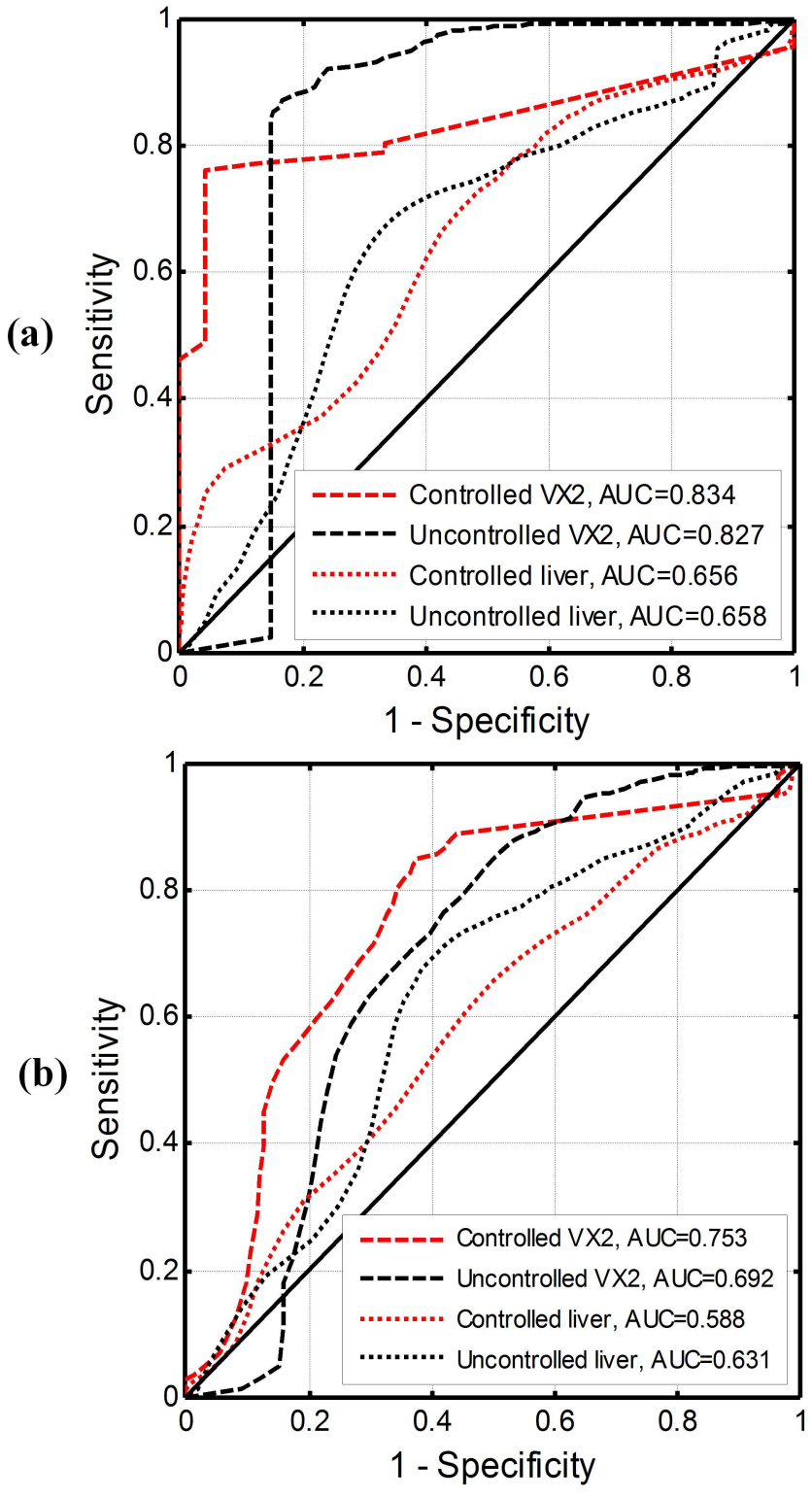

Figure 4.14: Receiver operating characteristic curves for echo decorrelation prediction of (a) treatment and (b) ablation in rabbit liver and VX2 tumor for controlled and uncontrolled bulk US experiments.

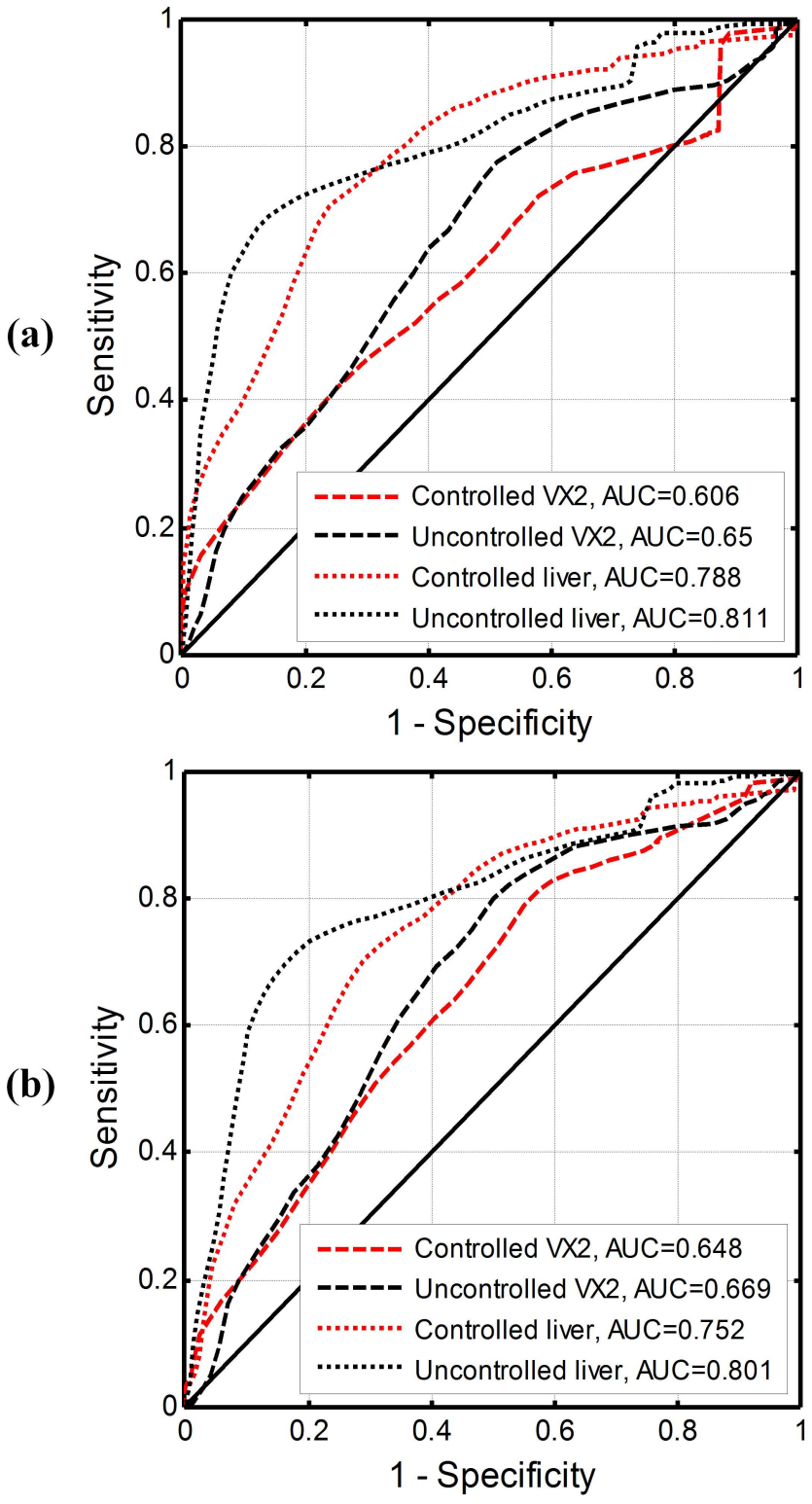

Figure 4.15: Receiver operating characteristic curves for echo decorrelation prediction of (a) treatment and (b) ablation in rabbit liver and VX2 tumor for all focused and bulk US exposures combined for controlled and uncontrolled trials.

Table 4.2: Results of two-tailed z tests comparing AUC values for echo decorrelation prediction of treated and ablated regions in liver and VX2 tumor in controlled vs. uncontrolled trials (z-statistic (p value)).

	Controlled vs. uncontrolled			
Tissue	Liver		VX2	
Exposure	Treated	Ablated	Treated	Ablated
HIFU	−0.30 (0.756)	0.16 (0.873)	0.40 (0.692)	−0.18 (0.857)
Bulk	−0.31 (0.756)	−0.94 (0.347)	0.02 (0.984)	0.53 (0.593)
All	−0.93 (0.351)	−1.51 (0.130)	−0.53 (0.597)	−0.25 (0.80)

Statistics of AUC comparisons for echo decorrelation prediction of treatment and ablation in VX2 tumor vs. liver for controlled and uncontrolled trials are shown in Table 4.3. For controlled trials, VX2 tumor treatment was predicted significantly better than rabbit liver for all exposures combined and VX2 tumor ablation was predicted significantly better than rabbit liver for bulk US exposures. For uncontrolled trials, liver treatment and ablation were predicted significantly better than VX2 tumor treatment and ablation for all exposures combined.

Table 4.3: Results of two-tailed z tests comparing AUC values for echo decorrelation prediction of treatment and ablation in VX2 tumor vs. liver for controlled and uncontrolled trials (z-statistic (p value)).

	VX2 tumor vs. liver			
Groups	Controlled		Uncontrolled	
Exposure	Treated	Ablated	Treated	Ablated
HIFU	−1.12 (0.264)	−1.48 (0.140)	−1.78 (0.076)	−1.43 (0.153)
Bulk	0.57 (0.569)	2.10 (0.037)	1.41 (0.158)	0.53 (0.596)
All	−2.91 ($3.6 \cdot 10^{-3}$)	−1.69 (0.092)	−2.68 (0.0073)	−2.09 (0.036)

Optimal echo decorrelation prediction thresholds (i.e., threshold nearest to the top-left corner of an ROC curve) and corresponding sensitivities and specificities for local ablation

(no TTC uptake) prediction in rabbit liver and VX2 tumor determined from ROC curves computed for both controlled and uncontrolled groups are shown in Table 4.4. Controlled and uncontrolled trials had approximately equivalent specificities for local ablation prediction in liver for HIFU exposures and in VX2 tumor for bulk US exposures and for all exposures combined.

Table 4.4: Optimal thresholds for local ablation prediction and corresponding sensitivities and specificities for echo decorrelation ($\log_{10}$-scaled decorrelation per ms) in liver and VX2 tumor for controlled and uncontrolled trials.

	Liver		VX2 tumor	
HIFU	Controlled	Uncontrolled	Controlled	Uncontrolled
Threshold	−2.6	−3.0	−2.3	−2.4
Sensitivity (%)	83	91	67	78
Specificity (%)	84	84	64	63
Bulk				
Threshold	−2.6	−2.7	−3.4	−2.6
Sensitivity (%)	61	68	80	67
Specificity (%)	54	62	65	67
All exposures				
Threshold	−2.8	−3.0	−2.6	−2.6
Sensitivity (%)	70	73	61	70
Specificity (%)	71	80	59	59

Means and standard errors of the $\log_{10}$-scaled cumulative echo decorrelation per ms (Δ_{cum}) in ablated and unablated rabbit liver and VX2 tumor are shown in Fig. 4.16(a)–(c) and Fig. 4.17(a)–(c) respectively. Statistical analyses of differences in means between Δ_{cum} in treated vs. non-treated, as well as in ablated vs. non-ablated rabbit liver and VX2 tumor for both controlled and uncontrolled groups are shown in Table 4.5. For HIFU exposures, both controlled and uncontrolled trials had significantly greater mean Δ_{cum} in ablated than non-ablated rabbit liver. For bulk US exposures, uncontrolled trials had significantly

greater mean Δ_{cum} in ablated than non-ablated rabbit liver. For all exposures combined, both controlled and uncontrolled trials had significantly greater mean Δ_{cum} in ablated than non-ablated rabbit liver and marginally greater mean Δ_{cum} in ablated than non-ablated VX2 tumor. Statistics of average Δ_{cum} comparisons between controlled and uncontrolled

Table 4.5: Results of paired, one-tailed t-tests comparing mean Δ_{cum} values in treated and non-treated, as well as in ablated and non-ablated regions, for liver and VX2 tumor of controlled and uncontrolled groups (t-statistic (p value, number of samples)).

	Treated vs. non-treated		Ablated vs. non-ablated	
HIFU	Liver	VX2	Liver	VX2
Controlled	3.1 ($7.4 \cdot 10^{-3}$, 9)	6.9 ($4.9 \cdot 10^{-4}$, 6)	6.4 ($6.9 \cdot 10^{-4}$, 6)	1.5 (0.104, 5)
Uncontrolled	4.0 ($7.4 \cdot 10^{-3}$, 8)	2.4 (0.030, 6)	4.3 ($1.8 \cdot 10^{-3}$, 8)	1.4 (0.125, 4)
Bulk				
Controlled	5.8 ($6.0 \cdot 10^{-4}$, 7)	1.1 (0.240, 2)	0.9 (0.200, 8)	1.6 (0.080, 8)
Uncontrolled	1.7 (0.068, 9)	0.9 (0.273, 2)	2.0 (0.040, 9)	1.3 (0.160, 3)
All exposures				
Controlled	5.3 ($4.8 \cdot 10^{-5}$, 16)	3.1 ($8.4 \cdot 10^{-3}$, 8)	2.9 ($5.6 \cdot 10^{-3}$, 14)	1.9 (0.040, 13)
Uncontrolled	3.4 ($1.8 \cdot 10^{-3}$, 17)	1.4 (0.100, 8)	3.7 ($9.5 \cdot 10^{-4}$, 17)	2.0 (0.050, 7)

groups in treated and ablated regions of rabbit liver or VX2 tumor, also between VX2 tumor and rabbit liver in treated and ablated regions of the controlled or uncontrolled groups are shown in Table 4.6. There were no significant differences between mean Δ_{cum} for controlled vs. uncontrolled trials in treated or ablated tissue. In most cases, there were no significant differences between mean Δ_{cum} in VX2 tumor vs. liver for the controlled and uncontrolled groups in treated or ablated tissue, except that for controlled HIFU trials, ablated liver had significantly larger mean Δ_{cum} than ablated VX2 tumor.

ROC curves and AUC values for IBS imaging prediction of HIFU, bulk US, and all exposures combined treatment and ablation in rabbit liver and VX2 tumor are shown in Figs. (4.18)–(4.20), similar to Figs. (4.13)–(4.15) for echo decorrelation imaging. Statistical

Table 4.6: Results of unpaired, two-tailed t-tests comparing mean $\log_{10}$-scaled Δ_{cum} for controlled vs. uncontrolled groups and VX2 tumor vs. liver in treated and ablated regions (t-statistic (p value)).

	Controlled vs. uncontrolled		VX2 vs. liver	
HIFU	Liver	VX2	Controlled	Uncontrolled
Treated	0.20 (0.842)	0.94 (0.372)	0.77 (0.460)	0.17 (0.870)
Ablated	1.22 (0.245)	0.37 (0.724)	−2.91 (0.017)	0.23 (0.830)
Bulk				
Treated	0.47 (0.641)	0.58 (0.571)	−0.70 (0.493)	−0.51 (0.617)
Ablated	0.046 (0.964)	0.65 (0.525)	0.25 (0.800)	−0.37 (0.713)
All exposures				
Treated	0.32 (0.753)	1.10 (0.281)	0.503 (0.620)	−0.22 (0.826)
Ablated	0.89 (0.379)	0.78 (0.446)	−0.36 (0.730)	−0.07 (0.940)

analysis results for paired comparisons between AUC values for controlled and uncontrolled groups against chance (AUC = 0.5) are shown in Table 4.7. For liver treatment and ablation, AUC values were significantly greater than chance for HIFU, bulk US, and all exposures combined for both controlled and uncontrolled trials. For VX2 tumor treatment, AUC was significantly greater than chance for HIFU exposures and all exposures combined for both controlled and uncontrolled trials. For VX2 tumor ablation, AUC was significantly greater than chance for controlled bulk US exposures and all exposures combined for both controlled and uncontrolled trials.

Statistics of comparisons between AUC values for IBS prediction of controlled vs. uncontrolled groups in rabbit liver and VX2 tumor are shown in Table 4.8. In most cases, the controlled group showed statistically equivalent prediction capability compared to the uncontrolled group. AUC for controlled bulk US trials was slightly greater than for uncontrolled bulk US trials for IBS prediction of VX2 tumor ablation.

Summary statistics for AUC comparisons between IBS prediction of treatment and ablation in rabbit liver and VX2 tumor of the controlled and uncontrolled groups are shown in Table 4.9. For the controlled bulk trials, VX2 tumor ablation was predicted significantly

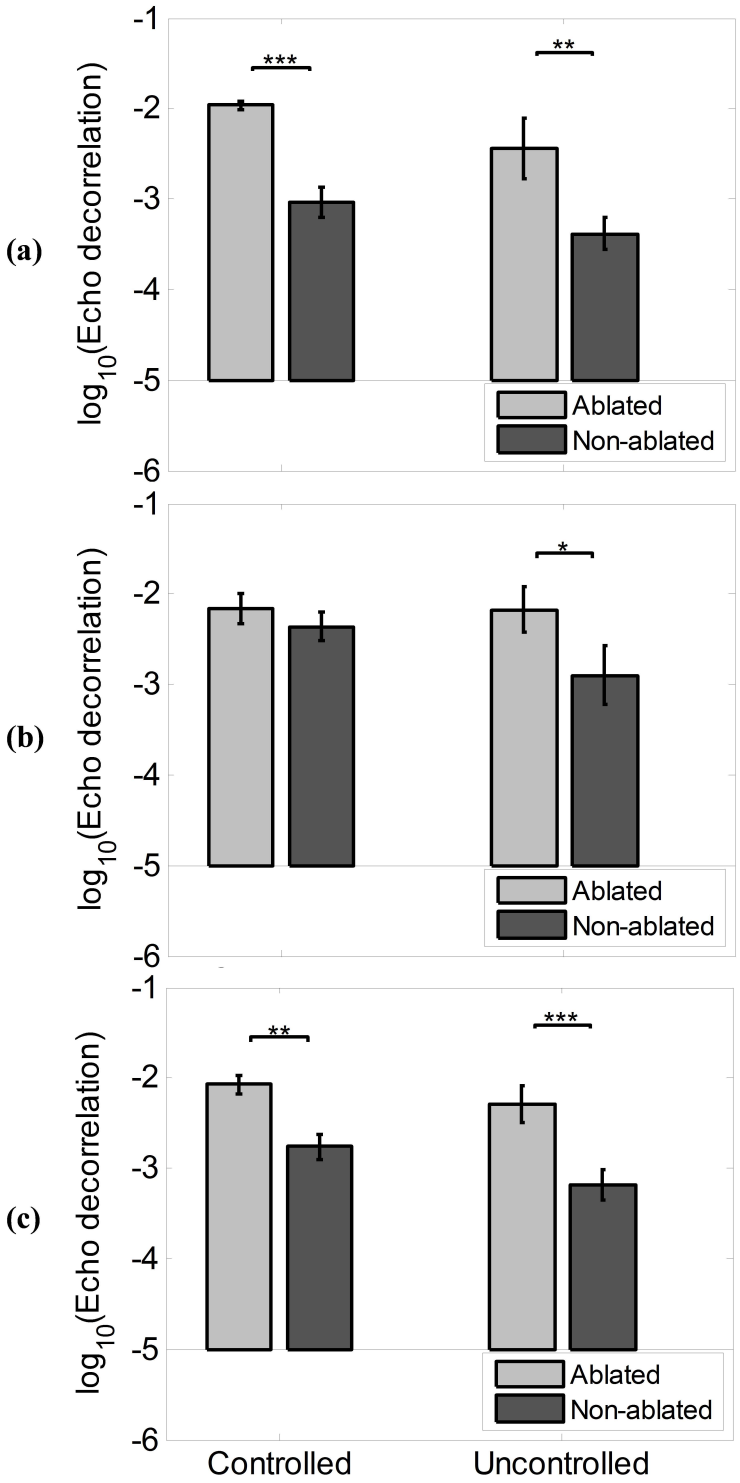

Figure 4.16: Means and standard errors of cumulative echo decorrelation ($\log_{10}$-scaled decorrelation per ms) values in ablated and non-ablated rabbit liver for controlled vs. uncontrolled (a) HIFU, (b) bulk US, and (c) all exposures combined. ($* \; p < 0.05$, $** \; p < 10^{-2}$, and $*** \; p < 10^{-3}$)

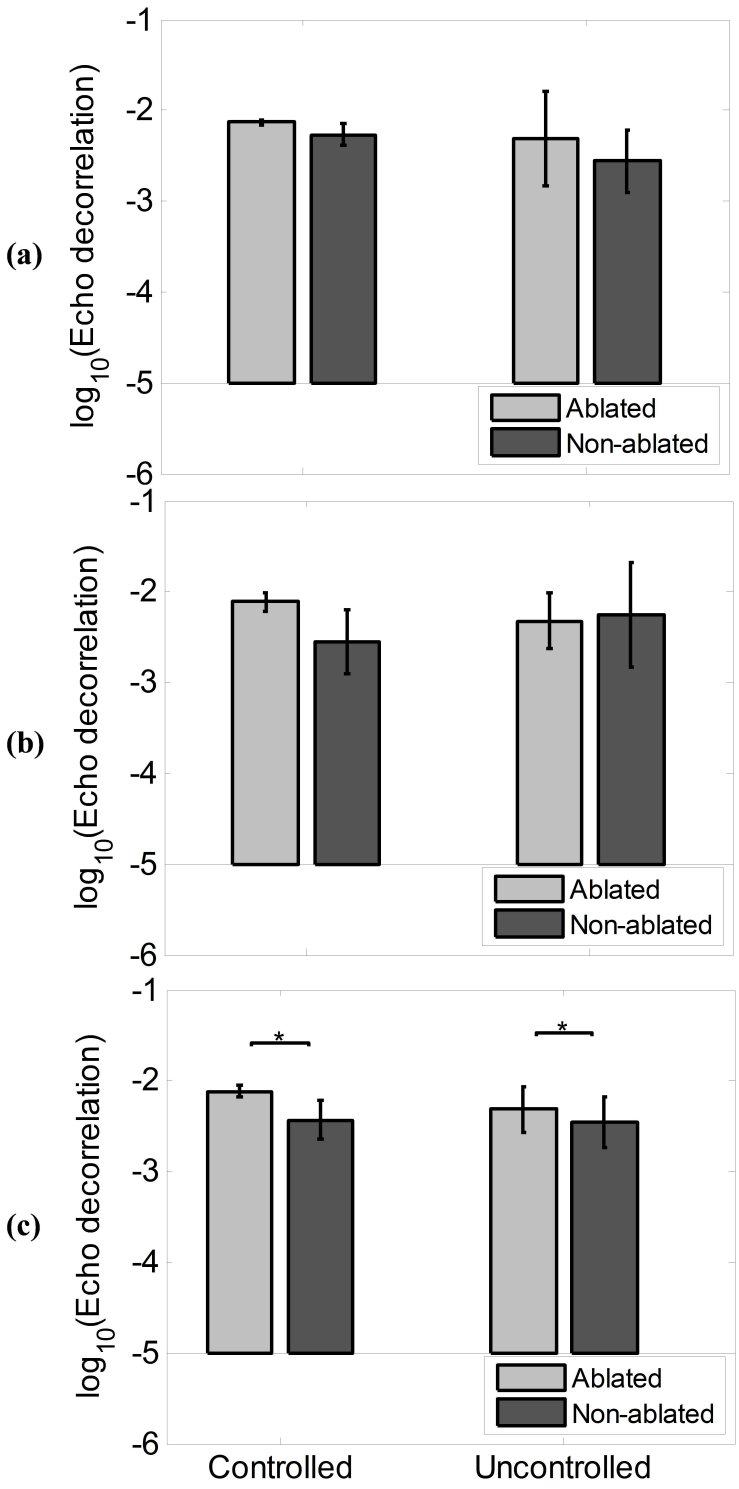

Figure 4.17: Means and standard errors of cumulative echo decorrelation ($\log_{10}$-scaled decorrelation per ms) values in ablated and non-ablated VX2 tumor for controlled vs. uncontrolled (a) HIFU, (b) bulk US, and (c) all exposures combined. ($* \; p < 0.05$)

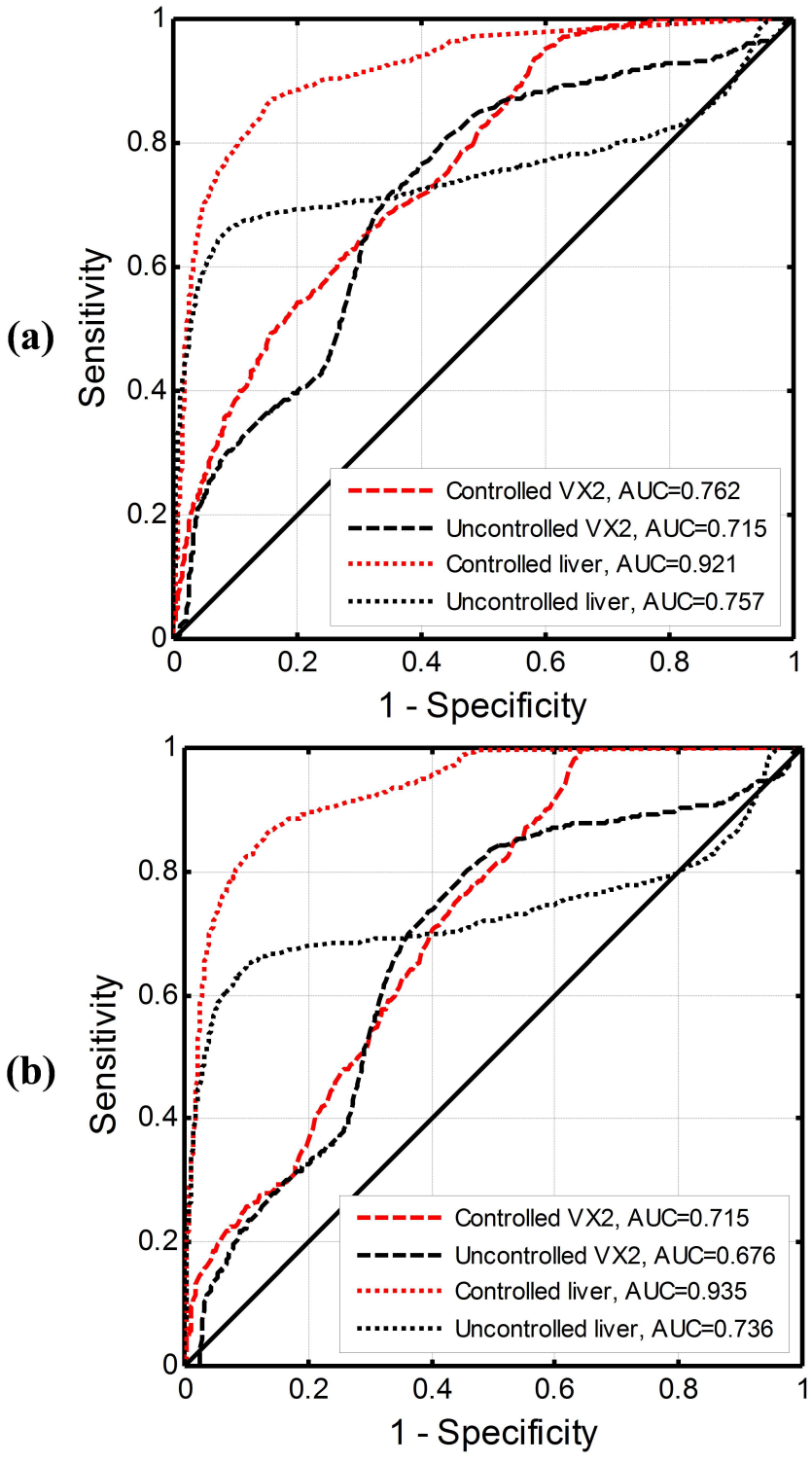

Figure 4.18: Receiver operating characteristic curves for integrated backscatter prediction of (a) treatment and (b) ablation in rabbit liver and VX2 tumor for the controlled and uncontrolled HIFU experiments.

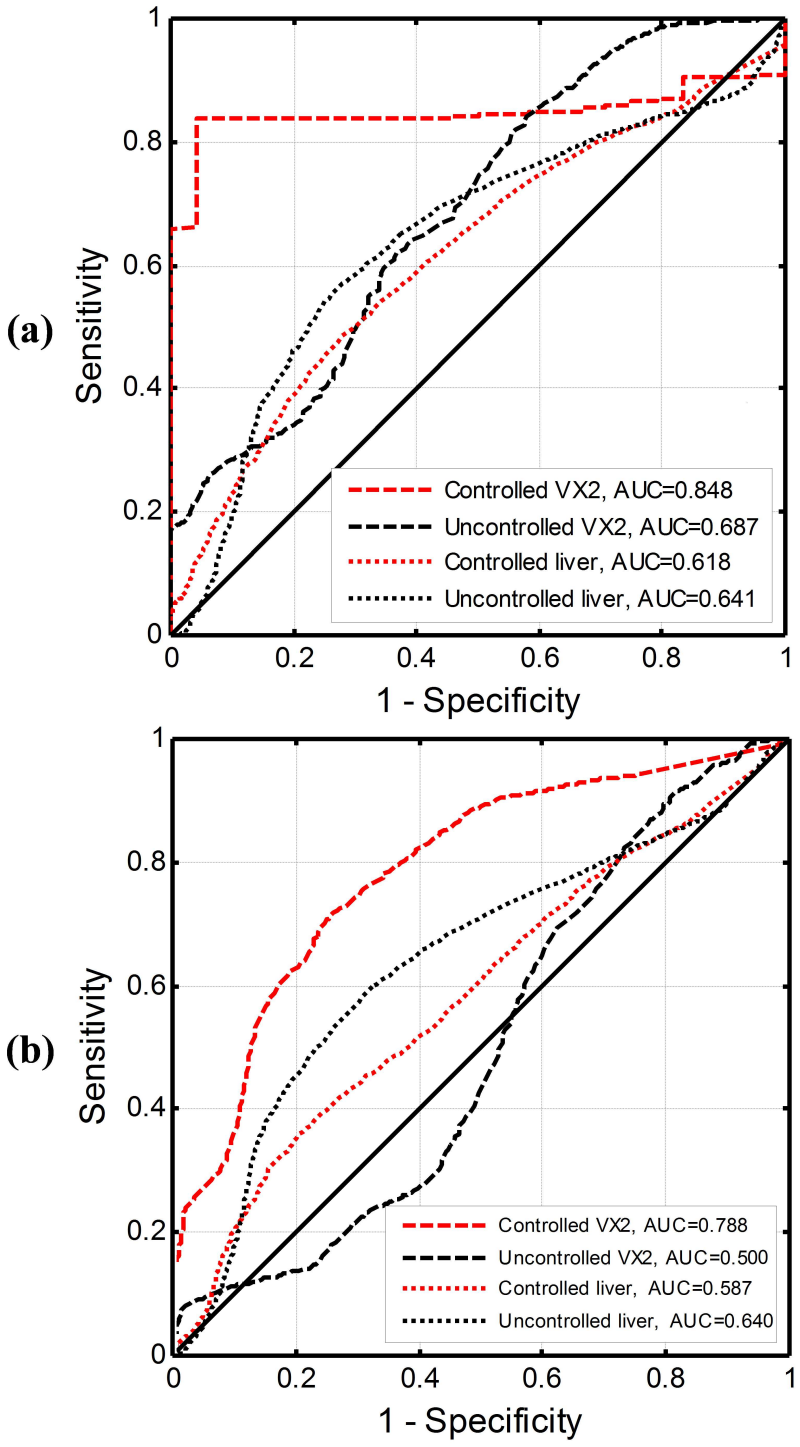

Figure 4.19: Receiver operating characteristic curves for integrated backscatter prediction of (a) treatment and (b) ablation in rabbit liver and VX2 tumor for the controlled and uncontrolled bulk US experiments.

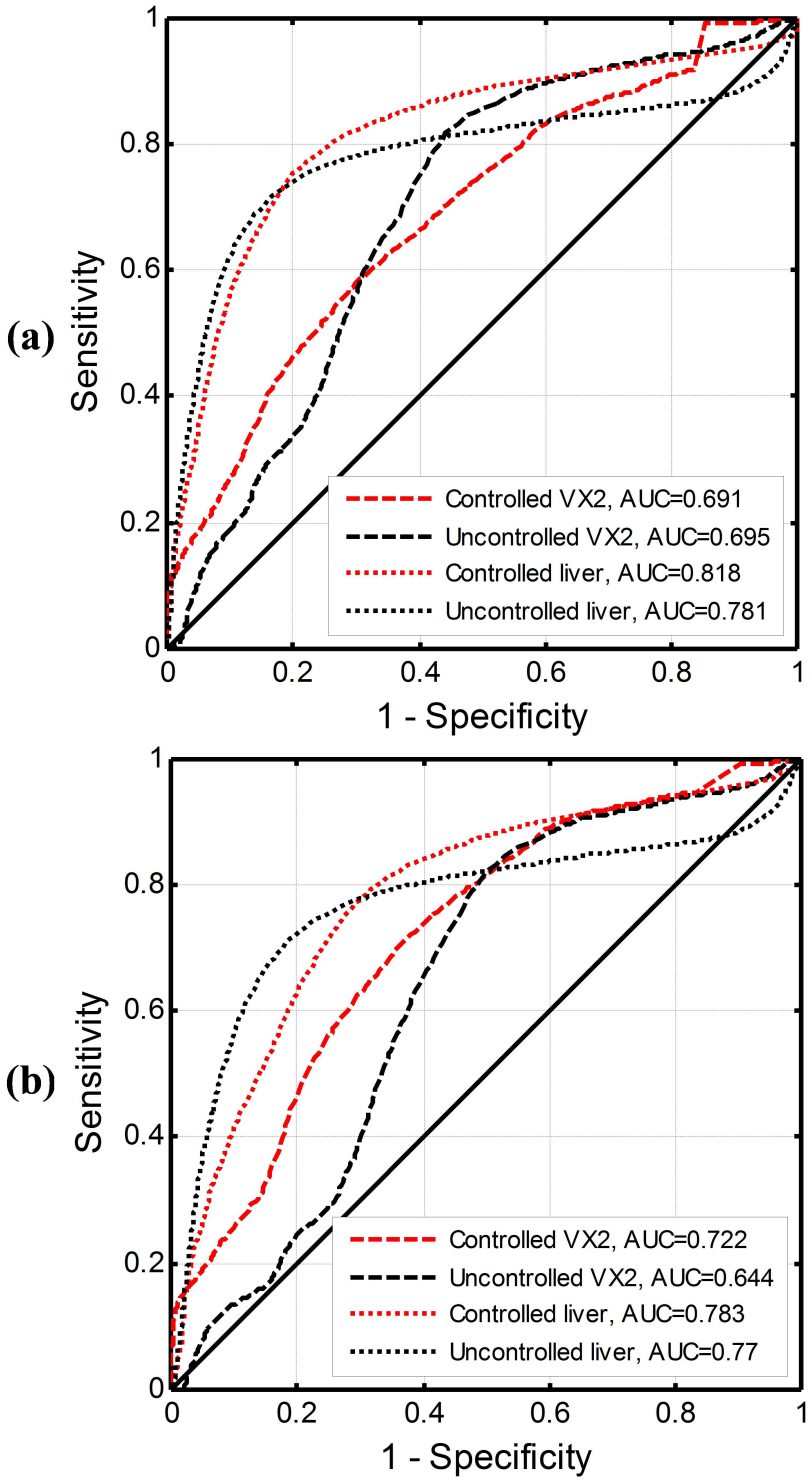

Figure 4.20: Receiver operating characteristic curves for integrated backscatter prediction of (a) treatment and (b) ablation in rabbit liver and VX2 tumor for the controlled and uncontrolled of all exposures combined.

Table 4.7: Results of paired, one-tailed z tests comparing AUC values for IBS prediction of treated and ablated regions in liver and VX2 tumor vs. chance (AUC = 0.5) (z-statistic (p value)).

	Liver		VX2 tumor	
HIFU	Treated	Ablated	Treated	Ablated
Controlled	7.1 ($5.45 \cdot 10^{-13}$)	5.7 ($4.88 \cdot 10^{-9}$)	2.7 (0.004)	1.4 (0.077)
Uncontrolled	3.8 ($6.29 \cdot 10^{-5}$)	2.9 ($2.1 \cdot 10^{-3}$)	1.9 (0.030)	1.3 (0.096)
Bulk				
Controlled	2.5 (0.006)	2.2 (0.016)	1.2 (0.113)	4.7 ($1.65 \cdot 10^{-6}$)
Uncontrolled	2.8 ($2.3 \cdot 10^{-3}$)	4.0 ($3.15 \cdot 10^{-5}$)	1.3 (0.096)	−0.003 (0.5)
All exposures				
Controlled	14.6 ($< 10^{-16}$)	9.9 ($< 10^{-16}$)	3.6 ($1.5 \cdot 10^{-4}$)	4.5 ($3.42 \cdot 10^{-6}$)
Uncontrolled	16.4 ($< 10^{-16}$)	14.9 ($< 10^{-16}$)	3.4 ($3.0 \cdot 10^{-4}$)	2.9 (0.011)

Table 4.8: Results of two-tailed z tests comparing AUC values for the controlled and uncontrolled trials for IBS prediction of treated and ablated regions in liver and VX2 tumor (z-statistic (p value)).

	Controlled vs. uncontrolled			
Tissue	Liver		VX2 tumor	
Exposure	Treated	Ablated	Treated	Ablated
HIFU	1.83 (0.066)	1.78 (0.075)	0.31 (0.756)	0.20 (0.845)
Bulk	−0.33 (0.739)	−0.98 (0.327)	0.50 (0.615)	2.29 (0.022)
All	1.35 (0.176)	0.37 (0.713)	−0.05 (0.964)	0.97 (0.332)

better than rabbit liver. For all controlled exposures combined, rabbit liver treatment was predicted significantly better than VX2 tumor.

Optimum integrated backscatter thresholds for local ablation prediction in rabbit liver and VX2 tumor determined from the computed ROC curves for both groups and their corresponding sensitivities and specificities are shown in Table 4.10. Tables 4.11 and 4.12 summarize statistical results of AUC comparisons between echo decorrelation and IBS prediction of local treatment and ablation in rabbit liver and VX2 tumor for both controlled and uncontrolled groups. In most cases, echo decorrelation and IBS imaging predicted treated

Table 4.9: Results of two-tailed z tests comparing AUC values for IBS prediction of treatment and ablation in VX2 tumor and liver for the controlled and uncontrolled trials (z-statistic (p value)).

	VX2 tumor vs. liver			
Groups	Controlled		Uncontrolled	
Exposure	Treated	Ablated	Treated	Ablated
HIFU	−1.38 (0.166)	−1.30 (0.192)	−0.32 (0.750)	−0.38 (0.703)
Bulk	0.79 (0.430)	2.7 ($6.7 \cdot 10^{-3}$)	0.30 (0.763)	−1.2 (0.223)
All	−2.21 (0.027)	−1.06 (0.287)	−1.45 (0.148)	−1.91 (0.055)

and ablated liver and VX2 tumor with statistically equivalent capability for controlled and uncontrolled trials. For all controlled trials combined, IBS prediction for local treatment in VX2 tumor was significantly better than echo decorrelation. For uncontrolled HIFU trials, echo decorrelation predicted treated and ablated liver significantly better than IBS.

Table 4.10: Optimal thresholds for local ablation prediction and corresponding sensitivities and specificities for IBS (decibel-scaled) in rabbit liver and VX2 tumor for the controlled and uncontrolled trials.

	Liver		VX2 tumor	
HIFU	Controlled	Uncontrolled	Controlled	Uncontrolled
Threshold	3.3	2.2	6.6	3.6
Sensitivity (%)	86.6	66.3	70.7	70.7
Specificity (%)	86.4	87.9	59.8	63.2
Bulk				
Threshold	7.2	4.0	6.3	3.5
Sensitivity (%)	51.3	60.3	71.9	66.8
Specificity (%)	60.5	67.1	74.1	39.4
All exposures				
Threshold	3.0	1.8	6.7	2.9
Sensitivity (%)	76.2	72.8	70.3	74.5
Specificity (%)	71.8	79.7	64	54.9

Means and standard errors of the decibel-scaled IBS in ablated and unablated rabbit liver and VX2 tumor are shown in Fig. 4.21(a)–(c) and Fig. 4.22(a)–(c) respectively. Statistical analyses of differences in mean decibel-scaled cumulative IBS in treated vs. non-treated, as well as in ablated vs. non-ablated rabbit liver and VX2 tumor for both controlled and uncontrolled groups are shown in Table 4.13. For HIFU exposures, both controlled and uncontrolled trials had significantly greater mean dB-scaled IBS in ablated than non-ablated rabbit liver. For bulk US exposures, controlled trials had significantly greater mean dB-scaled IBS in ablated than non-ablated VX2 tumor. For all exposures combined, both controlled and uncontrolled trials had significantly greater mean dB-scaled IBS in ablated than non-ablated rabbit liver and VX2 tumor.

Statistics of average cumulative IBS (dB) comparisons between controlled vs. uncontrolled groups in treated and ablated regions of rabbit liver or VX2 tumor, and also between VX2 tumor vs. rabbit liver in treated and ablated regions for the controlled and uncontrolled groups are shown in Table 4.14. There were no significant differences between mean cumulative IBS for controlled vs. uncontrolled trials in treated or ablated tissue. In most cases, there were no significant differences between mean cumulative IBS in VX2 tumor vs. liver for the controlled and uncontrolled groups in treated or ablated tissue, except that for controlled HIFU trials, ablated liver had significantly larger mean cumulative IBS than ablated VX2 tumor.

Optimal echo decorrelation and IBS thresholds for local ablation prediction in rabbit liver and VX2 tumor, computed from the ROC curves for all exposures combined for both controlled and uncontrolled trials ($N = 43$), were -2.9 ($\log_{10}$-scaled decorrelation per ms) for echo decorrelation and 2.3 dB for IBS. For echo decorrelation imaging, RMSE and NRMSE between measured ablated areas and areas predicted using these thresholds were 0.50 cm^2 (65.3%) for all controlled trials combined and 0.54 cm^2 (41.1%) for all uncontrolled trials

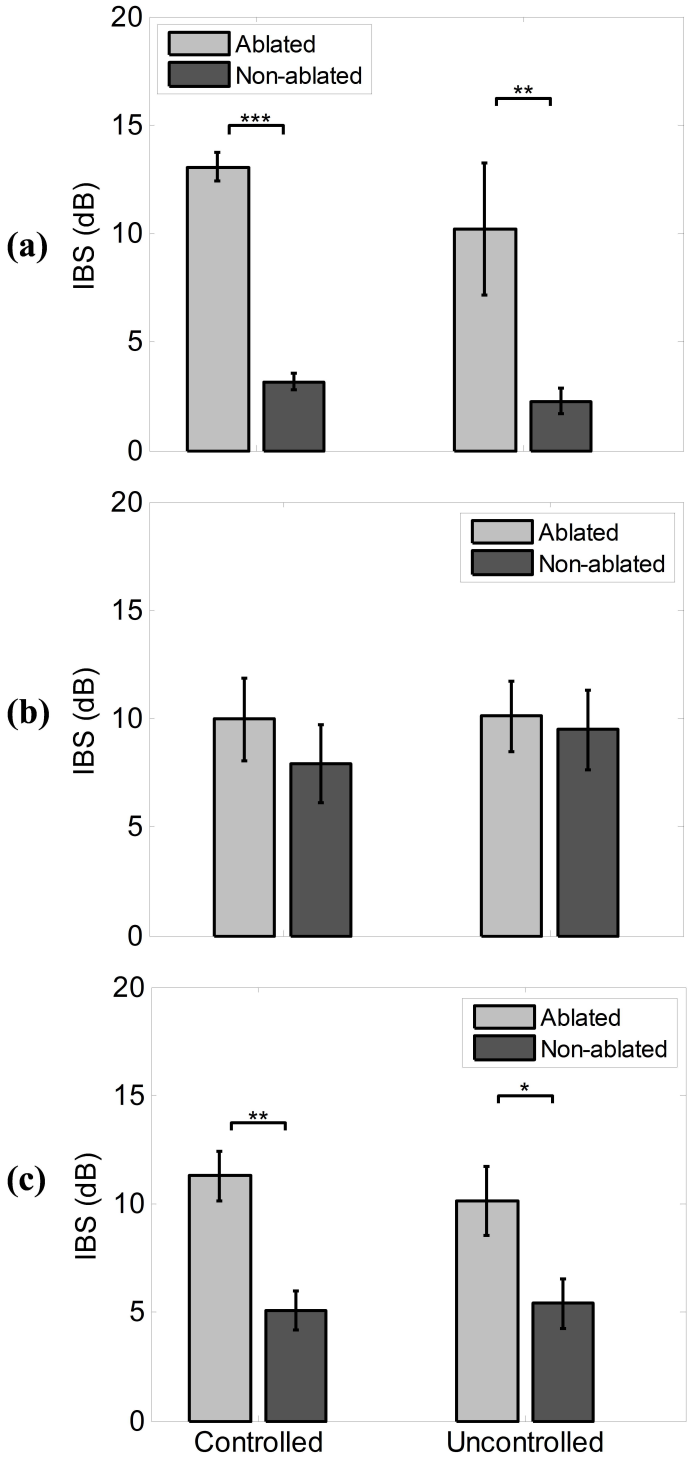

Figure 4.21: Means and standard errors of the decibel-scaled integrated backscatter in ablated and non-ablated rabbit liver for controlled vs. uncontrolled (a) HIFU, (b) bulk US, and (c) all exposures combined. ($* \; p < 0.05$, $** \; p < 10^{-2}$, and $*** \; p < 10^{-3}$)

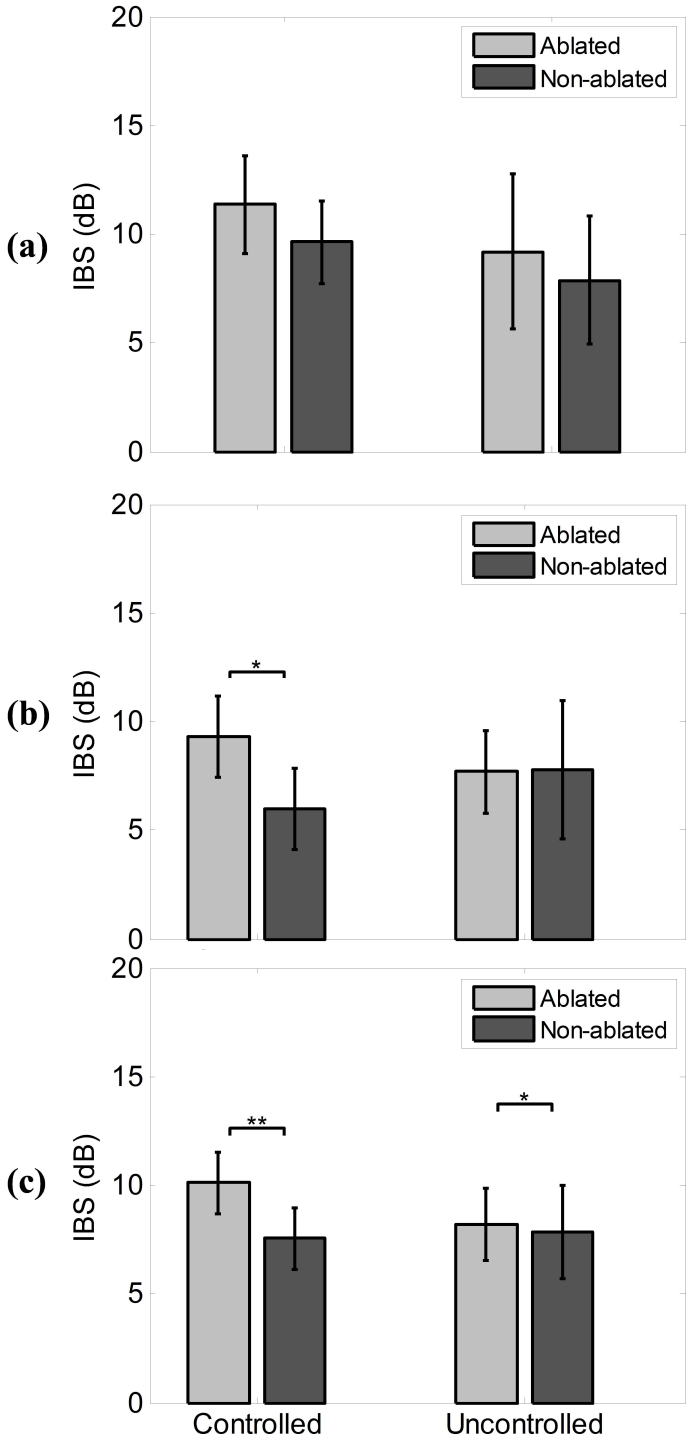

Figure 4.22: Means and standard errors of the decibel-scaled integrated backscatter in ablated and non-ablated VX2 tumor for controlled vs. uncontrolled (a) HIFU, (b) bulk US, and (c) all exposures combined. ($* \; p < 0.05$, $** \; p < 10^{-2}$, and $*** \; p < 10^{-3}$)

combined. For IBS imaging, RMSE and NRMSE were 0.485 cm^2 (63.3%) for all controlled trials combined and 0.538 cm^2 (40.8%) for all uncontrolled trials combined.

Similarly, based on the ROC curve for all exposures combined for both controlled and uncontrolled trials, optimal echo decorrelation and IBS thresholds for local treatment prediction in rabbit liver and VX2 tumor were -2.9 ($\log_{10}$-scaled decorrelation per ms) for echo decorrelation and 1.8 dB for IBS. For echo decorrelation imaging, RMSE and NRMSE between measured treated areas and areas predicted using these thresholds were 0.53 cm^2 (47.7%) for all controlled trials combined and 0.70 cm^2 (45.9%) for all uncontrolled trials combined. For IBS imaging, RMSE and NRMSE were 0.42 cm^2 (38.1%) for all controlled trials combined and 0.71 cm^2 (46.7%) for all uncontrolled trials combined.

Table 4.11: Results of two-tailed z test comparisons between AUC values for echo decorrelation and IBS ablation prediction of treated and ablated regions in liver and VX2 tumor for controlled trials (z-statistic (p value)).

	Echo decorrelation vs. IBS imaging			
Tissue	Liver		VX2 tumor	
Exposure	Treated	Ablated	Treated	Ablated
HIFU	−0.94 (0.346)	−0.21 (0.834)	−0.22 (0.824)	−0.579 (0.563)
Bulk	0.65 (0.515)	0.023 (0.982)	−0.09 (0.932)	−0.57 (0.566)
All	−1.20 (0.230)	−1.04 (0.30)	−2.16 (0.031)	−1.81 (0.071)

Table 4.12: Results of two-tailed z test comparisons between AUC values for echo decorrelation and IBS ablation prediction of treated and ablated regions in liver and VX2 tumor for uncontrolled trials (z-statistic (p value)).

	Echo decorrelation vs. IBS imaging			
Tissue	Liver		VX2 tumor	
Exposure	Treated	Ablated	Treated	Ablated
HIFU	2.28 (0.022)	2.08 (0.037)	−0.22 (0.820)	0.23 (0.829)
Bulk	0.50 (0.620)	−0.02 (0.982)	0.53 (0.599)	1.18 (0.237)
All	1.64 (0.101)	1.59 (0.112)	−0.74 (0.453)	0.39 (0.693)

Table 4.13: Results of paired, one-tailed t-tests comparing mean dB-scaled IBS in treated and non-treated, ablated and non-ablated regions in liver and VX2 tumor (t-statistic (p value,N)).

	Treated vs. non-treated		Ablated vs. non-ablated	
HIFU	Liver	VX2	Liver	VX2
Controlled	7.0 ($5.9 \cdot 10^{-5}$, 9)	4.4 ($3.4 \cdot 10^{-3}$, 6)	20.3 ($2.6 \cdot 10^{-6}$, 6)	1.1 (0.163, 5)
Uncontrolled	3.5 ($5.9 \cdot 10^{-5}$, 8)	1.9 (0.057, 6)	3.5 ($4.7 \cdot 10^{-3}$, 8)	1.2 (0.149, 4)
Bulk				
Controlled	1.5 (0.095, 7)	5.3 (0.059, 2)	1.2 (0.136, 8)	2.9 (0.011, 8)
Uncontrolled	1.4 (0.096, 9)	1.0 (0.251, 2)	0.4 (0.353, 10)	2.3 (0.075, 3)
All exposures				
Controlled	4.7 ($1.4 \cdot 10^{-4}$, 16)	5.5 ($4.7 \cdot 10^{-4}$, 8)	5.1 ($4.3 \cdot 10^{-5}$, 14)	2.8 (0.008, 13)
Uncontrolled	3.3 ($2.2 \cdot 10^{-3}$, 17)	2.3 (0.03, 8)	2.5 (0.012, 18)	2.2 (0.036, 7)

Table 4.14: Results of unpaired, two-tailed t-tests comparing mean cumulative dB-scaled IBS for controlled vs. uncontrolled groups and VX2 tumor vs. liver in treated and ablated regions (t-statistic (p value)).

	Controlled vs. uncontrolled		VX2 tumor vs. liver	
HIFU	Liver	VX2	Controlled	Uncontrolled
Treated	0.31 (0.761)	0.79 (0.449)	1.09 (0.297)	0.05 (0.963)
Ablated	0.80 (0.440)	0.54 (0.606)	−0.79 (0.448)	−0.19 (0.848)
Bulk				
Treated	−0.02 (0.988)	0.52 (0.615)	−0.53 (0.607)	−1.15 (0.267)
Ablated	0.35 (0.733)	−0.57 (0.623)	−0.25 (0.810)	−0.97 (0.347)
All exposures				
Treated	0.23 (0.817)	0.93 (0.360)	0.12 (0.915)	−0.64 (0.530)
Ablated	0.50 (0.617)	0.14 (0.449)	−0.66 (0.517)	−0.83 (0.420)

4.4 Discussion

In this chapter, the feasibility of controlling HIFU and bulk US thermal ablation using echo decorrelation imaging feedback was demonstrated in *in vivo* rabbit liver and VX2 tumor. The proposed real-time control algorithm was able to cease all successfully controlled HIFU

and bulk US treatments (i.e., all exposures except two bulk US treatments ending early due to software errors) when Δ_{avg} exceeded the predefined Δ_{th} ($\log_{10}$-scaled decorrelation per ms: -2.3). Tissue treatment was confirmed by TTC vital staining for all successfully controlled HIFU and bulk US trials. For both HIFU and bulk US ablation, controlled trials showed smaller lesion width and area, higher ablation rate, and significantly lower treatment time than uncontrolled trials, with equivalent prediction capability. Possible improvements to echo decorrelation imaging feedback for controlling future preclinical or clinical experiments are discussed below.

Average-decorrelation control criteria (control threshold and ROI shape/size) were effective for controlling the HIFU and bulk US treatments reported here. However, further investigation is required for better control performance in future *in vivo* studies. The control threshold ($\log_{10}$-scaled decorrelation per ms: -2.3) used here was selected from a similar *in vivo* study reported by Fosnight et al. [33], which computed echo decorrelation maps by ensemble averaging more RF frames (114 frames) than used here (20 frames). This difference in number of frames affected the computed cumulative echo decorrelation values and corresponding ablation prediction sensitivities and specificities. Retrospective analysis of uncontrolled trials indicated that for 20 frames, echo decorrelation thresholds corresponding to 90% specificity for local ablation prediction in liver and VX2 tumor for all exposures combined would be -2.3 and -1.6 ($\log_{10}$-scaled decorrelation per ms) respectively. In that case, an appropriate control threshold would be -1.6 ($\log_{10}$-scaled decorrelation per ms) instead of -2.3 ($\log_{10}$-scaled decorrelation per ms) as used here for controlled HIFU and bulk US experiments. Such an increase in the control threshold value is expected to improve local ablation prediction of bulk US thermal lesioning in both liver and tumor tissue, because for US ablation of rabbit liver and VX2 tumor, this larger threshold should confirm ablation of both tissue types. For controlled HIFU trials, using a larger control threshold would likely

improve the relatively poor prediction capability of echo decorrelation for tumor thermal ablation observed here (AUC = 0.668, $p = 0.139$).

Regarding the control ROI shape and size, for controlled HIFU experiments the use of a small control ROI (1×1 mm^2) at the focal zone helped in mitigating the effect of substantial echo decorrelation artifacts, observed outside the focal zone for some HIFU trials (Figs. 4.4(D), 4.5(E, G, H), and 4.6(J)), on the control algorithm. For controlled bulk US experiments, the use of a control ROI (18 mm $\times$ 6 mm) that approximately matched the shape and size of bulk thermal lesions in rabbit liver helped in confirming the expansion of thermal lesioning beyond that ROI boundaries in 87.5% of the successfully controlled trials. These results are consistent with previous *ex vivo* controlled bulk US ablation experiments employing similar stopping criteria in bovine liver (Section 3.3.2) [119].

In the experiments reported here, the motion and noise compensation method previously derived by Hooi et al. [70] was implemented in real-time to work simultaneously with echo decorrelation imaging. The correction method improved the capability of echo decorrelation imaging for local ablation prediction in rabbit liver and VX2 tumor as reported by Fosnight et al. [33]. However, the compensation method did not significantly affect the control algorithm performance. That is, without applying the compensation method, treatments would have stopped at the same therapy cycle. This may have occurred because the control ROIs for HIFU and bulk US experiments were accurately located at the region where large echo decorrelation occurred due to thermal ablation. Another possibility is that the correction method could not compensate additional artifactual echo decorrelation occurring during therapy cycles (e.g., that due to acoustic radiation force), in which case Δ_{avg} values would be nearly the same for corrected vs. uncorrected cumulative echo decorrelation maps. Fig. 4.5(G) shows an example of substantial echo decorrelation artifacts, possibly due to the effect of acoustic radiation force on trapped fluid inside the necrotic core of a large VX2 tumor. The compensation method could be modified to account for the effect of acoustic radiation

force by including image data from the first one or two therapy cycles within the cumulative sham echo decorrelation map.

Controlled HIFU trials ($N = 6$) treating liver only had significantly smaller lesion width ($p < 0.01$), depth ($p = 0.010$), and area ($p = 0.022$) than corresponding uncontrolled HIFU trials ($N = 7$). These results are consistent with previous controlled HIFU experiments that employed similar control criteria in *ex vivo* bovine liver (Chapter 2) [118], possibly because the selected control threshold was equivalent to that used in the *ex vivo* study (i.e., corresponding to 90% specificity for local ablation prediction in preliminary experiments). However, controlled HIFU trials ($N = 3$) treating tumor only had larger but statistically equivalent lesion width ($p = 0.850$), depth ($p = 0.141$), and area ($p = 0.513$) compared to corresponding uncontrolled HIFU trials ($N = 5$), contrary to the trend for HIFU trials treating liver only. Further investigation with a larger number of trials would be required to confirm and analyze this possible trend.

Thermal lesion dimensions for controlled HIFU trials treating liver only were slightly smaller but statistically equivalent compared to controlled trials treating tumor only. However, thermal lesion dimensions for uncontrolled HIFU trials treating liver only were significantly larger than uncontrolled trials treating tumor only. These results suggest that controlling HIFU thermal ablation in liver and tumor using the same control threshold could provide equivalent ablation outcomes in both tissue types. However, more trials would be required to confirm this trend statistically.

Controlled bulk US trials had slightly smaller and more consistent treated area (2.04 ± 0.24 vs. 2.54 ± 0.26) than uncontrolled bulk US trials. This may have occurred because the control algorithm stopped bulk sonications before or immediately after tissue vaporization temperatures (> 100 °C), preventing excessive treatment of the tissue.

Echo decorrelation prediction of treatment and ablation in liver and VX2 tumor for controlled HIFU and bulk US trials was significantly better than chance, except for prediction

of tumor ablation in controlled HIFU trials and prediction of tumor treatment in controlled bulk US trials. Echo decorrelation prediction of tumor treatment in controlled HIFU trials and tumor ablation in bulk US trials was statistically equivalent to the corresponding uncontrolled trials (Figs. 4.13–4.15). Echo decorrelation predicted treated liver significantly better than treated VX2 tumor for HIFU and bulk exposures combined ($p < 0.01$), consistent with the choice of the control threshold as discussed above. However, echo decorrelation predicted ablated tumor significantly better than ablated liver for controlled bulk US trials ($p = 0.037$). This opposite trend may be associated with the low prevalence of unablated tumor points in the segmented histology maps for bulk US trials.

Integrated backscatter prediction of treatment and ablation in liver and VX2 tumor for controlled HIFU and bulk US trials showed similar trends compared to echo decorrelation imaging with higher AUC values in some cases, but with no significant differences (Table 4.11). Similar behavior was observed in previous *ex vivo* controlled HIFU experiments (Chapter 2). However, in previous uncontrolled RFA [89, 92] and US [88] thermal ablation studies, echo decorrelation predicted local thermal ablation better than IBS, consistent with prediction results from controlled and uncontrolled bulk US experiments in *ex vivo* bovine liver previously reported in Chapter 3. Possible reasons for this discrepancy are that for controlled trials, treatments stopped when high decorrelation due to thermal coagulation occurred, usually accompanied by hyperechoic activity (higher echo signal energy). However, for uncontrolled trials, formation of microbubbles due to excessive tissue heating can cause acoustic shadowing, which decreases echo signal energy in the shadowed region and thus can lead to poor prediction by integrated backscatter [89].

4.5 Conclusion

In this chapter, HIFU and bulk US thermal ablation were successfully controlled using real-time echo decorrelation imaging feedback in *in vivo* rabbit liver and VX2 tumor tissue. Echo decorrelation imaging feedback was corrected for motion and noise in real-time. Controlled trials showed smaller lesion area, significantly less treatment time, and higher ablation rate than uncontrolled trials, with equivalent prediction capability. Also, controlled HIFU trials treating rabbit liver only showed significantly smaller lesion dimensions, higher ablation rate, and less treatment time than corresponding uncontrolled HIFU trials. The results reported here indicate that controlling US thermal ablation using echo decorrelation imaging feedback may reduce treatment time and increase treatment reliability for *in vivo* thermal ablation.

Chapter 5
Conclusions and Future Work

5.1 Summary

The main purpose of this dissertation was to develop a real-time closed loop control approach to control high-intensity focused and unfocused ultrasound thermal ablation using echo decorrelation imaging feedback *ex vivo* and *in vivo*. This control approach was hypothesized to provide precise thermal lesions, mitigate tissue overtreatment, improve local ablation prediction, and reduce the overall treatment duration. Summarized findings and conclusions for each chapter are discussed below.

In Chapter 2, a real-time echo decorrelation imaging feedback control algorithm was developed to control high-intensity focused ultrasound (HIFU) in *ex vivo* bovine liver. This control algorithm employed a small control region of interest (ROI) (1×1 mm^2) located at the HIFU focal zone and a control threshold (Δ_{th}) corresponding to 90% specificity of local ablation prediction in *ex vivo* bovine liver. Using this control algorithm, 100% of the controlled treatments were successfully stopped when minimum cumulative ensemble-averaged decorrelation Δ_{min} inside the control ROI exceeded Δ_{th} ($\log_{10}$-scaled echo decorrelation per ms). Ablation outcomes and prediction capability for the controlled group were compared to uncontrolled groups employing the two, five, and nine therapy cycles. Ablation prediction using echo decorrelation in the controlled group was significantly better than in the 2-cycle

group and statistically equivalent to the 5-cycle and 9-cycle uncontrolled groups. Lesion width and area for controlled trials was significantly smaller than 5-cycle and 9-cycle uncontrolled trials but statistically equivalent to 2-cycle trials. The mean duration of controlled exposures was 5.8 s, equal to the 2-cycle group but significantly smaller than the 5-cycle or 9-cycle groups. These results showed that echo decorrelation imaging is feasible to control HIFU thermal ablation in *ex vivo* bovine liver.

In Chapter 3, the feedback control algorithm implemented in Chapter 2 was extended to control unfocused (bulk) ultrasound (US) thermal ablation *in ex vivo* bovine liver. An optimization method was proposed to determine ablation control thresholds and ROI dimensions for two series of controlled experiments using different echo decorrelation imaging feedback parameters (minimum-decorrelation vs. average-decorrelation criterion) and different sonication sequences (constant-intensity vs. variable-intensity sonication sequence). Using preliminary experiments, control ROIs and thresholds for the minimum-decorrelation (16 mm $\times$ 12 mm, $\Delta_{\text{th}} = -3.20$ $\log_{10}$-decorrelation per ms) and average-decorrelation (12 mm $\times$ 9 mm, $\Delta_{\text{th}} = -1.576$) criteria were optimized. Controlled trials for the minimum-decorrelation and average-decorrelation criteria were compared with uncontrolled trials employing 9 or 18 cycles of matching sonication sequences. Successfully controlled trials using both criteria required significantly less treatment time than corresponding 18-cycle treatments, with better ablation prediction performance and higher ablation rate than corresponding 9-cycle or 18-cycle uncontrolled approaches. A *post hoc* analysis studied the effect of exchanging control criteria between the two series of controlled experiments. For either group, the average time needed to exceed the alternative decorrelation threshold approximately matched the average duration of successfully controlled experimental trials. These results indicate that either approach, using minimum-decorrelation or average-decorrelation

criteria, is feasible for control of bulk US ablation. In addition, use of a variable-intensity sonication sequence for bulk US thermal ablation can result in larger ablated regions compared to constant-intensity sonication sequences.

Based upon the success of controlling *ex vivo* HIFU and bulk US treatments in Chapters 2 and 3, in Chapter 4 the control algorithm was modified and applied to control *in vivo* ablation of rabbit liver and VX2 tumor. Echo decorrelation imaging feedback was corrected for motion and noise in real-time using the compensation method previously derived by Hooi et al. [70]. Based on results of a similar *in vivo* study [33], the control threshold was chosen as -2.3 ($\log_{10}$-scaled echo decorrelation per ms), corresponding to 90% specificity of local ablation prediction for *in vivo* VX2 tumor. The control ROI dimensions were modified based on *in vivo* lesion shapes to be 18 mm $\times$ 6 mm. Ablation outcomes and prediction capability of echo decorrelation imaging for controlled trials were compared with a similar series of uncontrolled *in vivo* experiments employing HIFU and bulk US ablation in rabbit liver and VX2 tumor [33]. Controlled trials showed smaller lesion area, significantly less treatment time, and higher ablation rate than uncontrolled trials, with equivalent prediction capability. Also, controlled HIFU trials treating rabbit liver only showed significantly smaller lesion dimensions, higher ablation rate, and less treatment time than corresponding uncontrolled HIFU trials. The results reported indicate that controlling US thermal ablation using echo decorrelation imaging feedback may reduce treatment time and increase treatment reliability for *in vivo* thermal ablation.

Echo decorrelation imaging showed better prediction and control performances for *ex vivo* US thermal ablation (Chapter 2 and 3) compared to *in vivo* US thermal ablation (Chapter 4). Reasons for this inconsistency may include differences in acoustical and anatomical properties between *ex vivo* (bovine liver) and *in vivo* (rabbit liver with VX2 tumor) tissue. Differences between *in vivo* and *ex vivo* ablation also include heat-sink effects due to blood perfusion and tissue motion. Errors in assessing prediction likely also occurred due to issues

with post-treatment tissue handling, including sectioning, staining, and scanning. For *ex vivo* tissue, using a cubic cuvette ensured approximately parallel and flat tissue surfaces, resulting in better transducer alignment and better image registration between echo decorrelation maps and treated regions compared to *in vivo* tissue. For *in vivo* tissue, uneven surfaces, particularly for regions with tumors, led to inaccurate transducer alignment, difficulties in determining the imaging/treatment plane, and consequently inaccurate tissue sectioning. Also, in trials with VX2 tumor, pre-existing necrosis and inhomogeneous vital stain uptake led to uncertainty in differentiating ablated, treated, and untreated regions.

In this dissertation, the central hypothesis, that using echo decorrelation imaging feedback for controlling US thermal ablation provides precise thermal lesioning with smaller treatment time and better cell death prediction than uncontrolled US ablation, was confirmed for controlling HIFU and bulk US thermal ablation in *ex vivo* (Chapter 2 and 3) and *in vivo* (Chapter 4) experiments. In general, controlled trials showed smaller lesion dimensions, smaller treatment time, and higher ablation rate compared to uncontrolled trials with longer duration, designed to ensure complete ablation (e.g., 5-cycle and 9-cycle focused trials in Chapter 2, 18-cycle bulk US trials in Chapter 3, and all uncontrolled trials in Chapter 4). However, controlled trials generally showed equivalent lesion dimensions and treatment time, but higher ablation rate compared to uncontrolled trials with shorter duration (e.g., 2-cycle focused trials in Chapter 2 and 9-cycle bulk US trials in Chapter 3). Better echo decorrelation prediction capability was observed for controlled trials compared to uncontrolled trials with shorter duration, but equivalent prediction performance was observed when compared to uncontrolled trials with longer exposures. For most cases, integrated backscatter imaging showed similar behavior to echo decorrelation imaging for local ablation prediction for controlled trials.

Controlled *ex vivo* and *in vivo* trials generally showed equivalent precision, assessed by comparing variances of lesion dimensions, compared to uncontrolled trials with shorter or

longer duration. This result does not support the hypothesis that controlling US thermal ablation provides more precise thermal lesioning than uncontrolled ablation. Since lesion shape and size highly depend on the amount of deposited heat and treatment time [131], a substantial change in the progress of lesion formation can occur at temperatures > 100 °C [132], due to tissue vaporization. The control algorithm proposed here exploited heat-induced echo decorrelation feedback to stop treatments, likely at temperatures higher than 80°C. However, abrupt jumps in echo decorrelation values between successive therapy cycles may lead to treatment cessation after exceeding the boiling temperature in some cases. For the bulk US ablation approach employed in Chapter 3, treatments may continue as long as 6 s after vaporization. Precision could be improved by tracking echo decorrelation activity between shorter, consecutive therapy pulses. Using this approach, cumulative decorrelation inside the control ROI could potentially cease treatments before extensive tissue boiling.

5.2 Future Directions

Clinical translation of the proposed real-time feedback control algorithm is feasible for controlling HIFU and bulk US thermal ablation, given necessary additional investigations. Optimal echo decorrelation thresholds for control should be determined for different tumor types (e.g., hepatocellular carcinoma (HCC) and colorectal metastases (CLM)) and liver parenchyma states (e.g., cirrhotic or fatty liver), each of which has different acoustic and thermal properties. Uncontrolled preliminary clinical experiments are needed to determine these optimal thresholds before testing of echo decorrelation-controlled ablation in patients. These experiments could determine control thresholds similarly to the procedure employed in Chapter 2, with ROC curves computed by point-by-point comparison of cumulative echo decorrelation maps with ablation results from radiologic imaging or histology. Echo decorrelation thresholds could then be chosen to achieve the required specificity and sensitivity of ablation prediction in each tissue type.

HIFU ablation control using echo decorrelation imaging as demonstrated in Chapter 2, could be incorporated into commercial extracorporeal US guided HIFU systems used for treating unresectable liver tumors (e.g., Model JC, Chongqing HAIFU Tech Ltd, China). In the Model-JC HAIFU system [133], sections of the targeted treatment volume are ablated sequentially with monitoring by 2D B-mode imaging. Using a single-exposure mode [134], repeated HIFU sonications $>$ 1 s duration at each position are employed. After ablation, treatment end points are assessed visually by comparing pretreatment and post-treatment B-mode US images of the treated area. Using the same workflow, 2D echo decorrelation maps could be computed using the RF echo signals acquired after HIFU sonication in each slice. To implement ablation control, treatments would stop once the echo decorrelation exceeded an ablation threshold within an ROI for the current focal position. The system would then proceed to the next focal position and repeat this procedure to ablate the entire targeted volume. This control approach could improve ablation accuracy while reducing treatment times, since only the necessary number of HIFU sonication cycles would be fired at each position.

The control methods investigated in Chapter 3 were optimized for bulk ultrasound ablation, but could also be optimized for controlling clinical thermal ablation techniques (e.g. radiofrequency ablation (RFA) and microwave ablation (MWA)) with minor changes. Since bulk thermal ablation using RFA or MWA is inherently a 3D problem, 3D imaging and controlling methods are needed for better ablation assessment and control [73, 135]. The feasibility of 3D echo decorrelation imaging has been shown previously [70]. For ablation control using 3D echo decorrelation imaging, the target volume could be subdivided into multiple control ROIs, accounting for likely spatial variations in ablation rates caused by differences in local anatomy (e.g., local tissue type, large blood vessels, and tissue boundaries). Treatments would then continue until the average or minimum echo decorrelation

within all control ROIs exceeds a prespecified control threshold. The optimum size, geometry, and number of ROIs as well as optimal control thresholds could be selected similarly to the approach employed in Chapter 3 for unfocused ultrasound ablation, based on 3D echo decorrelation volumes acquired and archived during clinical RFA and MWA procedures. The same process could then be repeated for different thermal ablation techniques and tumor types. Treatment near vulnerable structures could potentially be performed safely by confining vulnerable areas to a safety ROI, ceasing treatment after a lower decorrelation threshold has been met within that ROI [118].

Future survival studies in animals with implanted tumors [136] could be done to assess long-term ablation outcomes for controlled US experiments using echo decorrelation imaging feedback. Materials and methods used in Chapter 4 could be employed in these studies with some changes. VX2 tumor would be implanted in a series of rabbits and after two weeks, 50% of the rabbits would be thermally treated in a sterile open surgery or noninvasive procedure. The untreated animals would be considered a control group. Follow-up for all animals would be performed using computed tomography or US monitoring for 2 months or until animal death. Survival analysis for the control and treatment groups would be done using the Kaplan-Meier method [137]. This study would provide new information on the effectiveness of controlled US ablation using echo decorrelation imaging feedback in improving long-term survival for rabbits with VX2 tumor.

Further preliminary studies are required to facilitate future clinical translation of echo decorrelation imaging to monitor and control thermal ablation of liver tumors. Possible studies are outlined as follows: (1) echo decorrelation imaging for thermal ablation in *ex vivo* human liver, to test the feasibility of echo decorrelation for local ablation prediction and to compute receiver operating characteristic curves to determine control thresholds for different tissue types as described in Section 2.2.3, (2) treat-and-resect experiments on patients undergoing resectable liver tumor surgery, to test the feasibility of echo decorrelation

imaging for local ablation prediction in *in vivo* human liver and also to determine control thresholds as for the *ex vivo* experiments, (3) post-treatment disease-free survival rate studies [138]. In these experiments, tumor would be ablated with control by echo decorrelation imaging feedback and after ablation at intervals of 1–3 months, ablation success would be evaluated by computed tomography or magnetic resonance imaging and tumor biomarkers (α-fetoprotein for HCC [11] and carcinoembryonic antigen for CLM [138]). Controlled trials would be compared to uncontrolled trials with longer duration. The disease-free interval would be defined as the interval between ablation and tumor recurrence. Overall survival time would be defined as the interval between the ablation procedure and death. Treatment time and overall survival time for the controlled and uncontrolled groups would be statistically tested. Following this strategy should ultimately demonstrate the efficiency and accuracy of thermal ablation control by echo decorrelation imaging for clinical applications.

Appendix

Details of *in vivo* controlled ablation experiments

Table A.1: Identification numbers of the rabbits, treatment time sequences, therapy cycles, measured acoustic powers, applied voltages, focal depths, and estimated spatial-peak temporal-peak acoustic intensities (I_{SPTP}) for controlled *in vivo* HIFU thermal ablation trials (gray-shaded rows represent trials excluded from the statistical analysis).

Trial #	Rabbit ID #	On time (s)	Off time (s)	Cycles	A.P. (W)	Voltage (V)	$\mathrm{F_{depth}}$ (mm)	Aperture	$\mathrm{P_{gain}}$	I_{SPTP} (W/cm^2)
Date: 5/10/2017	Array: THX5A JV910	f_c: 5.35 MHz								
1_{A}	R334 / Right lobe	0.7	2.2	3	24-28	10.5-11.7	25	1-64	7.43	1025-1195.8
1 (left mark)	R334 / Right lobe	6.0	2.2	10	35	13.8	∞	1-10	1.54	64.0
1 (right mark)	R334 / Right lobe	6.0	2.2	10	35	13.8	∞	55-64	1.54	64.0
2_{B}	R334 / Middle lobe	0.7	2.2	4	24-28	10.5-11.7	25	1-64	7.43	1025-1195.8
Date: 6/14/2017	Array: THX5A JV910	f_c: 5.35 MHz								
3_{C}	R335 / Right lobe	0.7	2.2	5	24-28	10.7-11.9	25	1-64	7.43	1025-1195.8
3 (left mark)	R335 / Right lobe	6.0	2.2	8	35	14	∞	1-10	1.54	64.0
3 (right mark)	R335 / Right lobe	6.0	2.2	9	35	14	∞	55-64	1.54	64.0
4_{D}	R335 / Right lobe	0.7	2.2	6	24-28	10.7-11.9	25	1-64	7.43	1025-1195.8
4 (left mark)	R335 / Right lobe	6.0	2.2	9	35	14	∞	1-10	1.54	64.0
4 (right mark)	R335 / Right lobe	6.0	2.2	9	35	14	∞	55-64	1.54	64.0
	Array: THX5A JV933	f_c: 5.50 MHz								
5_{E}	R336 / Left lobe	0.7	2.2	3	24-28	11.3-12.4	25	1-64	7.42	1022-1192.4
5 (left mark)	R336 / Left lobe	6.0	2.2	9	35	14	∞	1-10	1.54	63.9
5 (right mark)	R336 / Left lobe	6.0	2.2	9	35	14	∞	55-64	1.54	63.9
Date: 10/11/2017	Array: THX5A JV910	f_c: 5.35 MHz								
6_{F}	R340 / Left lobe	0.7	2.2	2	24-28	11.2-12.5	25	1-64	7.43	1025-1195.8
6 (left mark)	R340 / Left lobe	6.0	2.2	5	35	13.9	∞	1-10	1.54	64.0
6 (right mark)	R340 / Left lobe	6.0	2.2	9	35	13.9	∞	55-64	1.54	64.0
7	R340 / Right lobe	0.7	2.2	2	24-28	11.2-12.5	25	1-64	7.43	1025-1195.8
7 (left mark)	R340 / Right lobe	6.0	2.2	5	35	13.9	∞	1-10	1.54	64.0
7 (right mark)	R340 / Right lobe	6.0	2.2	2	35	13.9	∞	55-64	1.54	64.0
8_{G}	R341 / Middle lobe	0.7	2.2	13	24-28	11.2-12.5	25	1-64	7.43	1025-1195.8
8 (left mark)	R341 / Middle lobe	6.0	2.2	9	35	13.9	∞	1-10	1.54	64.0
8 (right mark)	R341 / Middle lobe	6.0	2.2	9	35	13.9	∞	55-64	1.54	64.0

Table A.2: Identification numbers of rabbits, treatment time sequences, therapy cycles, measured acoustic powers, applied voltages, focal depths, and estimated spatial-peak temporal-peak acoustic intensities (I_{SPTP}) for controlled *in vivo* HIFU thermal ablation trials (gray-shaded rows represent trials excluded from the statistical analysis). (Continued)

Trial #	Rabbit ID #	On time (s)	Off time (s)	Cycles	A.P. (W)	Voltage (V)	$\mathrm{F_{depth}}$ (mm)	Aperture	$\mathrm{P_{gain}}$	I_{SPTP} (W/cm^2)
Date: 10/11/2017	Array: THX5A JV910	f_c: 5.35 MHz								
9_{H}	R341 / Right lobe	0.7	2.2	13	24-28	11.2-12.5	25	1-64	7.43	1025-1195.8
9 (left mark)	R341 / Right lobe	6.0	2.2	9	35	13.9	∞	1-10	1.54	64.0
9 (right mark)	R341 / Right lobe	6.0	2.2	9	35	13.9	∞	55-64	1.54	64.0
10_{I}	R341 / Right lobe	0.7	2.2	4	24-28	11.2-12.5	25	1-64	7.43	1025-1195.8
10 (left mark)	R341 / Right lobe	6.0	2.2	5	35	13.9	∞	1-10	1.54	64.0
10 (right mark)	R341 / Right lobe	6.0	2.2	9	35	13.9	∞	55-64	1.54	64.0
Date: 11/15/2017	Array: THX5A JV910	f_c: 5.35 MHz								
11_{J}	R342 / Right lobe	0.7	2.2	3	24-28	11.0-12.5	25	1-64	7.43	1025-1195.8
11 (left mark)	R342 / Right lobe	6.0	2.2	9	35	13.9	∞	1-10	1.54	64.0
11 (right mark)	R342 / Right lobe	6.0	2.2	3	35	13.9	∞	55-64	1.54	64.0
12	R343 / Middle lobe	0.7	2.2	1	24-28	11.0-12.5	25	1-64	7.43	1025-1195.8
12 (left mark)	R343 / Middle lobe	6.0	2.2	9	35	13.9	∞	1-10	1.54	64.0
12 (right mark)	R343 / Middle lobe	6.0	2.2	9	35	13.9	∞	55-64	1.54	64.0
13_{K}	R343 / Right lobe	0.7	2.2	2	24-28	11.0-12.5	25	1-64	7.43	1025-1195.8
13 (left mark)	R343 / Right lobe	6.0	2.2	5	35	13.9	∞	1-10	1.54	64.0
13 (right mark)	R343 / Right lobe	6.0	2.2	3	35	13.9	∞	55-64	1.54	64.0
14_{L}	R343 / Right lobe	0.7	2.2	1	24-28	11.0-12.5	25	1-64	7.43	1025-1195.8
14 (left mark)	R343 / Right lobe	6.0	2.2	5	35	13.9	∞	1-10	1.54	64.0
14 (right mark)	R343 / Right lobe	6.0	2.2	5	35	13.9	∞	55-64	1.54	64.0

Table A.3: Identification numbers of rabbits, treatment time sequences, therapy cycles, measured acoustic powers, applied voltages, focal depths, and estimated spatial-peak temporal-peak acoustic intensities (I_{SPTP}) for controlled *in vivo* unfocused ultrasound thermal ablation trials (gray-shaded rows represent trials excluded from the statistical analysis).

Trial #	Rabbit ID #	On time (s)	Off time (s)	Cycles	A.P. (W)	Voltage (V)	$\mathrm{F_{depth}}$ (mm)	Aperture	$\mathrm{P_{gain}}$	I_{SPTP} ($\mathrm{W/cm^2}$)
Date: 5/10/2017	Array: THX5A JV910	f_c: 5.35 MHz								
1_{A}	R333 / Left lobe	6.0	2.2	11	30-35	12.3-13.9	∞	1-64	1.44	48.0-56.0
Date: 6/14/2017	Array: THX5A JV910	f_c: 5.35 MHz								
2_{B}	R335 / Middle lobe	6.0	2.2	7	30-35	12.5-13.9	∞	1-64	1.44	48.0-56.0
3_{C}	R335 / Left lobe	6.0	2.2	6	30-35	12.5-13.9	∞	1-64	1.44	48.0-56.0
	Array: THX5A JV933	f_c: 5.50 MHz								
4_{D}	R336 / Middle lobe	6.0	2.2	4	30-35	13.1-14.0	∞	1-64	1.44	48.2-56.3
5_{E}	R336 / Right lobe	6.0	2.2	8	30-35	13.1-14.0	∞	1-64	1.44	48.2-56.3
Date: 10/11/2017	Array: THX5A JV910	f_c: 5.35 MHz								
6	R340 / Middle lobe	6.0	2.2	7	30-35	13.1-14.2	∞	1-64	1.44	48.0-56.0
7_{F}	R341 / Left lobe	6.0	2.2	5	30-35	13.1-14.2	∞	1-64	1.44	48.0-56.0
Date: 11/15/2017	Array: THX5A JV910	f_c: 5.35 MHz								
8	R342 / Middle lobe	6.0	2.2	4	30-35	13.1-14.7	∞	1-64	1.44	48.0-56.0
9_{G}	R342 / Left lobe	6.0	2.2	4	30-35	13.1-14.7	∞	1-64	1.44	48.0-56.0
10_{H}	R343 / Right lobe	6.0	2.2	6	30-35	13.1-14.7	∞	1-64	1.44	48.0-56.0

Table A.4: Time stamps and effective tumor diameters for controlled *in vivo* HIFU thermal ablation trials (gray-shaded rows represent trials excluded from the statistical analysis).

Trial #	Iris B-scan before thx	Iris B-scan after thx	File name	Tumor diameter
Date: 5/10/2017	Array: THX5A JV910	f_c: 5.35 MHz		(mm)
1	09:41:27	NA	05102017_094429	no tumor
1 (left mark)	NA	NA	05102017_094633	—
1 (right mark)	NA	NA	05102017_095014	—
2	10:00:51	10:02:15	05102017_100011	7.39
Date: 6/14/2017	Array: THX5A JV910	f_c: 5.35 MHz		
3	NA	NA	06142017_082558	6.38
3 (left mark)	NA	NA	06142017_082703	—
3 (right mark)	NA	NA	06142017_082839	—
4	08:53:48	08:55:26	06142017_085318	no tumor
4 (left mark)	NA	NA	06142017_085429	—
4 (right mark)	NA	08:58:51	06142017_085608	—
	Array: THX5A JV933	f_c: 5.50 MHz		
5	09:43:03	NA	06142017_094316	no tumor
5 (left mark)	NA	NA	06142017_094410	—
5 (right mark)	NA	09:48:30	06142017_094547	—
Date: 10/11/2017	Array: THX5A JV910	f_c: 5.35 MHz		
6	08:20:56	NA	10112017_082128	5.47
6 (left mark)	NA	NA	10112017_082231	—
6 (right mark)	NA	08:26:39	10112017_082340	—
7	NA	NA	10112017_083429	no tumor
7 (left mark)	NA	08:35:09	10112017_083528	—
7 (right mark)	NA	08:38:21	10112017_083630	—
8	09:17:43	NA	10112017_091745	11.58
8 (left mark)	NA	NA	10112017_091914	—
8 (right mark)	NA	09:23:50	10112017_092054	—
9	09:30:03	NA	10112017_093011	12.72
9 (left mark)	NA	NA	10112017_093139	—
9 (right mark)	NA	09:36:15	10112017_093317	—
10	09:52:33	NA	10112017_095246	no tumor
10 (left mark)	NA	NA	10112017_095342	—
10 (right mark)	NA	09:57:36	10112017_095439	—
Date: 11/15/2017	Array: THX5A JV910	f_c: 5.35 MHz		
11	09:12:54	09:15:50	11152017_081323	8.13
11 (left mark)	NA	NA	11152017_081440	—
11 (right mark)	NA	09:18:39	11152017_081626	—
12	10:18:12	NA	11152017_091839	5.43
12 (left mark)	NA	10:21:01	11152017_091945	—
12 (right mark)	NA	10:24:44	11152017_092134	—
13	10:33:03	NA	11152017_093436	no tumor
13 (left mark)	NA	10:37:02	11152017_093543	—
13 (right mark)	NA	10:38:58	11152017_093646	—
14	10:41:06	NA	11152017_094049	no tumor
14 (left mark)	NA	10:43:10	11152017_094200	—
14 (right mark)	NA	10:45:37	11152017_094307	—

Table A.5: Time stamps and effective tumor diameters for controlled *in vivo* unfocused ultrasound thermal ablation trials (gray-shaded rows represent trials excluded from the statistical analysis).

Trial #	Iris B-scan before thx	Iris B-scan after thx	File name	Tumor diameter
Date: 5/10/2017	Array: THX5A JV910	f_c: 5.35 MHz		(mm)
1	08:43:53	08:56:34	05102017_085223	3.75
Date: 6/14/2017	Array: THX5A JV910	f_c: 5.35 MHz		
2	NA	08:39:06	06142017_083527	15.15
3	08:47:34	08:50:24	06142017_084658	10.31
	Array: THX5A JV933	f_c: 5.50 MHz		
4	09:20:57	09:24:47	06142017_092132	15.81
5	09:29:49	09:33:10	06142017_092931	16.79
Date: 10/11/2017	Array: THX5A JV910	f_c: 5.35 MHz		
6	08:48:01	08:52:35	10112017_084804	6.59
7	09:42:00	09:48:17	10112017_094444	14.11
Date: 11/15/2017	Array: THX5A JV910	f_c: 5.35 MHz		
8	09:21:30	09:29:27	11152017_082157	3.11
9	09:39:22	09:42:34	11152017_083857	6.21
10	10:53:34	10:57:07	11152017_095314	8.53

Bibliography

[1] American Cancer Society, *Cancer Facts and Figures 2018*. Atlanta: American Cancer Society, 2018.

[2] H. K. Weir, T. D. Thompson, A. Soman, B. Møller, and S. Leadbetter, "The past, present, and future of cancer incidence in the United States: 1975 through 2020," *Cancer*, vol. 121, no. 11, pp. 1827–1837, 2015.

[3] A. Forner, M. Reig, and J. Bruix, "Hepatocellular carcinoma," *The Lancet*, vol. 391, no. 10127, pp. 1301–1314, 2018.

[4] M. Sherman, "Hepatocellular carcinoma: Epidemiology, surveillance, and diagnosis," *Semin. Liver Dis.*, vol. 30, no. 01, pp. 3–16, 2010.

[5] C. Bosetti, F. Turati, and C. L. Vecchia, "Hepatocellular carcinoma epidemiology," *Best Pract. Res. Clin. Gastroenterol.*, vol. 28, no. 5, pp. 753–770, 2014.

[6] F. Turati, C. Galeone, M. Rota, C. Pelucchi, E. Negri, V. Bagnardi, G. Corrao, P. Boffetta, and C. La Vecchia, "Alcohol and liver cancer: a systematic review and meta-analysis of prospective studies," *Ann. Oncol.*, vol. 25, no. 8, pp. 1526–1535, 2014.

[7] F. Trevisani, M. C. Cantarini, J. R. Wands, and M. Bernardi, "Recent advances in the natural history of hepatocellular carcinoma," *Carcinogenesis*, vol. 29, no. 7, pp. 1299–1305, 2008.

[8] Y. Kei, H. Setsuo, S. Michiie, K. Toshio, and S. Yukio, "Growth and spread of hepatocellular carcinoma: A review of 240 consecutive autopsy cases," *Cancer*, vol. 66, no. 10, pp. 2174–2179, 1990.

[9] M. Schlageter, L. M. Terracciano, S. D'Angelo, and P. Sorrentino, "Histopathology of hepatocellular carcinoma," *World J. Gastroenterol.*, vol. 20, no. 43, pp. 15955–15964, 2014.

[10] A. Forner, M. Gilabert, J. Bruix, and J.-L. Raoul, "Treatment of intermediate-stage hepatocellular carcinoma," *Nat. Rev. Clin. Oncol.*, vol. 11, pp. 525–535, 2014.

[11] P. Lersritwimanmaen and S. Nimanong, "Hepatocellular carcinoma surveillance: Benefit of serum alfa-fetoprotein in real-world practice," *Euroasian J. Hepatogastroenterol.*, vol. 8, no. 1, pp. 83–87, 2018.

[12] A. B. Benson, T. A. Abrams, E. Ben-Josef, P. M. Bloomston, J. F. Botha, B. M. Clary, A. Covey, S. A. Curley, M. I. D'Angelica, R. Davila, W. D. Ensminger, J. F. Gibbs, D. Laheru, M. P. Malafa, J. Marrero, S. G. Meranze, S. J. Mulvihill, J. O. Park, J. A. Posey, J. Sachdev, R. Salem, E. R. Sigurdson, C. Sofocleous, J.-N. Vauthey, A. P. Venook, L. W. Goff, Y. Yen, and A. X. Zhu, "Hepatobiliary cancers: Clinical practice guidelines in Oncology," *J. Natl. Compr. Canc. Netw.*, vol. 7, no. 4, pp. 350–391, 2009.

[13] A. Forner, M. E. Reig, C. Rodriguez de Lope, and J. Bruix, "Current strategy for staging and treatment: The BCLC update and future prospects," *Semin. Liver Dis.*, vol. 30, no. 01, pp. 061–074, 2010.

[14] R. Hernaez and H. B. El-Serag, "How we approach it: Treatment options for hepatocellular carcinoma," *Am. J. Gastroenterol.*, vol. 113, no. 6, pp. 791–794, 2018.

[15] J. Bruix, M. Reig, and M. Sherman, "Evidence-based diagnosis, staging, and treatment of patients with hepatocellular carcinoma," *Gastroenterology*, vol. 150, no. 4, pp. 835–853, 2016.

[16] S. G. Delis and C. Dervenis, "Selection criteria for liver resection in patients with hepatocellular carcinoma and chronic liver disease," *World J. Gastroenterol.*, vol. 14, no. 22, pp. 3452–3460, 2008.

[17] F. Ardito, M. Vellone, A. Cassano, A. M. De Rose, C. Pozzo, A. Coppola, B. Federico, I. Giovannini, C. Barone, G. Nuzzo, and F. Giuliante, "Chance of cure following liver resection for initially unresectable colorectal metastases: Analysis of actual 5-year survival," *J. Gastrointest. Surg.*, vol. 17, no. 2, pp. 352–359, 2013.

[18] V. Dhar, R. M. Thomas, and S. A. Ahmad, *Repeat Hepatectomy for Colorectal Liver Metastases*, pp. 203–220. Cham: Springer International Publishing, 2016.

[19] J. Scheele, R. Stang, A. Altendorf-Hofmann, and M. Paul, "Resection of colorectal liver metastases," *World J. Surg.*, vol. 19, no. 1, pp. 59–71, 1995.

[20] E. K. Abdalla, J.-N. Vauthey, L. M. Ellis, V. Ellis, R. Pollock, K. R. Broglio, K. Hess, and S. A. Curley, "Recurrence and outcomes following hepatic resection, radiofrequency ablation, and combined resection/ablation for colorectal liver metastases," *Ann. Surg.*, vol. 239, no. 6, pp. 818–827, 2004.

[21] E. J. A. Morris, D. Forman, J. D. Thomas, P. Quirke, E. F. Taylor, L. Fairley, B. Cottier, and G. Poston, "Surgical management and outcomes of colorectal cancer liver metastases," *BJS*, vol. 97, no. 7, pp. 1110–1118, 2010.

[22] R. Adam, V. Delvart, G. Pascal, A. Valeanu, D. Castaing, D. Azoulay, S. Giacchetti, B. Paule, F. Kunstlinger, O. Ghémard, F. Levi, and H. Bismuth, "Rescue surgery for unresectable colorectal liver metastases downstaged by chemotherapy: A model to predict long-term survival," *Ann. Surg.*, vol. 240, no. 4, pp. 644–658, 2004.

[23] P. Yao and D. L. Morris, "Radiofrequency ablation-assisted liver resection: review of the literature and our experience," *HPB (Oxford)*, vol. 8, no. 4, pp. 248–254, 2006.

[24] H. Shen, S. Zhou, Y. Lou, Y. Gao, S. Cao, D. Wu, and G. Li, "Microwave-assisted ablation improves the prognosis of patients with hepatocellular carcinoma undergoing liver resection," *Technol. Cancer Res. Treat.*, vol. 17, pp. 1–6, 2018.

[25] K. H. Kim, Y. S. Yoon, C. S. Yu, T. W. Kim, H. J. Kim, P. N. Kim, H. K. Ha, and J. C. Kim, "Comparative analysis of radiofrequency ablation and surgical resection for colorectal liver metastases," *J. Korean Surg. Soc.*, vol. 81, no. 1, pp. 25–34, 2011.

[26] T. Chartier, O. Carpentier, B. Genestie, J.-C. Hornez, and F. Monchau, "Numerical and *ex vivo* studies of a bioprobe developed for laser-induced thermotherapy (LITT) in contact with liver tissue," *Med. Eng. Physics.*, vol. 38, no. 8, pp. 733–740, 2016.

[27] M. W. Lee, S. S. Raman, N. H. Asvadi, S. Siripongsakun, R. M. Hicks, J. Chen, A. Worakitsitisatorn, J. McWilliams, M. J. Tong, R. S. Finn, V. G. Agopian, R. W. Busuttil, and D. S. K. Lu, "Radiofrequency ablation of hepatocellular carcinoma as bridge therapy to liver transplantation: A 10-year intention-to-treat analysis," *Hepatology*, vol. 65, no. 6, pp. 1979–1990, 2017.

[28] R. Hoffmann, H. Rempp, D.-E. Kessler, J. Weiss, P. L. Pereira, K. Nikolaou, and S. Clasen, "MR-guided microwave ablation in hepatic tumours: initial results in clinical routine," *Eur. Radiol.*, vol. 27, no. 4, pp. 1467–1476, 2017.

[29] I. R. S. Makin, T. D. Mast, W. Faidi, P. G. Runk, M. M.and Barthe, , and M. H. Slayton, "Miniaturized ultrasound arrays for interstitial ablation and imaging," *Ultrasound Med. Biol.*, vol. 31, no. 11, pp. 1539–1550, 2005.

[30] E. Delabrousse, R. Salomir, A. Birer, C. Paquet, F. Mithieux, J.-Y. Chapelon, F. Cotton, and C. Lafon, "Automatic temperature control for MR-guided interstitial ultrasound ablation in liver using a percutaneous applicator: *Ex vivo* and *in vivo* initial studies," *Magn. Reson. Med.*, vol. 63, no. 3, pp. 667–679, 2010.

[31] D. Melodelima, W. A. N'Djin, H. Parmentier, S. Chesnais, M. Rivoire, and J.-Y. Chapelon, "Thermal ablation by high-intensity-focused ultrasound using a toroid transducer increases the coagulated volume. results of animal experiments," *Ultrasound Med. Biol.*, vol. 35, no. 3, pp. 425–435, 2009.

[32] J. Vincenot, D. Melodelima, F. Chavrier, A. Vignot, A. Kocot, and J.-Y. Chapelon, "Electronic beam steering used with a toroidal HIFU transducer substantially increases the coagulated volume," *Ultrasound Med. Biol.*, vol. 39, no. 7, pp. 1241–1254, 2013.

[33] T. R. Fosnight, F. M. Hooi, R. D. Keil, A. P. Ross, S. Subramanian, T. G. Akinyi, J. K. Killin, P. G. Barthe, S. M. Rudich, S. A. Ahmad, M. B. Rao, and T. D. Mast, "Echo decorrelation imaging of rabbit liver and VX2 tumor during *in vivo* ultrasound ablation," *Ultrasound Med. Biol.*, vol. 43, no. 1, pp. 176–186, 2017.

[34] T. J. Vogl, A. Dommermuth, B. Heinle, N.-E. A. Nour-Eldin, T. Lehnert, K. Eichler, S. Zangos, W. O. Bechstein, and N. N. N. Naguib, "Colorectal cancer liver metastases: Long-term survival and progression-free survival after thermal ablation using magnetic resonance-guided laser-induced interstitial thermotherapy in 594 patients: Analysis of prognostic factors," *Invest. Radiol.*, vol. 49, no. 1, 2014.

[35] E. van Sonnenberg, W. McMullen, and L. Solbiati, *Tumor Ablation.* New York, New York: Springer-Verlag, 1 ed., 2005.

[36] L. Zhang, H. Zhu, C. Jin, K. Zhou, K. Li, H. Su, W. Chen, J. Bai, and Z. Wang, "High-intensity focused ultrasound (HIFU): Effective and safe therapy for hepatocellular carcinoma adjacent to major hepatec veins," *Eur. Radiol.*, vol. 19, pp. 437–445, 2009.

[37] J.-F. Aubry, K. B. Pauly, C. Moonen, G. Haar, M. Ries, R. Salomir, S. Sokka, K. M. Sekins, Y. Shapira, F. Ye, H. Huff-Simonin, M. Eames, A. Hananel, N. Kassell, A. Napoli, J. H. Hwang, F. Wu, L. Zhang, A. Melzer, Y.-S. Kim, and W. M. Gedroyc, "The road to clinical use of high-intensity focused ultrasound for liver cancer: Technical and clinical consensus," *J. Ther. Ultrasound*, vol. 1, no. 1, pp. 13–20, 2013.

[38] J. Luo, X. Ren, and T. Yu, "Efficacy of extracorporeal ultrasound-guided high intensity focused ultrasound: An evaluation based on controlled trials in China," *Int. J. Radiat. Biol.*, vol. 91, no. 6, pp. 480–485, 2015.

[39] D. S. Lu, S. S. Raman, P. Limanond, D. Aziz, J. Economou, R. Busuttil, and J. Sayre, "Influence of large peritumoral vessels on outcome of radiofrequency ablation of liver tumors," *J. Vasc. Interv. Radiol.*, vol. 14, no. 10, pp. 1267–1274, 2003.

[40] T. Hideo, A. Muhammet, A. Erol, K. Koray, and B. Eren, "Local recurrence after laparoscopic radiofrequency ablation of malignant liver tumors: Results of a contemporary series," *J. Surg. Oncol.*, vol. 115, no. 7, pp. 830–834, 2017.

[41] K. Hynynen, A. Darkazanli, E. Unger, and J. F. Schenck, "MRI-guided noninvasive ultrasound surgery," *Med. Phys.*, vol. 20, no. 1, pp. 107–115, 1993.

[42] A. Darkazanli, K. Hynynen, E. C. Unger, and J. F. Schenck, "On-line monitoring of ultrasonic surgery with MR imaging," *J. Magn. Reson. Imaging*, vol. 3, no. 3, pp. 509–514, 1993.

[43] C. Bohris, W. G. Schreiber, J. Jenne, I. Simiantonakis, R. Rastert, H. Zabel, P. Huber, R. Bader, and G. Brix, "Quantitative MR temperature monitoring of high-intensity focused ultrasound therapy," *Magn. Reson. Imaging*, vol. 17, no. 4, pp. 603–610, 1999.

[44] K. Hynynen and N. McDannold, "MRI guided and monitored focused ultrasound thermal ablation methods: A review of progress," *Int. J. Hyperthermia*, vol. 20, no. 7, pp. 725–737, 2004.

[45] P. Bour, F. Marquet, V. Ozenne, S. Toupin, E. Dumont, J.-F. Aubry, M. Lepetit-Coiffe, and B. Quesson, "Real-time monitoring of tissue displacement and temperature changes during MR-guided high intensity focused ultrasound," *Magn. Reson. Med.*, 2017.

[46] Y.-F. Zhou, "High intensity focused ultrasound in clinical tumor ablation," *World J. Clin. Oncol.*, vol. 2, no. 1, pp. 8–27, 2011.

[47] A. Napoli, M. Anzidei, F. Ciolina, E. Marotta, B. Cavallo Marincola, G. Brachetti, L. Di Mare, G. Cartocci, F. Boni, V. Noce, L. Bertaccini, and C. Catalano, "MR-guided high-intensity focused ultrasound: Current status of an emerging technology," *Cardiovasc. Intervent. Radiol.*, vol. 36, pp. 1190–1203, Oct 2013.

[48] F. Wu, Z.-B. Wang, W.-Z. Chen, H. Zhu, J. Bai, J.-Z. Zou, K.-Q. Li, C.-B. Jin, F.-L. Xie, and H.-B. Su, "Extracorporeal high intensity focused ultrasound ablation in the treatment of patients with large hepatocellular carcinoma," *Ann. Surg. Oncol.*, vol. 11, no. 12, p. 1061, 2004.

[49] J. Kennedy, F. Wu, G. ter Haar, F. Gleeson, R. Phillips, M. Middleton, and D. Cranston, "High-intensity focused ultrasound for the treatment of liver tumours," *Ultrasonics*, vol. 42, no. 19, pp. 931–935, 2004.

[50] R. O. Illing, J. E. Kennedy, F. Wu, G. R. ter Haar, A. S. Protheroe, P. J. Friend, F. V. Gleeson, D. W. Cranston, R. R. Phillips, and M. R. Middleton, "The safety and feasibility of extracorporeal high-intensity focused ultrasound (HIFU) for the treatment of liver and kidney tumours in a Western population," *Br. J. Cancer*, vol. 93, no. 8, pp. 890–895, 2005.

[51] H. C. Klingler, M. Susani, R. Seip, J. Mauermann, N. Sanghvi, and M. J. Marberger, "A novel approach to energy ablative therapy of small renal tumours: Laparoscopic high-intensity focused ultrasound," *Eur. Urol.*, vol. 53, no. 4, pp. 810–818, 2008.

[52] S. Vaezy, X. Shi, R. W. Martin, E. Chi, P. I. Nelson, M. R. Bailey, and L. A. Crum, "Real-time visualization of high-intensity focused ultrasound treatment using ultrasound imaging," *Ultrasound Med. Biol.*, vol. 27, no. 1, pp. 33–42, 2001.

[53] M. Gudur, R. Kumon, Y. Zhou, and C. Deng, "High-frequency rapid B-mode ultrasound imaging for real-time monitoring of lesion," *IEEE Trans. Ultrason., Ferroelectr., Freq. Control*, vol. 59, no. 8, pp. 1687–1699, 2012.

[54] R. E. Kumon, M. S. Gudur, Y. Zhou, and C. X. Deng, "High-frequency ultrasound M-mode imaging for identifying lesion and bubble activity during high-intensity focused ultrasound ablation," *Ultrasound Med. Biol.*, vol. 38, no. 4, pp. 626–641, 2012.

[55] R. Seip, J. Tavakkoli, R. Carlson, A. Wunderlich, N. Sanghvi, K. Dines, and T. Gardner, "High-intensity focused ultrasound (HIFU) multiple lesion imaging: Comparison of detection algorithms for real-time treatment control," in *Proc. IEEE Int. Ultrason. Symp.*, vol. 2, pp. 1427–1430, 2002.

[56] W. Chen, N. T. Sanghvi, R. Carlson, and T. Uchida, "Real-time tissue change monitoring on the Sonablate® 500 during high intensity focused ultrasound (HIFU) treatment of prostate cancer," *AIP Conf. Proc.*, vol. 1359, no. 1, pp. 391–396, 2011.

[57] T. Shishitani, R. Matsuzawa, S. Yoshizawa, and S.-I. Umemura, "Changes in backscatter of liver tissue due to thermal coagulation induced by focused ultrasound," *J. Acoust. Soc. Am.*, vol. 134, no. 2, pp. 1724–1730, 2013.

[58] R. Souchon, G. Bouchoux, E. Maciejko, C. Lafon, D. Cathignol, M. Bertrand, and J.-Y. Chapelon, "Monitoring the formation of thermal lesions with heat-induced echostrain imaging: A feasibility study," *Ultrasound Med. Biol.*, vol. 31, no. 2, pp. 251–259, 2005.

[59] Y. Han, G. Y. Hou, S. Wang, and E. Konofagou, "High intensity focused ultrasound (HIFU) focal spot localization using harmonic motion imaging (HMI)," *Phys. Med. Biol.*, vol. 60, no. 15, p. 5911, 2015.

[60] J. Grondin, T. Payen, S. Wang, and E. E. Konofagou, "Real-time monitoring of high intensity focused ultrasound (HIFU) ablation of *in vitro* canine livers using harmonic motion imaging for focused ultrasound (HMIFU)," *JOVE J. Vis. Exp.*, vol. 105, p. 53050, 2015.

[61] H. Yang, W. Shutao, P. Thomas, and K. Elisa, "Fast lesion mapping during HIFU treatment using harmonic motion imaging guided focused ultrasound (HMIgFUS) *in vitro* and *in vivo*," *Phys. Med. Biol.*, vol. 62, no. 8, pp. 3111–3123, 2017.

[62] R. Iwasaki, R. Takagi, R. Nagaoka, H. Jimbo, S. Yoshizawa, Y. Saijo, and S.-I. Umemura, "Monitoring of high-intensity focused ultrasound treatment by shear wave

elastography induced by two-dimensional-array therapeutic transducer," *Jpn. J. Appl. Phys.*, vol. 55, no. 7S1, p. 07KF05, 2016.

[63] F. L. Lizzi, R. Muratore, C. X. Deng, J. A. Ketterling, S. Alam, S. Mikaelian, and A. Kalisz, "Radiation-force technique to monitor lesions during ultrasonic therapy," *Ultrasound Med. Biol.*, vol. 29, no. 11, pp. 1593–1605, 2003.

[64] T. Varghese, U. Techavipoo, J. A. Zagzebski, and J. Lee, F. T., "Impact of gas bubbles generated during interstitial ablation on elastographic depiction of *in vitro* thermal lesions," *J. Ultrasound Med.*, vol. 23, no. 4, pp. 535–544, 2004.

[65] V. Suomi, Y. Han, E. Konofagou, and R. O. Cleveland, "The effect of temperature dependent tissue parameters on acoustic radiation force induced displacements," *Phys. Med. Biol.*, vol. 61, no. 20, pp. 7427–7447, 2016.

[66] L. Curiel, Y. Huang, N. Vykhodtseva, and K. Hynynen, "Focused ultrasound treatment of VX2 tumors controlled by local harmonic motion," *Phys. Med. Biol.*, vol. 54, no. 11, p. 3405, 2009.

[67] A. J. Casper, D. Liu, J. R. Ballard, and E. S. Ebbini, "Real-time implementation of a dual-mode ultrasound array system: *In vivo* results," *IEEE Trans. Biomed. Eng.*, vol. 60, no. 10, pp. 2751–2759, 2013.

[68] B. Majaron, P. Plestenjak, and M. Lukač, "Thermo-mechanical laser ablation of soft biological tissue: Modeling the micro-explosion," *Appl. Phys. B.*, vol. 69, pp. 71–80, Jul 1999.

[69] J. B. Kruskal, B. Oliver, J.-C. Huertas, and S. N. Goldberg, "Dynamic intrahepatic flow and cellular alterations during radiofrequency ablation of liver tissue in mice," *J. Vasc. Interv. Radiol.*, vol. 12, no. 10, pp. 1193–1201, 2001.

[70] F. M. Hooi, A. Nagle, S. Subramanian, and T. D. Mast, "Analysis of tissue changes, measurement system effects, and motion artifacts in echo decorrelation imaging," *J. Acoust. Soc. Am.*, vol. 137, no. 2, pp. 585–597, 2015.

[71] J.-E. Kim, Y.-S. Kim, H. Rhim, H. K. Lim, M. W. Lee, D. Choi, S. W. Shin, and S. K. Cho, "Outcomes of patients with hepatocellular carcinoma referred for percutaneous radiofrequency ablation at a tertiary center: Analysis focused on the feasibility with the use of ultrasonography guidance," *Eur. J. Radiol.*, vol. 79, no. 2, pp. e80–e84, 2011.

[72] P.-C. Liang, H.-S. Lai, T.-F. Shih, C.-H. Wu, and K.-W. Huang, "Initial institutional experience of uncooled single-antenna microwave ablation for large hepatocellular carcinoma," *Clin. Radiol.*, vol. 70, no. 5, pp. e35–e40, 2015.

[73] P. D. Hansen, M. A. Cassera, and R. F. Wolf, "Ablative technologies for hepatocellular, cholangiocarcinoma, and metastatic colorectal cancer of the liver," *Surg. Oncol. Clin. N. Am.*, vol. 24, no. 1, pp. 97–119, 2015.

[74] Y.-S. Kim, H. K. Lim, H. Rhim, M. W. Lee, D. Choi, W. J. Lee, S. W. Paik, K. C. Koh, J. H. Lee, M. S. Choi, G.-Y. Gwak, and B. C. Yoo, "Ten-year outcomes of percutaneous radiofrequency ablation as first-line therapy of early hepatocellular carcinoma: Analysis of prognostic factors," *J. Hepatol.*, vol. 58, no. 1, pp. 89–97, 2013.

[75] R. Liu, K. Li, H. Luo, W. Zhang, T. Zhang, M. Gao, W. Zha, X. Cui, and Y. Deng, "Ultrasound-guided percutaneous microwave ablation for small liver cancers adjacent to large vessels: long-term outcomes and strategies," *Oncol. Transl. Med.*, vol. 3, pp. P57–P64, 2017.

[76] J. Engstrand, G. Toporek, P. Harbut, E. Jonas, H. Nilsson, and J. Freedman, "Stereotactic CT-guided percutaneous microwave ablation of liver tumors with the use of high-frequency jet ventilation: An accuracy and procedural safety study," *Am. J. Roentgenol.*, vol. 208, no. 1, pp. 193–200, 2016.

[77] H. Rempp, R. Hoffmann, J. Roland, A. Buck, A. Kickhefel, C. D. Claussen, P. L. Pereira, F. Schick, and S. Clasen, "Threshold-based prediction of the coagulation zone in sequential temperature mapping in MR-guided radiofrequency ablation of liver tumours," *Eur. Radiol.*, vol. 22, no. 5, pp. 1091–1100, 2012.

[78] M. Lepetit-Coiffé, H. Laumonier, O. Seror, B. Quesson, M.-B. Sesay, C. T. W. Moonen, N. Grenier, and H. Trillaud, "Real-time monitoring of radiofrequency ablation of liver tumors using thermal-dose calculation by MR temperature imaging: Initial results in nine patients, including follow-up," *Eur. Radiol.*, vol. 20, no. 1, pp. 193–201, 2010.

[79] K. K. Vigen, J. Jarrard, V. Rieke, J. Frisoli, B. L. Daniel, and K. B. Pauly, "*In vivo* porcine liver radiofrequency ablation with simultaneous MR temperature imaging," *J. Magn. Reson. Imaging*, vol. 23, no. 4, pp. 578–584, 2006.

[80] S. J. Ahn, J. M. Lee, D. H. Lee, S. M. Lee, J.-H. Yoon, Y. J. Kim, J.-H. Lee, S. J. Yu, and J. K. Han, "Real-time US-CT/MR fusion imaging for percutaneous radiofrequency ablation of hepatocellular carcinoma," *J. Hepatol.*, vol. 66, no. 2, pp. 347–354, 2017.

[81] S.-Y. Yan, Y. Zhang, C. Sun, H.-X. Cao, G.-M. Li, Y.-Q. Wang, and J.-G. Fan, "Comparison of real-time contrast-enhanced ultrasonography and standard ultrasonography in liver cancer microwave ablation," *Exp. Ther. Med.*, vol. 12, no. 3, pp. 1345–1348, 2016.

[82] S. S. Raman, D. S. K. Lu, D. J. Vodopich, J. Sayre, and C. Lassman, "Creation of radiofrequency lesions in a porcine model: Correlation with sonography, CT, and histopathology," *Am. J. Roentgenol.*, vol. 175, no. 5, pp. 1253–1258, 2000.

[83] R. Sugiyama, K. Kanazawa, M. Seki, T. Azuma, A. Sasaki, H. Takeuchi, K. Fujiwara, K. Itani, S. Tamano, K. Yoshinaka, S. Takagi, and Y. Matsumoto, "Real-time feedback control for high-intensity focused ultrasound system using localized motion imaging," *Jpn. J. Appl. Phys.*, vol. 54, no. 7S1, p. 07HD15, 2015.

[84] R. Takagi, H. Jimbo, R. Iwasaki, K. Tomiyasu, S. Yoshizawa, and S.-I. Umemura, "Feasibility of real-time treatment feedback using novel filter for eliminating therapeutic ultrasound noise with high-speed ultrasonic imaging in ultrasound-guided high-intensity focused ultrasound treatment," *Jpn. J. Appl. Phys.*, vol. 55, no. 7S1, p. 07KC10, 2016.

[85] N. Toshikuni, Y. Matsue, K. Ozaki, K. Yamada, N. Hayashi, M. Tsuchishima, and M. Tsutsumi, "An image fusion system for estimating the therapeutic effects of radiofrequency ablation on hepatocellular carcinoma," *Radiol. Oncol.*, vol. 51, no. 3, pp. 263–269, 2017.

[86] O. Al-Bataineh, J. Jenne, and P. Huber, "Clinical and future applications of high intensity focused ultrasound in cancer," *Cancer Treat. Rev.*, vol. 38, no. 5, pp. 346–353, 2012.

[87] X. Qu, T. Azuma, R. Sugiyama, K. Kanazawa, M. Seki, A. Sasaki, H. Takeuchi, K. Fujiwara, K. Itani, S. Tamano, S. Takagi, I. Sakuma, and Y. Matsumoto, "Improved highly accurate localized motion imaging for monitoring high-intensity focused ultrasound therapy," *Jpn. J. Appl. Phys.*, vol. 55, no. 7S1, p. 07KF04, 2016.

[88] S. Subramanian, S. M. Rudich, A. Alqadah, C. P. Karunakaran, M. B. Rao, and T. D. Mast, "*In vivo* thermal ablation monitoring using ultrasound echo decorrelation imaging," *Ultrasound Med. Biol.*, vol. 40, no. 1, pp. 102–114, 2014.

[89] T. D. Mast, D. Pucke, S. Subramanian, W. Bowlus, S. Rudich, and J. Buell, "Ultrasound monitoring of *in vitro* radio frequency ablation by echo decorrelation," *J. Ultrasound Med.*, vol. 27, no. 12, pp. 1685–1697, 2008.

[90] R. Matsuzawa, T. Shishitani, S. Yoshizawa, and S.-I. Umemura, "Monitoring of lesion induced by high-intensity focused ultrasound using correlation method based on block matching," *Jpn. J. Appl. Phys.*, vol. 51, no. 7S, p. 07GF26, 2012.

[91] S. Sasaki, R. Takagi, K. Matsuura, S. Yoshizawa, and S.-I. Umemura, "Monitoring of high-intensity focused ultrasound lesion formation using decorrelation between high-speed ultrasonic images by parallel beamforming," *Jpn. J. Appl. Phys.*, vol. 53, no. 7S, p. 07KF10, 2014.

[92] S. Subramanian, D. T. Schmidt, M. B. Rao, and T. D. Mast, "Dependence of ultrasound echo decorrelation on local tissue temperature during *ex vivo* radiofrequency ablation," *Phys. Med. Biol.*, vol. 61, no. 6, pp. 2356–2371, 2016.

[93] P. Wiggermann, K. Brnn, J. Rennert, M. Loss, H. Wobser, A. Schreyer, C. Stroszczynski, and E. Jung, "Monitoring during hepatic radiofrequency ablation (RFA): Comparison of real-time ultrasound elastography (RTE) and contrast-enhanced ultrasound (CEUS): First clinical results of 25 patients," *Eur. J. Ultrasound*, vol. 34, no. 6, pp. 590–594, 2013.

[94] W. Yang, M. Alexander, N. Rubert, A. Ingle, M. Lubner, T. Ziemlewicz, J. L. Hinshaw, F. T. Lee, J. A. Zagzebski, and T. Varghese, "Monitoring microwave ablation for liver tumors with electrode displacement strain imaging," in *Proc. IEEE Int. Ultrason. Symp.*, pp. 1128–1131, 2014.

[95] Y.-D. Liu, Q. Li, Z. Zhou, Y.-W. Yeah, C.-C. Chang, C.-Y. Lee, and P.-H. Tsui, "Adaptive ultrasound temperature imaging for monitoring radiofrequency ablation," *PLoS One*, vol. 12, pp. 1–15, 08 2017.

[96] A. Casper, D. Liu, and E. S. Ebbini, "Realtime control of multiple-focus phased array heating patterns based on noninvasive ultrasound thermography," *IEEE Trans. Biomed. Eng.*, vol. 59, no. 1, pp. 95–105, 2012.

[97] J. Foiret and K. W. Ferrara, "Spatial and temporal control of hyperthermia using real time ultrasonic thermal strain imaging with motion compensation, phantom study," *PLoS One*, vol. 10, pp. 1–22, 08 2015.

[98] T. R. Fosnight, F. M. Hooi, R. D. Keil, S. Subramanian, P. G. Barthe, W. Yang, R. Xiaoping, S. Ahmad, M. B. Rao, and T. D. Mast, "Motion-corrected echo decorrelation imaging of *in vivo* focused and bulk ultrasound ablation in a rabbit liver cancer model," in *Proc. IEEE Int. Ultrason. Symp.*, pp. 2161–2164, 2014.

[99] H. Zhong, M.-X. Wan, Y.-F. Jiang, and S.-P. Wang, "Monitoring imaging of lesions induced by high intensity focused ultrasound based on differential ultrasonic attenuation and integrated backscatter estimation," *Ultrasound Med. Biol.*, vol. 33, no. 1, pp. 82–94, 2007.

[100] T. D. Mast, I. R. S. Makin, W. Faidi, M. M. Runk, P. G. Barthe, and M. H. Slayton, "Bulk ablation of soft tissue with intense ultrasound: Modeling and experiments," *J. Acoust. Soc. Am.*, vol. 118, no. 4, pp. 2715–2724, 2005.

[101] H. Nishikawa and Y. Osaki, "Comparison of high-intensity focused ultrasound therapy and radiofrequency ablation for recurrent hepatocellular carcinoma," *Hepatobiliary Surg. Nutr.*, vol. 2, no. 3, pp. 168–170, 2013.

[102] P. G. Barthe, M. H. Slayton, P. M. Jaeger, I. R. S. Makin, L. A. Gallagher, T. D. Mast, M. M. Runk, and W. Faidi, "Ultrasound therapy system and ablation results utilizing miniature imaging/therapy arrays," in *Proc. IEEE Int. Ultrason. Symp.*, vol. 3, pp. 1792–1795, 2004.

[103] S. Zhou, J. Petruzzello, A. Anand, S. Sethuraman, and J. Azevedo, "Validating ultrasound-based HIFU lesion-size monitoring technique with MR thermometry and histology," *AIP Conf. Proc.*, vol. 1215, no. 1, pp. 53–56, 2010.

[104] J. W. Wijlemans, M. de Greef, G. Schubert, L. W. Bartels, C. T. Moonen, M. A. van den Bosch, and M. Ries, "A clinically feasible treatment protocol for magnetic resonance-guided high-intensity focused ultrasound ablation in the liver," *Invest. Radiol.*, vol. 50, no. 1, pp. 24–31, 2015.

[105] H. J. Scheffer, K. Nielsen, A. A. J. M. van Tilborg, J. M. Vieveen, R. A. Bouwman, G. Kazemier, H. W. M. Niessen, S. Meijer, C. van Kuijk, M. P. van den Tol, and M. R. Meijerink, "Ablation of colorectal liver metastases by irreversible electroporation: Results of the COLDFIRE-I ablate-and-resect study," *Eur. Radiol.*, vol. 24, no. 10, pp. 2467–2475, 2014.

[106] J. A. Hanley and B. J. McNeil, "The meaning and use of the area under a receiver operating characteristic (ROC) curve," *Radiology*, vol. 143, no. 1, pp. 64–71, 1982.

[107] W. J. Krzanowski and D. J. Hand, *ROC Curves for Continuous Data*. Chapman and Hall/CRC, 1st ed., 2009.

[108] E. R. DeLong, D. M. DeLong, and D. L. Clarke-Pearson, "Comparing the areas under two or more correlated receiver operating characteristic curves: A nonparametric approach," *Biometrics*, vol. 44, no. 3, pp. 837–845, 1988.

[109] W. H. Kruskal and W. A. Wallis, "Use of ranks in one-criterion variance analysis," *J. Am. Stat. Assoc.*, vol. 47, no. 260, pp. 583–621, 1952.

[110] O. J. Dunn, "Multiple comparisons using rank sums," *Technometrics*, vol. 6, no. 3, pp. 241–252, 1964.

[111] B. S. Holland and M. D. Copenhaver, "Improved Bonferroni-type multiple testing procedures: Correction to Holland and Copenhaver," *Psychol. Bull.*, vol. 104, no. 2, p. 299, 1988.

[112] X. Robin, N. Turck, A. Hainard, N. Tiberti, F. Lisacek, J.-C. Sanchez, and M. Müller, "pROC: an open-source package for R and S+ to analyze and compare ROC curves," *BMC Bioinformatics*, vol. 12, no. 1, pp. 77–85, 2011.

[113] L. Chen, G. ter Haar, C. R. Hill, M. Dworkin, P. Carnochan, H. Young, and J. P. M. Bensted, "Effect of blood perfusion on the ablation of liver parenchyma with high-intensity focused ultrasound," *Phys. Med. Biol.*, vol. 38, no. 11, pp. 1661–1673, 1993.

[114] S. Dasgupta, J. Wansapura, P. Hariharan, R. Pratt, D. Witte, M. R. Myers, and R. K. Banerjee, "HIFU lesion volume as a function of sonication time, as determined by MRI, histology, and computations," *J. Biomech. Eng.*, vol. 132, no. 8, p. 081005, 2010.

[115] E. S. Ebbini and G. ter Haar, "Ultrasound-guided therapeutic focused ultrasound: Current status and future directions," *Int. J. Hyperthermia*, vol. 31, no. 2, pp. 77–89, 2015.

[116] A. Okada, T. Murakami, K. Mikami, H. Onishi, N. Tanigawa, T. Marukawa, and H. Nakamura, "A case of hepatocellular carcinoma treated by MR-guided focused ultrasound ablation with respiratory gating," *Magn. Reson. Med. Sci.*, vol. 5, no. 3, pp. 167–171, 2006.

[117] J. M. M. van Breugel, J. W. Wijlemans, H. H. B. Vaessen, M. de Greef, C. T. W. Moonen, M. A. A. J. van den Bosch, and M. G. Ries, "Procedural sedation and analgesia for respiratory-gated MR-HIFU in the liver: A feasibility study," *J. Ther. Ultrasound*, vol. 4, no. 1, pp. 19–31, 2016.

[118] M. A. Abbass, J. K. Killin, N. Mahalingam, F. M. Hooi, P. G. Barthe, and T. D. Mast, "Real-time spatiotemporal control of high-intensity focused ultrasound thermal ablation using echo decorrelation imaging in *ex vivo* bovine liver," *Ultrasound Med. Biol.*, vol. 44, no. 1, pp. 199–213, 2018.

[119] M. A. Abbass, A.-J. Garbo, N. Mahalingam, J. K. Killin, and T. D. Mast, "Real-time control of bulk ultrasound thermal ablation using echo decorrelation imaging feedback," in *Proc. IEEE Int. Ultrason. Symp.*, 2017.

[120] M. T. Cox, M. A. Abbass, N. Mahalingam, A. J. Garbo, K. S. Krothapalli, and T. D. Mast, "Focused ultrasound ablation using electronically scanned grating lobes with real-time echo decorrelation imaging feedback," in *Proc. IEEE Int. Ultrason. Symp.*, Sept 2017.

[121] K. B. Bader and C. K. Holland, "Gauging the likelihood of stable cavitation from ultrasound contrast agents," *Phys. Med. Biol.*, vol. 58, no. 1, pp. 127–144, 2013.

[122] H. Iida, T. Aihara, S. Ikuta, and N. Yamanaka, "Effectiveness of impedance monitoring during radiofrequency ablation for predicting popping," *World J. Gastroenterol.*, vol. 18, no. 41, pp. 5870–5878, 2012.

[123] S. S. Shapiro and M. B. Wilk, "An analysis of variance test for normality (complete samples)," *Biometrika*, vol. 52, no. 3/4, pp. 591–611, 1965.

[124] M. S. Bartlett, "Properties of sufficiency and statistical tests," *Proc. R. Soc. Lond. Ser. A*, vol. 160, pp. 268–282, 1937.

[125] H. Levene, "Robust tests for equality of variances," in *Contributions to Probability and Statistics* (I. Olkin, ed.), pp. 278–292, Stanford Univ. Press, Stanford, Calif.: Palo Alto, 1960.

[126] J. H. Min, Y. Kim, H. Rhim, M. W. Lee, T. W. Kang, K. D. Song, and H. K. Lim, "Effect of parenchymal uptake of perfluorobutane microbubbles (Sonazoid) on radiofrequency ablation of the liver: *in vivo* experimental study," *Liver Int.*, vol. 36, no. 8, pp. 1187–1195, 2016.

[127] J. Choe, K. W. Kim, Y. I. Kim, J. W. Chung, J. Huh, J. Park, S. J. Ham, M. K. Jun, and P. N. Kim, "Feasibility of a low-power radiofrequency ablation protocol to delay steam popping," *J. Vasc. Interv. Radiol.*, vol. 27, no. 2, pp. 268–274, 2016.

[128] J. R. Leyendecker, G. D. Dodd, G. A. Halff, V. A. McCoy, D. H. Napier, L. G. Hubbard, K. N. Chintapalli, S. Chopra, W. K. Washburn, R. M. Esterl, F. G. Cigarroa, R. E. Kohlmeier, and F. E. Sharkey, "Sonographically observed echogenic response during intraoperative radiofrequency ablation of cirrhotic livers," *AJR Am. J. Roentgenol.*, vol. 178, no. 5, pp. 1147–1151, 2002.

[129] D. F. Bauer, "Constructing confidence sets using rank statistics," *J. Am. Stat. Assoc.*, vol. 67, no. 339, pp. 687–690, 1972.

[130] W. J. Conover, *Practical Nonparametric Statistics, 2nd ed.* New York Chichester Wiley, 1980.

[131] S. A. Sapareto and W. C. Dewey, "Thermal dose determination in cancer therapy," *Int. J. Radiat. Oncol. Biol. Phys.*, vol. 10, no. 6, pp. 787–800, 1984.

[132] W.-S. Chen, C. Lafon, T. J. Matula, S. Vaezy, and L. A. Crum, "Mechanisms of lesion formation in high intensity focused ultrasound therapy," *ARLO*, vol. 4, no. 2, pp. 41–46, 2003.

[133] F. Wu, W.-Z. Chen, J. Bai, J.-Z. Zou, Z.-L. Wang, H. Zhu, and Z.-B. Wang, "Pathological changes in human malignant carcinoma treated with high-intensity focused ultrasound," *Ultrasound Med. Biol.*, vol. 27, no. 8, pp. 1099–1106, 2001.

[134] F. Wu, "Clinical applications of high intensity focused ultrasound in the treatment of patients with solid malignancy," in *Emerging Therapeutic Ultrasound* (J. Wu and W. Nyborg, eds.), ch. 8, pp. 279–339, World Scientific, 2006.

[135] S. A. Wells, J. L. Hinshaw, M. G. Lubner, T. J. Ziemlewicz, C. L. Brace, and F. T. Lee, "Liver ablation: Best practice," *Radiol. Clin. North Am.*, vol. 53, no. 5, pp. 933–971, 2015.

[136] J. Hänsler, D. Neureiter, M. Wasserburger, R. Janka, T. Bernatik, T. Schneider, W. Müller, M. Frieser, S. Schaber, D. Becker, E. G. Hahn, and D. Strobel, "Percutaneous US-guided radiofrequency ablation with perfused needle applicators: Improved survival with the VX2 tumor model in rabbits," *Radiology*, vol. 230, no. 1, pp. 169–174, 2004.

[137] M. K. Goel, P. Khanna, and J. Kishore, "Understanding survival analysis: Kaplan-Meier estimate," *Int. J. Ayurveda Res.*, vol. 1, no. 4, pp. 274–278, 2010.

[138] I. Sucandy, S. Cheek, B. J. Golas, A. Tsung, D. A. Geller, and J. W. Marsh, "Longterm survival outcomes of patients undergoing treatment with radiofrequency ablation for hepatocellular carcinoma and metastatic colorectal cancer liver tumors," *HPB*, vol. 18, no. 9, pp. 756–763, 2016.